

**Flame Spray Pyrolysis for the Preparation of Upconverting Luminescent
Nanostructured Materials**

Francesca Mangiarini

A Thesis
in
The Department
of
Chemistry and Biochemistry

Presented in Partial Fulfillment of the Requirements
For the Degree of
Doctor of Philosophy (Chemistry) at
Concordia University
Montreal, Quebec, Canada

April 2012

© Francesca Mangiarini, 2012

**CONCORDIA UNIVERSITY
SCHOOL OF GRADUATE STUDIES**

This is to certify that the thesis prepared

By: **Francesca Mangiarini**

Entitled: **Flame Spray Pyrolysis for the Preparation of
Upconverting Luminescent Nanostructured Materials**

and submitted in partial fulfillment of the requirements for the degree of

DOCTOR OF PHILOSOPHY (Chemistry)

complies with the regulations of the University and meets the accepted standards with respect to originality and quality.

Signed by the final examining committee:

Chair
Dr. M. Frank

External Examiner
Dr. J. Garcia Solé

External to Program
Dr. W. Bukowski

Examiner
Dr. P. Bird

Examiner
Dr. L. Cuccia

Thesis Supervisor
Dr. J.A. Capobianco

Approved by _____
Dr. H. Muchall, Graduate Program Director

April 24, 2012 _____
Dr. B. Lewis, Dean, Faculty of Arts and Science

ABSTRACT

Flame Spray Pyrolysis for the Preparation of Upconverting Luminescent Nanostructured Materials

Francesca Mangiarini, Ph.D.
Concordia University, 2012

Luminescent nanostructured oxides doped with lanthanide ions have a great potential in a wide range of conventional applications, such as lighting, displays and laser devices. Materials doped with lanthanide (Ln^{3+}) ions are interesting due to their unique optical properties, since they undergo a process called upconversion, which is the conversion of a low energy source (usually near-infrared) to a higher energy emission (i.e. visible or UV) through a multiphoton process. In addition to this, with the continuous increase of demand for technology miniaturization, the use of nanosized phosphors with high emission efficiencies becomes essential to replace commercially available micron-sized counterparts. In order to achieve this, it is very important to engineer phosphors for their specific application and controlling the physical and optical properties of the materials directly during their synthesis.

In this thesis, a flame spray pyrolysis (FSP) synthesis has been developed for the synthesis of luminescent nanostructures oxides. This synthesis is a one step process that allows the preparation of nanoparticles with homogeneous size distribution and the direct control of their physical properties during the synthesis. Firstly, $\text{Gd}_2\text{O}_3: \text{Er}^{3+}$, a system whose optical behaviour is well known, was chosen as a model to compare the properties of materials prepared by combustion synthesis with the ones prepared by

FSP. The materials prepared by the latter showed higher luminescence intensity and better morphological homogeneity, due to the control achieved during the preparation. Secondly, a systematic study of the FSP method showed how the morphological and optical properties change with the variation of the synthetic parameters. In particular, it has been observed that as the temperature of the flame increases, the upconversion emission increases, along with the particle size and thermal stability. Thirdly, the luminescence intensity of the nanoparticles has been enhanced, choosing different doping combinations (Yb^{3+} , Er^{3+} and alkali metal ions) and host materials (GdVO_4). Finally, the synthesis of complex systems has been explored: core-shell ($\text{Gd}_2\text{O}_3@\text{SiO}_2$) nanoparticles have been prepared more rapidly by FSP than with conventional wet synthesis methods. The versatility of FSP makes it a very suitable technique for the preparation of various nanomaterials tailored directly during the synthesis.

ACKNOWLEDGEMENTS

I am very grateful to my thesis supervisor, Prof. John A. Capobianco. I have always been excited to do research in his lab. I will never forget your confidence since the day I walked in your office for the first time. While I was working on this project, you showed me how to be independent, self-confident and build solid science from simple results.

A great thank goes to committee members, Prof. Peter Bird and Prof. Louis Cuccia. If your comments and advice guided me along this path, your continued encouragements helped me to persist.

I would like to thank also Prof. Jose García Solé, “Pepe”. I have very good memories of those months when he visited our lab. Our discussions of my results and his resourceful book helped me greatly to put together the pieces of the puzzle. I am particularly grateful for your humanity: it has been a great gift to me in that period.

I cannot forget each of the members of the Lanthanide Research Group that I will remember with great fondness. In particular, I am grateful to Prof. Fiorenzo Vetrone, who has guided and inspired me for many of these years, and Dr. Emma Martin Rodriguez. Her feedback on this thesis helped greatly to make it what it is now. Emma, you are not only a great physicist, but you are also a wonderful friend.

I would also like to extend many thanks to Prof Adolfo Speghini, from the University of Verona, whose collaboration led to several scientific publications. You saw the early beginning of this project and I have greatly appreciated our discussions and your encouragement.

Un gros merci à mes collègues chez Photon etc., les "photoneux". Vos simplicité et vos chaleur m'ont fait voir la lumière à la fin de ce chemin. J'espère continuer de faire partie de ce groupe exceptionnel pour de nombreuses années.

I would like to thank my husband, François-Simon Labelle. Mi hai sostenuto nei momenti difficili, con pazienza e amore. Il tuo supporto e incoraggiamento sono stati l'appiglio per portare questo progetto fino alla fine. Merci pour être là pour moi. Adesso, possiamo pensare a noi.

This work would not have been possible without my parents, Ornella e Piero Mangiarini. Voi avete fatto il sacrificio più grande, ma siete sempre stati lì con me, lontano e vicino, prima, dopo, e durante. Grazie per avermi dato la possibilità di fare questa impresa, senza i vostri valori, l'entusiasmo e la tenacia che mi avete trasmesso, non ce l'avrei mai fatta.

*“What I want to talk about is the problem of
manipulating and controlling things on a small scale.”*

Richard P. Feynman

TABLE OF CONTENTS

1. INTRODUCTION	1
1.1 EVOLUTION AND APPLICATIONS OF LUMINESCENT MATERIALS	1
2. BACKGROUND	7
2.1 DISCOVERY OF RARE EARTHS AND LANTHANIDES	8
2.2 POSITION OF LANTHANIDES IN THE PERIODIC TABLE AND OPTICAL PROPERTIES.	10
2.3 HOST MATERIALS	16
2.4 SYNTHESIS	20
2.5 FLAME SPRAY PYROLYSIS	25
2.6 ENHANCEMENT OF LUMINESCENCE	29
2.6.1 <i>Dopant concentration and combinations</i>	30
2.7 CORE-SHELL SYSTEMS	32
2.8 STATEMENT OF THE PROBLEM	34
3. THEORY	37
3.1 APPROXIMATION OF THE FREE ION, HAMILTONIAN AND TERM SYMBOLS.	38
3.2 CRYSTAL FIELD EFFECT.	42
3.3 GENERAL SELECTION RULES: FROM FORBIDDEN TO FORCED TRANSITIONS.	45
3.4 JUDD-OFELT THEORY AND RADIATIVE TRANSITIONS.	47
3.5 ENERGY TRANSFER	50
3.5.1 <i>Excited state absorption (ESA)</i>	53
3.5.2 <i>Energy transfer upconversion (ETU)</i>	54
3.5.3 <i>Cross relaxation (CR)</i>	55
3.5.4 <i>Photon avalanche (PA)</i>	56
3.6 THEORY OF THE NOZZLES	58
4. TECHNIQUES	62
4.1 PROPELLANT SYNTHESIS	63
4.2 FLAME SPRAY PYROLYSIS SETUP	64
4.2.1 <i>FSP synthesis</i>	65
4.2.2 <i>Burner</i>	65
4.2.3 <i>Materials</i>	66
4.2.4 <i>Delivery of solution and gas</i>	66
4.2.5 <i>Collection of nanocrystals</i>	67
4.3 PRECURSORS SOLUTION	68
4.3.1 <i>Preparation of the core/shell nanoparticles</i>	70
4.4 THERMODYNAMICS CALCULATIONS	71
4.4.1 <i>Volumetric Enthalpy of Combustion, ΔH_{CV}</i>	71
4.4.2 <i>Equivalence ratio, Φ</i>	72
4.5 CHARACTERIZATION	74
4.5.1 <i>X-ray Powder Diffraction measurement and analysis</i>	74

4.5.2	<i>Transmission Electron Microscopy (TEM)</i>	75
4.5.3	<i>Scanning Electron Microscopy (SEM) analyses</i>	75
4.5.4	<i>Thermogravimetric analysis (TGA and DTA)</i>	75
4.5.5	<i>Luminescence measurements</i>	76
5.	RESULTS AND DISCUSSION	78
5.1	FROM COMBUSTION SYNTHESIS TO FSP	79
5.1.1	<i>Combustion synthesis: phase purity and morphology</i>	79
5.1.2	<i>Flame Spray Pyrolysis: Phase purity and morphology</i>	83
5.1.1	<i>Thermodynamics of the two synthesis</i>	86
5.1.2	<i>Luminescent properties of the nanocrystals</i>	88
5.2	DEVELOPMENT OF FLAME SPRAY PYROLYSIS	94
5.2.1	<i>Synthetic parameters</i>	95
5.2.2	<i>Shape of the flame and mechanism of formation</i>	96
5.2.3	<i>Choice of metal precursor</i>	99
5.2.4	<i>Choice of solvent/fuel</i>	100
5.2.5	<i>Effect of the precursors solution flow rate</i>	104
5.2.6	<i>Effect of the oxygen flow rate.</i>	116
5.2.7	<i>Effect of the pressure drop</i>	123
5.3	ENHANCEMENT OF THE LUMINESCENCE	127
5.3.1	<i>Combination of dopants: Er³⁺ and Yb³⁺</i>	128
5.3.2	<i>Combination of dopants: alkali metals</i>	132
5.3.3	<i>Host materials: preparation of GdVO₄</i>	139
5.4	CORE SHELL SYSTEMS	144
6.	CONCLUSIONS	147
6.1	FROM COMBUSTION SYNTHESIS TO FSP	148
6.2	DEVELOPMENT OF FLAME SPRAY PYROLYSIS	149
6.3	ENHANCEMENT OF THE LUMINESCENCE	152
6.4	CORE-SHELL SYSTEMS	153
7.	FUTURE WORK	154
7.1	ALKALI METALS	155
7.2	GADOLINIUM VANADATE NANOCRYSTALS	156
7.3	CORE-SHELL SYSTEMS	157
8.	BIBLIOGRAPHY	158

LIST OF FIGURES

Figure 1.1: One of the first CRT televisions in the 1950s [1].	1
Figure 1.2: the smallest display available (Kopin Corporation) [5].	2
Figure 1.3: Security features of a euro banknote [7].	3
Figure 1.4: Solar panel on top a roof [9].	4
Figure 2.1: Periodic table and lanthanides. All the elements considered Rare Earths are highlighted in orange.	10
Figure 2.2: Dieke energy level diagram of Ln^{3+} ions in LnCl_3 [24].	12
Figure 2.3: generic UC mechanism	14
Figure 2.4: Absorption and fluorescence spectra of $\text{CaF}_2:\text{Er}^{3+}$ [40]	15
Figure 2.5: Upconversion mechanism in Er^{3+} . The subsequent absorption of two photons is followed by green and red emission.	15
Figure 2.6: Symmetry sites of Gd_2O_3 .	18
Figure 2.7: Flame Spray Synthesis [71]	23
Figure 2.8: Experimental set-up of FSP using an air-assisted nozzle and six supporting CH_4/O_2 flamelets for spray pyrolysis of fumed silica. [71]	25
Figure 2.9: schematic diagram for the dependence between synthesis settings and flame properties.	26
Figure 2.10: CL spectra of (a) $\text{Y}_{1.95}\text{xLi}_x\text{O}_3:\text{Eu}_{0.05}$ a doping agent of Li ions [96].	30
Figure 2.11: coated particles ($\text{SiO}_2\text{-CeO}_2$) prepared by FSP [107]	33
Figure 3.1: Effect of the various perturbations on the ion for the $4f^{11}$ configuration (Er^{3+}).	43
Figure 3.2: Resonant and phonon assisted energy transfers	50
Figure 3.3: Excited state absorption mechanism	53
Figure 3.4: Energy Transfer Upconversion	54
Figure 3.5: Cross-Relaxation mechanism	55
Figure 3.6: Photon Avalanche mechanism	56
Figure 3.7: converging and diverging ducts.	58
Figure 3.8: Converging-diverging duct (a) and diverging-converging duct (b).	61
Figure 3.9: converging-diverging duct and detail of the flow.	61
Figure 4.1: Schematic of the FSP setup	64
Figure 4.2: Details of the FSP synthesis setup. A: flame and flamelets, B: flowmeters and controller, C: flame and pressure gauge, D: syringe and syringe pump, E: glass fiber filter, F: collection of particles, G: flame and burner detail (note the concentric cylinders at the bottom of the burner).	67
Figure 4.3: Experimental setup for decay times measurements.	77
Figure 4.4: Experimental setup for UC emission measurements.	77
Figure 5.1: XRPD of $\text{Gd}_2\text{O}_3:\text{Er}^{3+}$ prepared by propellant synthesis	80
Figure 5.2: TEM (top) and SEM (bottom) images of $\text{Gd}_2\text{O}_3:\text{Er}^{3+}$ prepared by propellant synthesis	81
Figure 5.3: SEM images of $\text{Gd}_2\text{O}_3:\text{Er}^{3+}$ prepared by FSP	83
Figure 5.4: TEM images of $\text{Gd}_2\text{O}_3:\text{Er}^{3+}$ prepared by FSP	84
Figure 5.5: XRPD pattern of $\text{Gd}_2\text{O}_3:\text{Er}^{3+}$ prepared by FSP	85
Figure 5.6: Room temperature luminescence of $\text{Gd}_2\text{O}_3:\text{Er}^{3+}$ prepared by propellant synthesis and FSP	88
Figure 5.7: Upconversion mechanisms responsible for the green (7-8) and red (9) emission in Er^{3+} -doped Gd_2O_3 nanocrystals. – (1-2-3) energy transfer upconversion (ETU), (4-5) excited state absorption (ESA), and (6) cross relaxation [$^4\text{F}_{7/2}, ^4\text{I}_{11/2}$] \rightarrow [$^4\text{F}_{9/2}, ^4\text{F}_{9/2}$] (CR).	89

Figure 5.8: : Room temperature upconversion spectra ($\lambda_{exc} = 980 \text{ nm}$) of $\text{Gd}_2\text{O}_3:\text{Er}^{3+}$ (a) 0.1 mol%, (b) 1 mol% and (c) 10 mol% prepared by propellant synthesis (top) or FSP (bottom) – (i) ${}^2\text{H}_{11/2} \rightarrow {}^4\text{I}_{15/2}$, (ii) ${}^4\text{S}_{3/2} \rightarrow {}^4\text{I}_{15/2}$ and (iii) ${}^4\text{F}_{9/2} \rightarrow {}^4\text{I}_{15/2}$.ii) ${}^4\text{F}_{9/2} \rightarrow {}^4\text{I}_{15/2}$.	91
Figure 5.9: Plot of the ratio of the integrated intensity listed in Table 5.2 -▲ propellant synthesis, ○ FSP	92
Figure 5.10: Setup of Flame Spray Pyrolysis	94
Figure 5.11: Variable synthesis settings and their effect on the flame.	95
Figure 5.12: Effect of the fuel flow rate on the flame.	96
Figure 5.13: Effect of the oxygen flow rate on the flame.	96
Figure 5.14: Effect of the opening of the nozzle on the flame.	97
Figure 5.15: Formation of particles along the length of the flame	98
Figure 5.16: XRPD patterns of the samples prepared with different molar compositions of xylene (xyl) in 2EHA. Xyl# indicates the molar fraction of xylene in a xylene/2EHA solution.	103
Figure 5.17: UC spectra of $\text{Gd}_2\text{O}_3:1\%\text{Er}^{3+}$ samples at different precursor solution flow rates. $\lambda_{exc} = 980 \text{ nm}$.	105
Figure 5.18: UC emission spectra, normalized to ${}^4\text{S}_{3/2}$, at different precursor solution flow rates. $\lambda_{exc} = 980 \text{ nm}$	106
Figure 5.19: Intensity ratios between the red emission (${}^4\text{F}_{9/2}$, centered at 673 nm) and the green emissions (${}^2\text{H}_{11/2}$, ${}^4\text{S}_{3/2}$, centered at 548 nm)	106
Figure 5.20: TGA measurements of $\text{Gd}_2\text{O}_3:1\%\text{Er}^{3+}$ samples at different precursor solution flow rates.	108
Figure 5.21: DTA and TGA of $\text{Gd}_2\text{O}_3:1\%\text{Er}^{3+}$ sample prepared at 2.66 mL/min.	109
Figure 5.22: XRPD patterns of the samples prepared at different precursor flow rates.	112
Figure 5.23: Cubic and Monoclinic phase of Gd_2O_3 .	113
Figure 5.24: Plot showing the trend of the liquid flow rate and the volumetric combustion enthalpy respect to the % of monoclinic phase (▼) in the products and the particle size (△).	114
Figure 5.25: TEM images of $\text{Gd}_2\text{O}_3:1\%\text{Er}^{3+}$ samples prepared at different precursor solution flow rates	115
Figure 5.26: UC spectra of $\text{Gd}_2\text{O}_3:1\%\text{Er}^{3+}$ samples at different oxygen flow rates. $\lambda_{exc} = 980 \text{ nm}$.	117
Figure 5.27: UC emission spectra, normalized to ${}^4\text{S}_{3/2}$, at different oxygen flow rates. $\lambda_{exc} = 980 \text{ nm}$	118
Figure 5.28: Intensity ratios between the red emission (${}^4\text{F}_{9/2}$, centered at 673 nm) and the green emissions (${}^2\text{H}_{11/2}$, ${}^4\text{S}_{3/2}$, centered at 548 nm)	118
Figure 5.29: TGA measurements of $\text{Gd}_2\text{O}_3:1\%\text{Er}^{3+}$ samples at different oxygen flow rates.	119
Figure 5.30: XRPD patterns of the samples prepared at different oxygen flow rates.	120
Figure 5.31: Plot showing the trend of the oxygen flow rate and the volumetric combustion enthalpy respect to the % of monoclinic phase (▼) in the products and the particle size (△).	122
Figure 5.32: TEM images of $\text{Gd}_2\text{O}_3:1\%\text{Er}^{3+}$ samples prepared at different oxygen flow rates	122
Figure 5.33: UC emission spectra at different pressure drops. $\lambda_{exc} = 980 \text{ nm}$	124
Figure 5.34: UC spectra of $\text{Gd}_2\text{O}_3:1\%\text{Er}^{3+}$ (–) $\text{Gd}_2\text{O}_3:1\%\text{Er}^{3+}$, 1% Yb^{3+} (–) samples. $\lambda_{exc} = 980 \text{ nm}$.	129
Figure 5.35: Upconversion mechanisms responsible for the green (7-8) and red (9) emission in Er^{3+} , Yb^{3+} -doped Gd_2O_3 nanocrystals. – (1-2-3) energy transfer upconversion (ETU), (4-5) excited state absorption (ESA), and (6) cross relaxation [${}^4\text{F}_{7/2}$, ${}^4\text{I}_{11/2}$] \rightarrow [${}^4\text{F}_{9/2}$, ${}^4\text{F}_{9/2}$] (CR), (10-11-3) ETU from Yb^{3+} , (12-13) ETU and lattice dissipation.	130
Figure 5.36: UC spectra of $\text{Gd}_2\text{O}_3:1\%\text{Er}^{3+}$, 1% Yb^{3+} , 1% M^+ samples, where M^+ is an alkali metal. $\lambda_{exc} = 980 \text{ nm}$.	132
Figure 5.37: XRPD analysis of $\text{Gd}_2\text{O}_3:1\%\text{Er}^{3+}$, 1% Yb^{3+} , 1% M^+ samples, where M^+ is an alkali metal.	135
Figure 5.38: Decay time curve of $\text{Gd}_2\text{O}_3:1\%\text{Er}^{3+}$, 1% Yb^{3+} sample at the green emitting state (${}^4\text{S}_{3/2}$).	136
Figure 5.39: XRPD patterns of $\text{GdVO}_4:1\%\text{Er}^{3+}$.	140

Figure 5.40: structure of $GdVO_4$.	140
Figure 5.41: TEM images of $GdVO_4: 1\%Er^{3+}$	141
Figure 5.42: UC emission of $GdVO_4:1Er^{3+}$. $\lambda_{exc} = 980$ nm. The inset shows the emission of the sample, normalized at the $^4S_{3/2}$ peak, at different excitation power.	142
Figure 5.43: Power study of the $GdVO_4:1Er^{3+}$, upon excitation at 980 nm.	142
Figure 5.44: core-shell $Gd_2O_3:1Er^{3+}, 1Yb^{3+}, 1Li^+ @SiO_2$ prepared by FSP	145
Figure 5.45: core-shell $Gd_2O_3:1Er^{3+}, 1Yb^{3+}, 1Li^+ @SiO_2$ prepared by Stöber method.	145

LIST OF TABLES

Table 2.1: History of the discovery of Rare Earths elements [13]	8
Table 2.2: Lattice parameters and cell volume of monoclinic phase $Gd_2O_3:Er^{3+}$ [55]	17
Table 2.3: Size of the main Ln^{3+} ions used in this thesis.	17
Table 2.4: Typical synthetic routes for upconverting nanocrystals [63]	21
Table 4.1: Samples prepared by Combustion Synthesis.	63
Table 4.2: Metal Precursors	68
Table 4.3: Lanthanide ion precursors	68
Table 4.4: Alkali metal ion precursor	68
Table 4.5: Solvent (fuel)	68
Table 4.6: Samples prepared by FSP	69
Table 4.7: Core-shell samples prepared by FSP	70
Table 5.1: The combustion enthalpies of the propellant and FSP syntheses.	86
Table 5.2: The ratio of the integrated intensity of the ${}^4F_{9/2} \rightarrow {}^4I_{15/2} / ({}^2H_{11/2}, {}^4S_{3/2}) \rightarrow {}^4I_{15/2}$ emission bands after excitation using a wavelength of 980 nm	92
Table 5.3: Solvents used for the preparation of the precursor solutions and their characteristics.	100
Table 5.4: solutions of xylene in 2EHA.	103
Table 5.5: Series of samples prepared to study the effect of the solution flow rate on the final properties of the nanoparticles. Oxygen flow rate is kept at 2L/min and the pressure drop at 2 atm.	104
Table 5.6: red/green ratio of the samples prepared at different liquid flow rates	106
Table 5.7: Summary of the samples prepared at various precursor flow rates, showing the volumetric combustion enthalpy, the % of monoclinic phase and the size of the particles.	112
Table 5.8: Series of samples prepared to study the effect of the oxygen flow rate on the final properties of the nanocrystals. Precursor solution flow rate is kept at 2 mL/min and the pressure drop at 2 atm.	116
Table 5.9: red/green ratio of the samples prepared at different oxygen flow rates	118
Table 5.10: Summary of the samples prepared at various oxygen flow rates, showing the volumetric combustion enthalpy, the % of monoclinic phase and the size of the particles.	120
Table 5.11: Series of samples prepared to study the effect of the pressure drop on the final properties of the nanocrystals. Precursor solution flow rate is kept at 2 mL/min and the oxygen flow rate at 2l/min.	123
Table 5.12: UC emission spectra, normalized to ${}^4S_{3/2}$, at different pressure drops. $\lambda_{exc} = 980$ nm.	125
Table 5.13: size of the nanocrystals prepared at different pressure drops.	126
Table 5.14: Red/green ratios of alkali metal-doped samples.	133
Table 5.16: Cell parameters calculated by Rietveld refinement of the samples doped with alkali metals.	135
Table 5.17: Decay times (τ) of the alkali metal undoped and alkali metal doped $Gd_2O_3:1Er^{3+}, 10Yb^{3+}$	136
Table 6.1: Summary of the effects of the synthesis parameters on the final products. ↗ indicates an increase and ↘ indicates a decrease.	149

1. Introduction

1.1 Evolution and applications of luminescent materials

Since the antiquity, humanity has been intrigued by the emission of light, also known as luminescence. At the time of ancient Rome, Titus Livius reported about women decorating their hair with “glowing torches” [2] during the bacchanalia, the



Figure 1.1: One of the first CRT televisions in the 1950s [1].

rituals for the worship of the god Bacchus. However, the first rational approaches on luminescence are dated only at the beginning of the 16th century, when alchemists were interested in searching the Philosopher’s Stone, known to transform metals into gold. It is during this time that an Italian alchemist, Vincenzo Casciarolo, described how to produce the “Bolognian Stone”. According to his description, this stone had a “magic” property: it “accumulated” light when exposed to the sun, and emitted it in the dark [3]. Today, it is known that the magic property was simply phosphorescence and that the Roman glowing accessories and the stone in question were barium sulphate [4].

In the early 17th century, Brand introduced the term “phosphorous” to designate substances glowing in the dark and “phosphorescence” to describe the occurrence of this phenomenon. Even J. W. von Goethe, known for his marked interest in science and particularly in chemistry, was captivated by the study of luminescence.

The scientific investigation of phosphors began only in the 19th century, most notably with the studies of luminescence undertaken by Stokes, Becquerel and Röntgen.

In particular, Stokes introduced the law according to which the emission of light occurs at wavelengths longer than the excitation light. However, the introduction of quantum mechanics in the 20th century was the key point to understand the phenomenon of luminescence and make it accessible for industrially interesting applications, such as lasers or lighting. Starting from the 1940s, after the introduction of cathode ray tubes (CRT), many researchers focused their attention on the study of phosphors. The evolution of these materials has played a key role in the development of televisions, personal computer monitors and fluorescent lighting.



Figure 1.2: the smallest display available (Kopin Corporation) [5].

The introduction of nanotechnology, with Feynman in 1959, opened a new era for science and technology. From the first CRT used in a display in 1907 much progress was made and, today, there is growing demand for small displays, in order to miniaturize the available devices and improve the screen resolution.

The smallest display commercially available has the size of a thumbnail and a resolution higher than that of a cell phone display. In fact, nanophosphors can be used to make smaller pixels and, as a consequence, increase the resolution of the display.

Nowadays, luminescent materials have been considered to solve problems in fields non conventional for phosphor science, e.g. anti-counterfeiting or solar cells.

Counterfeiting has a negative impact on the economy of many countries and in the last 20 years, the amount of counterfeited goods was multiplied by one hundred [6].

When the Euro, the new European currency, was introduced in 2002, the bank notes

have been engineered to include sophisticated anti-counterfeiting measures.

For this purpose, Europium compounds have been added to bank notes to include a luminescent signature that would validate

the authenticity of the said notes. In light of

this, it is clear how the choice of phosphors

with complex luminescent signatures would improve the anti-counterfeiting measures.

For example, phosphors that emit visible light when excited by infrared sources (IR) are part of a non-conventional group of luminescent materials.

Unfortunately, the action of counterfeiters is not limited to paper currency and the growth of this activity has affected many industries. If in the 1980s falsification was involving mainly manufacturers of luxury products (e.g. branded fashion items), today counterfeiting is extending to food, wine, medicines and automotive parts, creating health and safety concerns.



Figure 1.3: Security features of a euro banknote [7].

The U.S. Chamber of Commerce recently estimated the value of counterfeited goods traffic at 650 billions of dollars per year. Within these, it has been estimated that in 2010 the sale of counterfeited drugs would reach 75 billions of dollars [8]. For this purpose, luminescent materials at the nanoscale would not only provide a unique signature, but also open the possibility of marking drugs at the pill level. This technology is already commercially used by some manufacturers as, for example, Nanoink.

One of the main challenges of our times is the production and saving of energy. In this regard, the invention of solar cells represents a promising development, but their efficiency is still insufficient to provide an economical substitute to conventional energy



Figure 1.4: Solar panel on top a roof [9].

sources. Solar panels presently use only a limited range of wavelengths of the sunlight. Therefore, the development of solar cells that uses all the light coming from the solar radiation would improve their efficiency. In order to achieve this, it has been suggested to deposit on the back

of the solar panel a layer of phosphors that can absorb the unused wavelengths (e.g. IR) and convert them in visible light, emitting them back to the solar panel, which will transform them in usable energy. Currently, such empowered solar cells are 1% more efficient than regular solar cells [10].

Lanthanide-doped materials represent a class of phosphors able to convert IR sources to visible light. Their properties are so peculiar that, after their discovery, it was difficult to place them in the periodic table. In fact, when Mendeleev died, in 1907, the position of lanthanides was not yet defined and, at that time, the periodic table had already been introduced for forty years [11].

Lanthanides found their currently known position only after 1925, when Bohr presented the aufbau principle and Moseley discovered the concept of atomic number. Since they show similar properties (reactivity and ionic radius), lanthanides have been placed in a separate section of the periodic table, excluding them from the main group of elements. Otherwise, the periodic law would not have been applied [12].

The above-mentioned phenomenon of absorbing light at low energy (e.g. near infra red NIR) followed by emission at higher energy (e.g. visible or UV) occurs through a multiphoton process and is called upconversion. Phosphors manifesting this property are appealing because not only they can be excited by inexpensive diodes, but also they can be used in biological applications, due to the low energy of the excitation source. In particular, if in the past luminescent compounds have been used in medicine only for imaging, there is now a need for more complex systems, capable of multi-functioning properties, from the simple bifunctional magnetic and luminescent compounds to real intelligent systems.

In this thesis, oxide nanostructured materials doped with lanthanide ions have been chosen as phosphors, since they are known to be good luminescent materials and show high resistance to elevated temperatures. In order to overcome the demand of an increasing market, a synthesis, flame spray pyrolysis, was developed to allow the production of high quantities of material in a short time.

The prepared nanomaterials have been designed according to the necessity of sophisticated technologies in the display, security, energy and biological fields.

2. *Background*

2.1 Discovery of Rare Earths and Lanthanides

They are called “rare earths”, but they are not so rare. In the past, the term “rare earth” (RE) was used to indicate the sesquioxides, RE_2O_3 , which were considered uncommon, because the RE elements were isolated only from rare minerals. However, the term “rare” is not opportune, because these metals are not as scarce on earth as their name would suggest [13,14]. In fact, the percentage of rare earths contained in the Earth’s crust is higher than the amount of precious metals, such as gold and silver [15].

Element	Year	Discoverer	Notes
Scandium	1879	NILSON	from ytterbium earths (DE MARIGNAC, 1878)
Yttrium	1843	MOSANDER	from yttrium earths (GADOLIN, 1794)
Lanthanum	1839	MOSANDER	from cerium earths (KLAPROTH, BERZELIUS, HISINGER, 1803)
Cerium	1841		
Praseodymium	1885	AUER V. WELSBACH	from didymium (MOSANDER, 1839–1841)
Neodymium			
Samarium	1901	DEMARCAV	from the samarium fraction (LECOQ DE BOISBAUDRAN, 1879)
Europium			of didymium (MOSANDER, 1839–1841)
Gadolinium	1886	LECOQ DE BOISBAUDRAN	from didymium (MOSANDER, 1839–1841)
	1880	DE MARIGNAC	independently of each other
Terbium	1878	DE MARIGNAC DELAFONTAINE	from terbium earth, (DELAFONTAINE, 1878), originally named terbium earth (MOSANDER, 1843)
Dysprosium	1886	LECOQ DE BOISBAUDRAN	from the holmium fraction (CLEVE, 1879) of erbium earth (DE MARIGNAC, 1878)
Holmium	1879	CLEVE	
Erbium	1879	CLEVE	from erbium earth (DE MARIGNAC, 1878)
Thulium	1879	CLEVE	from the holmium fraction (CLEVE, 1879) of erbium earth (DE MARIGNAC, 1878)
Ytterbium	1878	DE MARIGNAC	from ytterbium earth (DE MARIGNAC, 1878)
Lutetium	1907	URBAIN, AUER V. WELSBACH JAMES	from ytterbium earth, independently of each other (DE MARIGNAC, 1878)

Table 2.1: History of the discovery of Rare Earths elements [13]

In nature, RE elements are combined with other rare earths and their physical and chemical properties are very similar. Considering the limited analytical methods available in the 18th century and the lack of a clear understanding of the atomic structure theory, the similarities between REs made them very difficult to separate. As a consequence, they have been discovered over a long period of time, starting from 1787, when Lieutenant Carl Axel Arrehnius, an officer of the Swedish artillery, found a new mineral. After examination, he called it ytterbite, in honour of the small town of Ytterby, close to the area where he was exploring. Only in 1794, Johan Gadolin separated the earth, as oxides, in general, were used to be called at that time, and he named it yttria. With the evolution of analytic instrumentation, it was then shown that “yttria” was not a single oxide, but rather a mixture of six other rare earths, which was named gadolinite [13,14]. The discovery of RE elements continued for other hundred fifty years, when the discovery of promethium, a radioactive product of the fission of uranium, completed the series of lanthanides [13,14,16].

According to the IUPAC nomenclature recommendations published in 2005, the term “rare earths” includes the lanthanoids, with scandium and yttrium, where for lanthanoids are indicated the elements in the periodic table between Lanthanum and Lutetium: La, Ce, Pr, Nd, Pm, Sm, Eu, Gd, Tb, Dy, Ho, Er, Tm, Yb, Lu [17]. The term “lanthanoids” is considered more appropriate than “lanthanides”, which would be more proper for negative ions [17]. However, the term “lanthanides” is more commonly used in the scientific literature and will be adopted in this work.

2.2 Position of Lanthanides in the periodic table and optical properties.

The discovery of lanthanides confused the scientists of the 18th century. These new elements were different from all the others that were known at that time: each of the lanthanides formed compounds with similar properties [18,19], in the same way as it occurs between elements that belong to a certain group of the periodic table (Figure 2.1).

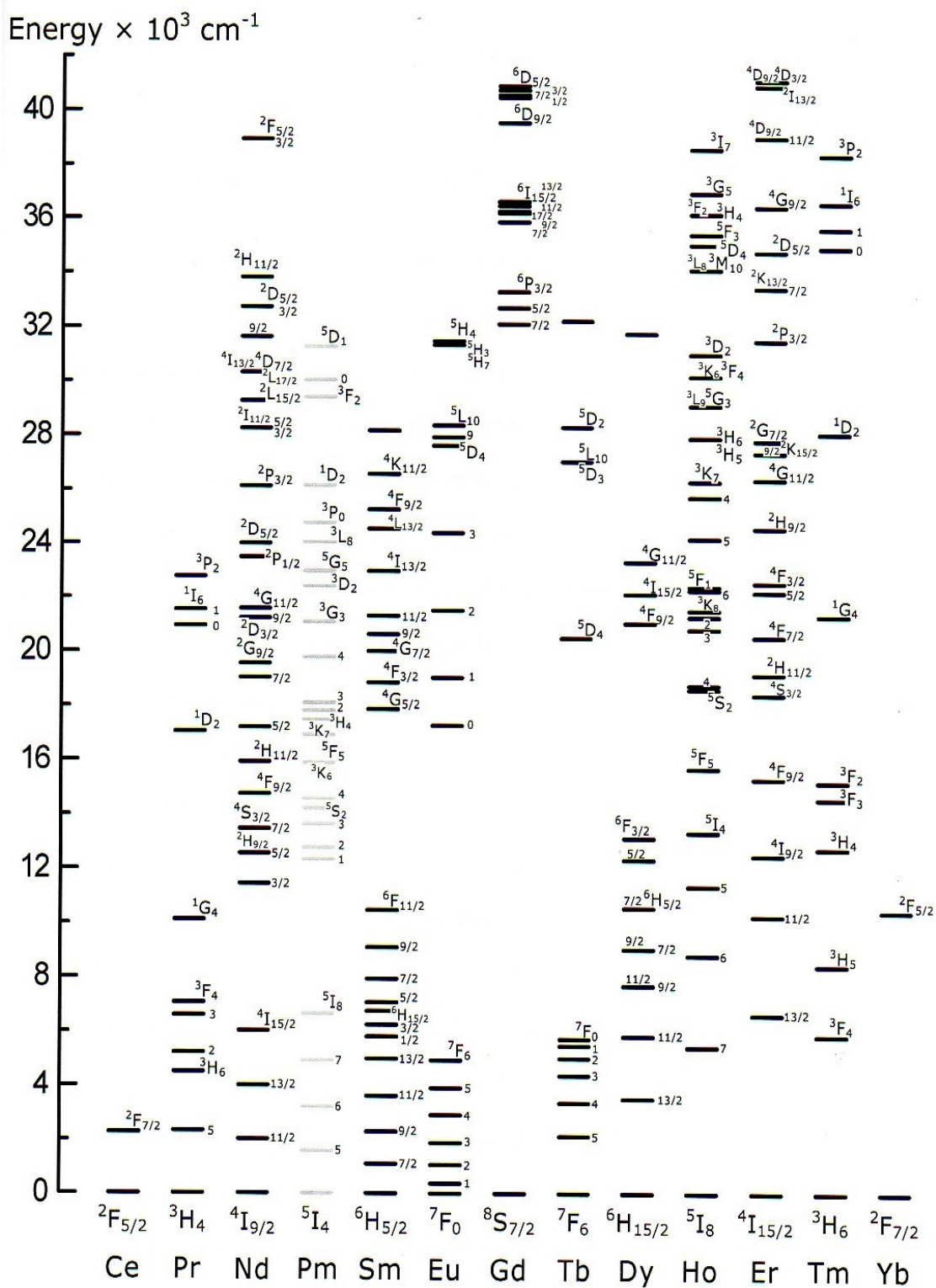
However, the lanthanides complicated the organized pattern of Mendeleev's periodic table, because it was not clear where to insert them, until the atomic structure was understood, in the 20th century [11,12].

1 H																	2 He														
3 Li	4 Be											5 B	6 C	7 N	8 O	9 F	10 Ne														
11 Na	12 Mg											13 Al	14 Si	15 P	16 S	17 Cl	18 Ar														
19 K	20 Ca	21 Sc	22 Ti	23 V	24 Cr	25 Mn	26 Fe	27 Co	28 Ni	29 Cu	30 Zn	31 Ga	32 Ge	33 As	34 Se	35 Br	36 Kr														
37 Rb	38 Sr	39 Y	40 Zr	41 Nb	42 Mo	43 Tc	44 Ru	45 Rh	46 Pd	47 Ag	48 Cd	49 In	50 Sn	51 Sb	52 Te	53 I	54 Xe														
55 Cs	56 Ba	57 La	72 Hf	73 Ta	74 W	75 Re	76 Os	77 Ir	78 Pt	79 Au	80 Hg	81 Tl	82 Pb	83 Bi	84 Po	85 At	86 Rn														
87 Fr	88 Ra	89 Ac	104 Unq	105 Unp	106 Unh	107 Uns	108 Uno	109 Une	110 Uun																						
																		58 Ce	59 Pr	60 Nd	61 Pm	62 Sm	63 Eu	64 Gd	65 Tb	66 Dy	67 Ho	68 Er	69 Tm	70 Yb	71 Lu
																		90 Th	91 Pa	92 U	93 Np	94 Pu	95 Am	96 Cm	97 Bk	98 Cf	99 Es	100 Fm	101 Md	102 No	103 Lr

Figure 2.1: Periodic table and lanthanides. All the elements considered Rare Earths are highlighted in orange.

The best placement of lanthanides in the periodic table has resulted in leaving them in a separate section, composed by the 14 elements in which the f orbitals are filled. These elements have similar properties and generate compounds in the form of trivalent ions, Ln^{3+} , with an outer configuration $5s^2 5p^6 4f^n$, where n varies from 1 (for Ce^{3+}) to 14 (for Lu^{3+}). The $4f$ orbitals are not involved in the formation of the bonds, because they are shielded by the $5s^2 5p^6$ orbitals. As a consequence, the spectroscopic properties of Ln^{3+} ions are only slightly perturbed by the environment [19]. In fact, the optical transitions of lanthanides, occurring between the $4f^n$ electrons, are essentially independent from the crystal field [20]. Moreover, the emission and absorption spectra of Ln^{3+} ions have characteristic sharp peaks and the transition lines are located in typical positions in the spectrum [21,22]. This is due to the fact that, when the lanthanides are incorporated in a host, they are shielded by the $5s^2 5p^6$ electrons and the energy states of the $4f$ valence electrons are only slightly perturbed by the crystal field. As a consequence, the crystal field interactions contribute to the shift and splitting energies much less than the spin-orbit coupling [21]. Therefore, the Ln^{3+} spectra are similar to those of the free ions, and the main features are similar from one crystal to the other.

In light of this, Dieke studied the absorption spectral lines of lanthanide ions in LaCl_3 and created the well-known Dieke diagram (Figure 2.2), where the thickness of the energy levels represents the splitting due to the crystal field [23]. For the above-mentioned reasons, this diagram can be used as reference to predict the emission spectra from the emitted levels, not only in LaCl_3 , but also in any other crystalline matrices.

Figure 2.2: Dieke energy level diagram of Ln^{3+} ions in LnCl_3 [24].

It should be pointed that, according to quantum mechanics, the transitions between states with the same parity are forbidden in the electric dipole order [21,25]. Therefore, in a free ion, the $f-f$ transitions are parity forbidden and intense emissions should not be expected from the Ln^{3+} ions. However, the effect of the crystal field may produce a slight shift in the energy of the $^{2S+1}L_J$ states and additional level splitting. In addition to this, the crystal field effect can vary the parity of these states, allowing the $f-f$ transitions at the electric dipole order.

The great number of states that can be observed in the Dieke's diagram, not only favours the emission in a wide region of the UV and VIS spectrum, but also increases the probability of energy transfer between resonant states, when more ions are combined together [26]. As a consequence, Ln^{3+} ions can be incorporated into compounds, singularly or combined, in order to emit light at a certain desired wavelength. When the emission is in the visible spectrum, this leads to the generation of different colors, according to the combination of the Ln^{3+} ions chosen. For example, a crystal, doped only with Er^{3+} , would produce green phosphors [27], but, when Er^{3+} is combined with Yb^{3+} in certain concentrations, it would produce red phosphors [28]. With the right combination of Ln^{3+} ions, it would also be possible to prepare white emitting phosphors [29,30], which are considered important in the production of LEDs [31].

As briefly mentioned in the introduction, Ln^{3+} ions undergo a process called upconversion (UC, Figure 2.3), which consists in the emission of high energy light (visible or UV) after absorption of a low energy source (usually NIR) through a multiphoton process (typically two-photon). Generalizing the UC mechanisms, the Ln^{3+} ion absorbs one NIR photon and is excited to an intermediate state, with a lifetime long enough (typically milliseconds) to allow for a second photon to excite the ion from the intermediate state to a higher one [24].

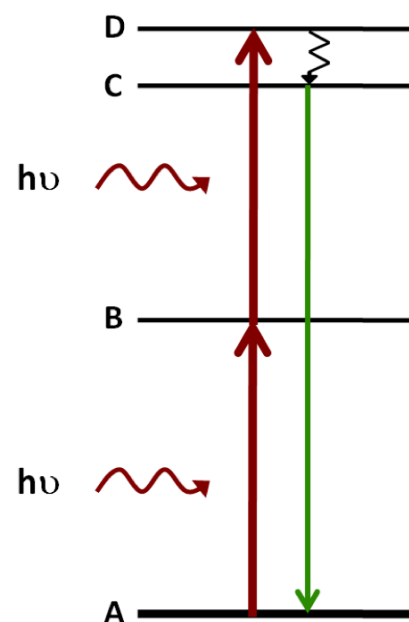


Figure 2.3: generic UC mechanism

The presence of equally spaced levels between the same Ln^{3+} ion or different ones (e.g. the $^4I_{11/2}$ state of Er^{3+} and the $^2F_{5/2}$ state Yb^{3+}), increases the probability of energy transfer (see Chapter 3) between the ions. As a consequence, the upconversion mechanism is more efficient, compared to the absence of energy transfer, and the luminescence emission is enhanced [28,32-34]. This is an important aspect to consider when upconverting phosphors are applied to new technologies. In fact, upconversion is a multiphoton process and its efficiency is lower than that of one-photon conventionally excited nanocrystals (NCs). Therefore, the enhancement of the UC intensity is one of the main challenges for the applications of Ln^{3+} doped phosphors in new technologies.

The Er^{3+} ion represents an excellent candidate for upconversion based emitting phosphors. In fact, as shown in Figure 2.2, this ion presents several energy levels emitting in the visible region of the electromagnetic spectrum, to its various absorption bands in the NIR and to the long lifetime states (e.g. $^4I_{11/2}$) that can act as reservoirs for energy transfer mechanisms [35-39].

The typical absorption and emission spectra of Er^{3+} are shown in Figure 2.4.

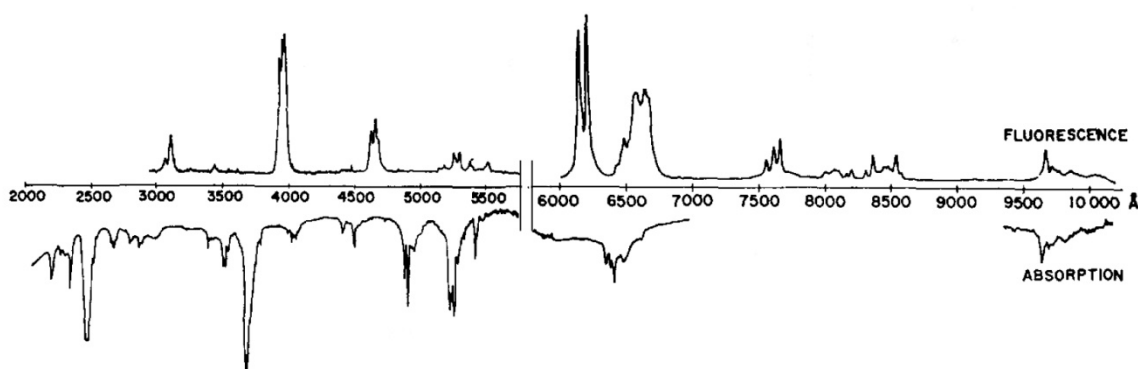


Figure 2.4: Absorption and fluorescence spectra of $\text{CaF}_2:\text{Er}^{3+}$ [40]

In this thesis, the visible green (about 540 nm) and red (about 650 nm) emissions of Er^{3+} , after 980 nm wavelength excitation, are studied. The upconversion process responsible for these emissions is showed in Figure 2.5. The mechanism will be extensively described in Chapter 5.1.

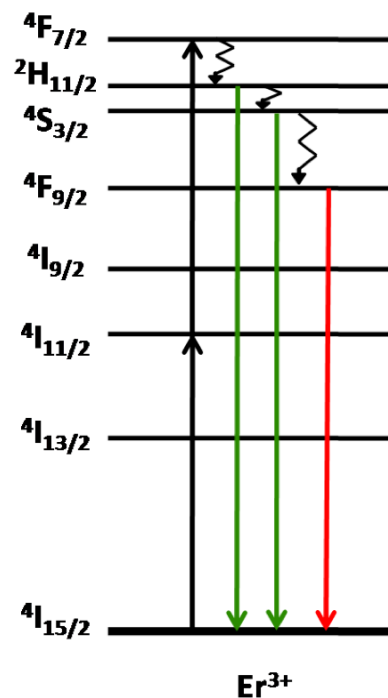


Figure 2.5: Upconversion mechanism in Er^{3+} . The sequential absorption of two photons is followed by green and red emission.

2.3 Host Materials

When designing nanomaterials doped with Ln^{3+} ions, the choice of the appropriate host material is determinant in order to have high upconversion emission and suitable optical properties. Among the insulators, the most common hosts are oxides, such as Y_2O_3 , Gd_2O_3 [22,32,41-43], fluorides, such as LaF_3 , NaYF_4 [44-46], and vanadates or phosphates [47,48]. In particular, oxides are interesting for their high thermal stability, making them attractive for the application in displays, where the heat developed during the emission process requires materials with high thermal resistance [49]. In fact, the most widely used red phosphor for lighting and plasma display panels is $\text{Y}_2\text{O}_3:\text{Eu}^{3+}$ [50]. Another advantage of using oxide phosphors (e.g. Gd_2O_3 and Y_2O_3) for displays is their photo stability [49]. In fact, some displays are prepared with NCs doped with lanthanide chelates [51], which decompose with time as a result of the released heat, which reduces, as a consequence, the life time of the material [52,53]. The integration of oxide nanoparticles could overcome the lifetime deficiency of other materials [54].

The main requirement for a host material is to have lattice sites compatible to the size of the dopant ions, which can substitute the ions of the host materials (in the case of matching lattice parameters between the host and the dopant crystal) or can enter interstitial areas.

Therefore, upconverting Ln^{3+} -doped nanomaterials can be inserted conveniently in their lanthanide compounds (e.g. Ln_2O_3 , LnF_3), since they present similar size and chemical properties.

Lattice parameters and the cell volumes of monoclinic $\text{Gd}_2\text{O}_3:\text{Er}^{3+}$ are reported in Table 2.2. As shown in Table 2.3, the size of the main Ln^{3+} ions used in this work is compatible with the lattice parameters.

Er₂O₃ (mol %)	Cell parameters				
	<i>a</i> (Å)	<i>b</i> (Å)	<i>c</i> (Å)	<i>B</i> (°)	<i>V</i> (Å ³)
1	14.135	3.584	8.786	100.130	438.195
3	14.129	3.581	8.781	100.158	437.364
6	14.116	3.577	8.772	100.156	436.034

Table 2.2: Lattice parameters and cell volume of monoclinic phase $\text{Gd}_2\text{O}_3:\text{Er}^{3+}$ [55]

Lanthanide ion	Ionic radius (pm)	Volume of ion (Å ³)
Gd^{3+}	93.8	432
Yb^{3+}	86.8	342
Er^{3+}	89.0	369

Table 2.3: Size of the main Ln^{3+} ions used in this thesis.

The symmetry of the crystal chosen as host for the Ln^{3+} ions is another important aspect to be considered for the efficiency of the luminescence emission. In fact, the symmetry, through the group theory, determines the probability of the allowed optical transitions [21]. In practice, low symmetry increases the probability of the transitions between the $^{2S+1}L_J$ states and, as a consequence, the luminescence emission is higher [20,21]. In fact, it has been reported that Ln^{3+} doped nanocrystals, existing in different phases, show the longest lifetimes and the highest emission intensity with the crystal at the lowest symmetry. These studies, for example, have been carried out on ZrO_2 [36], NaYF_4 [45], Y_2O_3 [56] and Gd_2O_3 [55].

In Figure 2.6, the symmetry of the sites in Gd_2O_3 crystals is shown. The most common phases of Gd_2O_3 are cubic and monoclinic, the latter being more difficult to synthesize. The symmetry properties of this crystal will be discussed in greater detail in Chapter 5.2.5. However, it is interesting to note the presence of a center of inversion in the cubic phase, which makes the C_{3i} site optically inactive. In fact, the selection rules forbid any transition in a center of inversion.

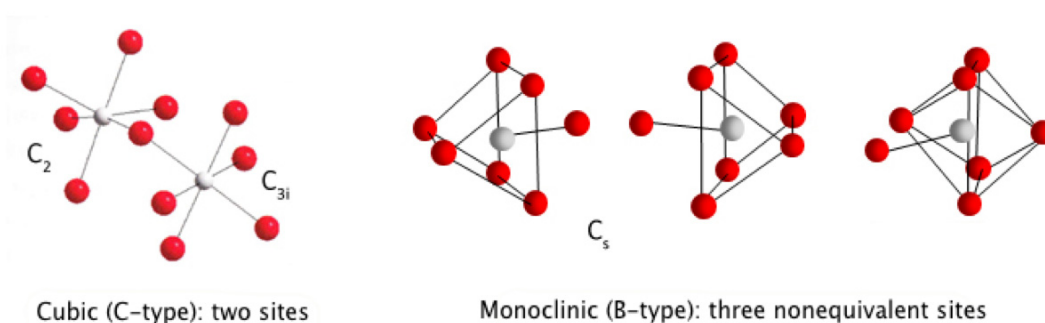


Figure 2.6: Symmetry sites of Gd_2O_3 .

Ideally, a proper host should have low phonon energy, in order to minimize non-radiative relaxations. In fact, the stretching vibrations of the lattice could fill the gap between the energy levels. Therefore, high phonon energy hosts makes the presence of non-radiative relaxations more probable, and this would reduce the efficiency of the emission [57].

For example, halides and fluorides are suitable host materials, since they present low energy phonons of about $300\text{-}350\text{ cm}^{-1}$, while oxides have a phonon energy higher than 500 cm^{-1} [58].

When Ln^{3+} ions are incorporated in insulating materials, as in the case of oxides, the position of the emission lines is not particle size dependent, as it would happen with quantum dots. However, compared to the bulk, the intensity of the luminescence and the decay times change at the nanoscale [27]. In fact, the high surface/volume ratio affects the environment of the superficial Ln^{3+} ions, with an increase in the crystalline defects.

In Ln^{3+} doped NCs, crystallinity defects as well as symmetry and position of the ions (e.g. surface or internal) affect emission and lifetimes of the material [24]. For this reason, oxides like Gd_2O_3 or Y_2O_3 are ideal host materials for lanthanide ions, as the dopants are spread out in the lattice at a sufficient distance to avoid self-quenching effects [59,60].

Ln^{3+} -doped NCs are interesting for biological applications due to their upconversion sharp emission lines and long lifetimes, which are fundamental for time-resolved methods [61]. In particular, these materials are attractive as bifunctional systems, such as labels for fluorescence and magnetic resonance imaging (MRI) applications. In fact, hosts containing Gd^{3+} (e.g. Gd_2O_3) can be used as a contrast agent for MRI. Among Gd^{3+} based compounds, Eu^{3+} and Sm^{3+} doped Gd_2O_3 (prepared by flame synthesis) have been previously reported [62], but, at the moment, there are not any reports on Er^{3+} doping.

2.4 Synthesis

Currently, several methods are available for the production of nanocrystals. The most desirable characteristic of a synthesis is the possibility to tailor the properties of the final products, such as crystal size, morphology, chemical composition, surface functionalization (if desired) and optical properties. Therefore, it is very important to choose a synthesis procedure according to the desired application of the material. For example, if a material will be used as a layer on a substrate, as in displays, it might be convenient to choose a route that allows the deposition directly during the synthesis. On the other hand, for biological applications, it is crucial to choose a synthesis that will yield to functionalized and water dispersible particles.

Upconverting oxide based nanostructured materials are the main focus of this thesis. The typical synthetic routes to prepare these materials are reported in Table 2.4.

Method	Hosts (examples)	Ref.	Advantages	Disadvantages
Coprecipitation	LuPO ₄ YbPO ₄	[64]	Fast Inexpensive equipment Easy procedure	Post synthesis thermal treatment
Thermal decomposition	Y ₂ O ₃	[65]	High quality, monodispersed nanocrystals	Expensive precursors
Hydrothermal synthesis	YVO ₄	[66]	Inexpensive reagents Excellent control of particle size and shape.	Expensive and specialized reaction autoclaves
Sol-gel	ZrO ₂ , TiO ₂ , BaTiO ₃ , Lu ₃ Ga ₅ O ₁₂ , YVO ₄	[36,37]	Inexpensive reagents	Calcination at high temperature
Combustion synthesis	Y ₂ O ₃ Gd ₂ O ₃	[67,68]	Rapid	Particle aggregation
Flame synthesis	Y ₂ O ₃	[56,62, 69]	Rapid Readily scalable Good control on particle size	Design limitations

Table 2.4: Typical synthetic routes for upconverting nanocrystals [63]

Between wet methods, coprecipitation is one of the most widely used routes. It is an easy and relatively fast technique, which allows the preparation of nanocrystals with a narrow size distribution. The possibility of adding a capping ligand directly during the synthesis makes it particularly interesting for biological applications. However, coprecipitation needs a thermal treatment after the synthesis, which adds a further step to the process. With this synthesis, various kinds of phosphates [64] have been prepared. Another widely used wet synthetic method is sol-gel, which has the advantage of using inexpensive starting materials. As for coprecipitation, sol-gel methods require calcination at high temperature in order to improve the crystallinity of the material. Therefore, it is a method used mainly for the production of oxides [36,37]. Two other wet syntheses that have been developed for the production of various upconverting nanocrystals are thermal decomposition [65] and hydrothermal synthesis [66]. Both of them allow the control of the particle size distribution during the preparation and do not require further thermal treatment. However, thermal decomposition requires expensive starting materials. On the contrary, hydrothermal synthesis requires inexpensive starting materials. However, this reaction needs to be carried under pressure in specific expensive reactors [70].

In contrast with the above-mentioned syntheses, which require prolonged reaction times, propellant synthesis allows the preparation of NCs in less than thirty minutes. This reaction consists in a controlled explosion between an oxidizer (nitrate precursors) and a fuel (glycine or urea), which are dissolved in water and heated until the formation of a gel and the combustion reaction that generates a spongy product of nanocrystalline oxides. Phosphors like Y_2O_3 and Gd_2O_3 prepared by this technique have been widely studied [55,67,68].

However, the control on the chemical and optical properties of the final material is limited only to the ratio between the fuel and the oxidizer, which affects the enthalpy of combustion, responsible for the reaction temperature, and, as a consequence, influences the particle size of the products [72].

Flame syntheses represent an alternative route for the production of metal nanostructured oxides. In these processes, a flame is used for the reaction of precursors and formation of clusters, which grow to nanometric dimensions due to coagulation and sintering [73]. The main advantages of these techniques are the preparation of nanocrystals in one step, quickly and without the production of side products.



Figure 2.7: Flame Spray Synthesis [71]

The high temperature (about 2000°C) involved in the synthesis allows the production of thermoresistant materials. Moreover, the process could be carried out continuously.

There are two main flame methods: the aerosol and the spray flame.

In the aerosol flame, the precursors (usually chlorides or isopropoxides or epoxides) are sent inside a CH_4/O_2 or H_2/O_2 flame via a carrier gas (N_2 or Ar). The disadvantage of this technique is the limit imposed by the precursor, which needs to be volatile.

Flame spray methods use precursors in organic (pyrolysis) or aqueous solutions (hydrolysis). While flame hydrolysis has a low yield, flame pyrolysis allows the formation of particles with higher crystallinity and purity [74].

In general, flame syntheses represent a convenient choice to have control on the properties of the products. In fact, the variation of different synthetic parameters affects the characteristics of the flame (e.g. temperature, length) and, as a consequence, the particle size, crystallinity and morphology of the prepared NCs. In addition to this, flame syntheses are inexpensive reactions, which occur in a single-step continuous process and, due to their design, are readily scalable.

2.5 Flame Spray Pyrolysis

Within the different kinds of flame syntheses, FSP represents a good choice for high crystalline and thermoresistant NCs. In this process, an appropriate organic precursor solution, which acts as fuel, is injected into a flame where the precursors decompose and the NCs are directly produced.

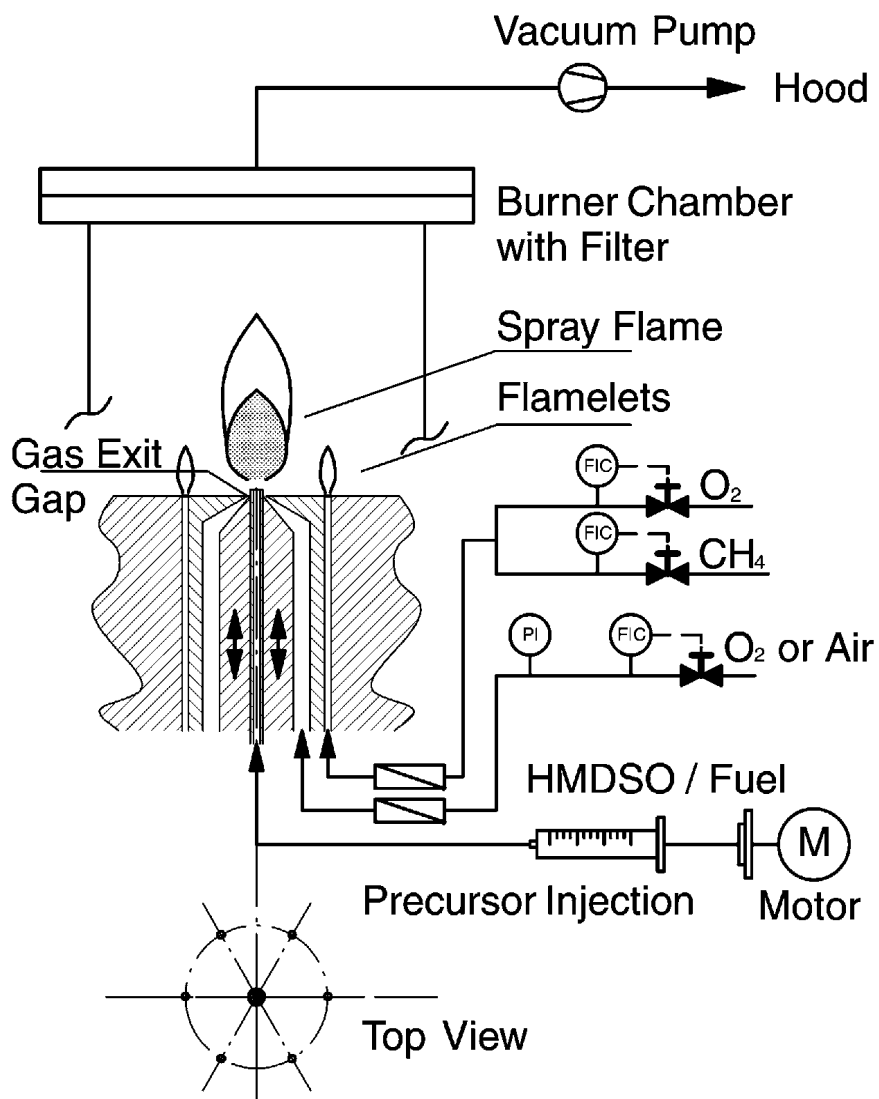


Figure 2.8: Experimental set-up of FSP using an air-assisted nozzle and six supporting CH_4/O_2 flamelets for spray pyrolysis of fumed silica. [71]

The simplicity of this technology makes it an attractive option, as it involves a single step process that does not require machinery with “moving parts”. The main advantage of using FSP consists in the properties of the resulting materials, which have small size and controlled morphology. In fact, although this is a quick process, the synthesis settings are fundamental, as they determine the product characteristics. Thus, using the FSP setup can allow for the properties of the particles to be changed directly during the synthesis [73,75-78]. The settings (oxygen rate, fuel rate and nozzle aperture) influence the flame through three conditions: the heat of combustion, the dispersion of the oxygen and the length of the

flame. The heat of combustion is proportional to the reaction temperature. The dispersion of the oxygen determines the turbulence in the flame and contributes to the mixture of the precursors and their collision after being injected.

The length of the flame affects the

time spent by the particles in the flame (residence time) and, consequently, the size and the aggregation of the products. In fact, it has been reported that conditions that favour a short residence time (e.g. high oxygen flow rate, high fuel velocity of injection) lead to small size particles (less than 50 nm).

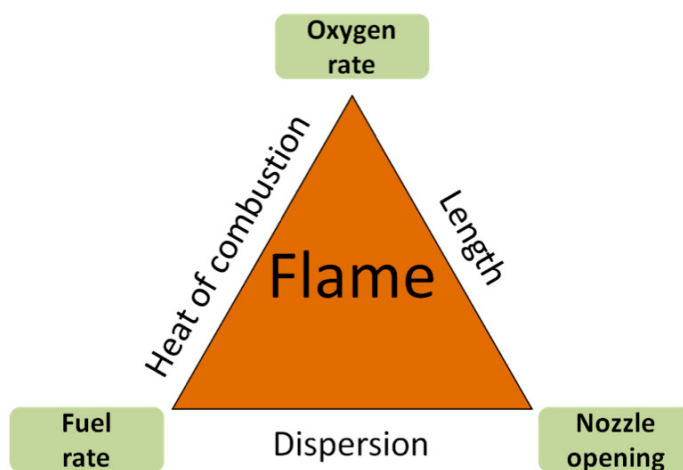


Figure 2.9: schematic diagram for the dependence between synthesis settings and flame properties.

In terms of luminescent materials, Eu^{3+} doped Y_2O_3 synthesized via FSP has been studied in great detail, because not only Eu^{3+} can be used as spectroscopic probe [19], but $\text{Y}_2\text{O}_3:\text{Eu}^{3+}$ finds commercial uses in red phosphors for lighting and display applications [50]. Y_2O_3 exists in two phases, cubic and monoclinic, and it has been reported that using an appropriate precursor will allow for the preparation of either cubic or monoclinic NCs of $\text{Y}_2\text{O}_3:\text{Eu}^{3+}$ [54,56,79,80].

In the literature, few upconverting luminescent materials prepared by FSP have been explored, such as Y_2O_3 doped with Sm, Tm, and Er [62,81]. For all the binary oxides reported, FSP has been considered as an easy and fast one-step synthetic route. One of the advantages of this method is the preparation of the precursor solution, which simply consists of the dissolution of appropriate precursors in the solvent until a transparent and stable solution is obtained. Some groups have also made more complex oxides using FSP to study their use as transparent polycrystalline laser materials, such as garnets (e.g. YAG) [82,83], and phosphates [84,85]. However, to obtain a pure garnet phase, it is necessary to add a further sintering treatment at high temperature, since the residence time in the flame is probably insufficient to produce the desired phase purity of this material [82,83]. The synthesis of these materials requires the preparation of a colloid solution for the precursors, which adds several steps to the process.

The unique morphology of the NCs prepared by this method and the good crystallinity, coupled with high luminescence intensity, make FSP an interesting option for the production of nanophosphors that are similar to commercial phosphors.

In fact, it has been reported that NCs synthesised by FSP show lower luminescence intensity, but longer decay times than commercial equivalent phosphors [56]. The prepared $\text{Y}_2\text{O}_3:\text{Eu}^{3+}$ has been compacted as tablets and ground, and then compared with commercial bulk materials. It has been showed that the nanocrystals prepared by this technique show higher luminescence intensity and decay times similar to bulk materials [56].

In light of what was discussed above, it is clear that the synthesis parameters have a fundamental impact on the properties of the final products. However, a systematic study on the impact of FSP settings on the optical properties of the resulting NCs has not been reported to date.

2.6 Enhancement of Luminescence

In order to be commercially usable, phosphors must exhibit very bright luminescence. As mentioned previously, upconversion is less efficient compared to directly excited emission [21] and the small size of the materials could affect negatively the intensity of the emission [60]. While designing nanomaterials, it is crucial to consider the elements that would improve the luminescence efficiency.

There are several approaches to achieve this:

- Concentration of dopants and/or combination of different dopants
- Host material with low symmetry and phonon energy (see 2.3)

2.6.1 Dopant concentration and combinations

As mentioned previously, lanthanide ions present several resonant energy states. When two or more dopants with resonant energy states are combined together, it is very probable that energy transfers between the ions would occur, increasing the efficiency of the luminescence. For Er^{3+} , the most common enhancer of the intensity is Yb^{3+} : it has a high absorption cross section and its unique excited state, $^2\text{F}_{5/2}$, is resonant with the $^4\text{I}_{11/2}$ state of Er^{3+} , favouring, in this way, the energy transfer between neighbouring ions [34,86,87]. For binary oxide systems containing Er^{3+} and Yb^{3+} , it has been reported that the best concentration combination is 1% Er^{3+} and 1% Yb^{3+} [33,34].

It has also been observed (Figure 2.10) that the presence of Li^+ ions in various nanocrystalline materials, such as Gd_2O_3 , Y_2O_3 , ZnO , significantly enhances the intensity of the luminescence emission [88-95]

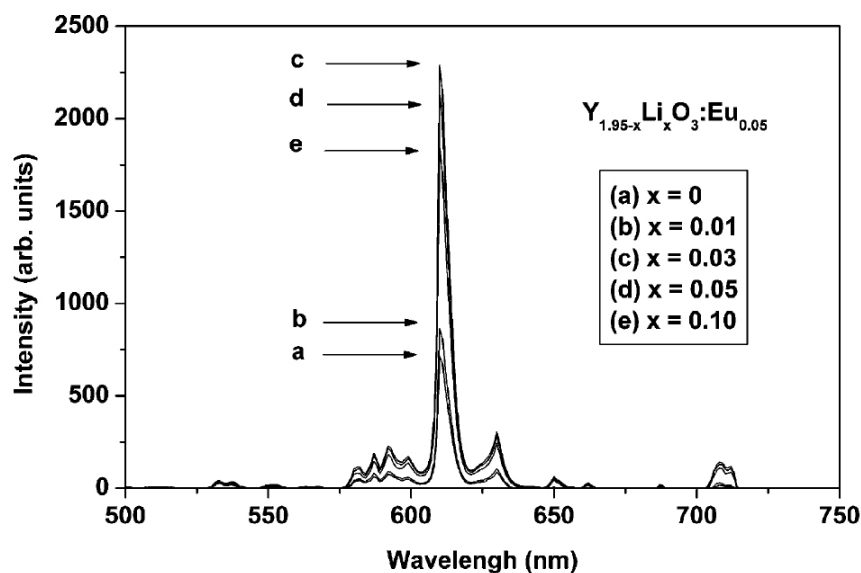


Figure 2.10: CL spectra of (a) $\text{Y}_{1.95-x}\text{Li}_x\text{O}_3:\text{Eu}_{0.05}$ a doping agent of Li ions [96].

However, a clear explanation of this effect has not yet been provided. It has been suggested that Li^+ ions might replace the Ln^{3+} ions in the optical active sites, where crystal defects are created in order to maintain the charge neutrality. Interstitial ions (e.g. Li^+) and vacancies (e.g. oxygen) would be the most probable type of crystal defects that occur in these cases [96,97]. Some studies, in fact, report the possibility of an intercalation of Li^+ ions within the crystal network [98,99].

The variation of the crystal structure in the nanocrystals affects the symmetry of the optical centers, resulting in a significant variation of the optical properties of the material [21]. Moreover, the presence of alkali metals probably influences the distance between the lanthanide ions [67]. For this purpose, it would be interesting to know how the optical properties change according to the size of the alkali ion incorporated in the matrix. At the moment, very few studies have investigated the effect of the alkali metals according to their size. For example, alkali metal doped CaS [100] and germanate tellurite glasses [101] were reported. In particular, in germanate tellurite glasses, it has been shown that at the increase of the alkali metal ion size, the intensity of the luminescence is enhanced and the maximum phonon energy (vibrational energies) decreases. Most of the studies on alkali metal ions reported in literature, use Eu^{3+} doped materials, [41,80,96,102] and little information is available concerning how Li^+ , compared to other alkali metals, affects upconversion emission.

2.7 Core-shell systems

One of the main characteristics of nanomaterials is the high surface/volume ratio, thus the surface area of the nanocrystals increases with respect to the volume at the decrease of the size. As a consequence, more Ln^{3+} ions are exposed to the hydroxylic and carboxylic groups that are present on the surface of the NCs. As mentioned previously, these groups have vibration energies resonant with several gaps between the energy states of the Ln^{3+} ions and can originate non-radiative relaxations, which would decrease the emission intensity.

To overcome this problem, the coating of nanocrystals with an inactive shell (e.g. the undoped host material) has been studied, in order to protect the surface from quenching agents. In fact, it has been observed that coated nanocrystals, over time, do not show variations in the intensity of the luminescence, while uncoated nanocrystals show a decrease in the luminescence emission [103,104].

One of the advantages of coating nanomaterials is also increasing their dispersibility in water, mostly in the case when the nanocrystals are used for biological applications. For this purpose, silica is one of the most suitable shells [105]. In fact, the Si-O groups present on the surface can be attached to organic groups, which can eventually be anchored to biomolecules.

Flame spray pyrolysis has been used to prepare silica coated compounds such as $\text{Fe}_2\text{O}_3@ \text{SiO}_2$ or $\text{TiO}_2@ \text{SiO}_2$ [106], but it has not been reported yet any study regarding the preparation by FSP of upconverting silica coated nanomaterials.

Compared to conventional wet silica coating methods, (e.g. Stöber [108]), FSP has the advantage of being an extremely rapid method. If for a conventional wet method the coating takes 2-3 days, with FSP a silica coating is achieved in less than one hour. According to the design of the synthesis, it is also possible to prepare a core-shell system in a single step [109], reducing even further the reaction times.

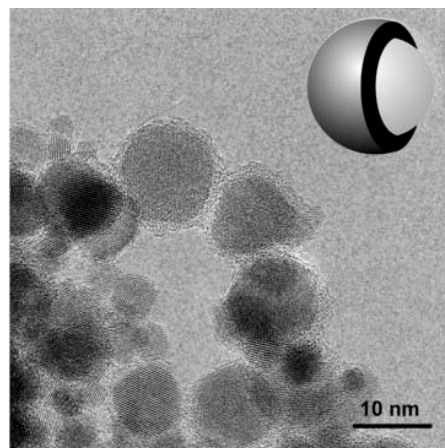


Figure 2.11: coated particles ($\text{SiO}_2\text{-CeO}_2$) prepared by FSP [107]

Coatings can also be used to produce multifunctional systems (e.g. luminescent and magnetic), which can be used for dual detection, through both their optical and magnetic properties. In literature the synthesis by FSP of Fe_2O_3 as magnetic core, with a luminescent $\text{Gd}_2\text{O}_3:\text{Eu}^{3+}$ shell has been reported [110-112]. To synthesize a core/shell material via FSP, the core synthesized nanoparticles are dissolved with the precursor solution of the desired shell. As solvent, EtOH or water are preferred for the preparation of the shell, as they tend to facilitate the coating of NCs [113,114]. However, the studies of magnetic luminescent phosphors prepared by FSP, like all the literature of luminescent materials prepared by this technique, have been focused mainly on Eu^{3+} doped NCs. At the moment, there is not presently any report on upconverting bifunctional nanomaterials.

2.8 Statement of the Problem

Conventional applications intended for materials doped with lanthanide ions are lighting, displays and laser devices. With the continuous increase of demand for technology miniaturization, the use of nanosized phosphors becomes essential. However, when the size decreases, the surface area increases as well as the amount of quenching agents on the surface and, as a consequence, the luminescence intensity diminishes. Therefore, in order to make phosphors at the nanoscale an attractive replacement for commercially available micron-sized counterparts (2.5-8 μm) the development of luminescent materials with high emission efficiencies is crucial. To achieve this, the choice of dopants and host materials leading to very bright phosphors is fundamental. Nanosized oxides represent an attractive class of materials for the above mentioned purposes, due to their relatively low phonon energies, compatibility with Ln^{3+} ions sizes and high thermal stability.

In recent years, the interest towards phosphors extended to non-conventional fields, such as security, energy saving and medicine. It becomes important to engineer the phosphors according to their destination and be able to control the physical and optical properties of the materials directly during their synthesis. The most common methods of preparation imply wet techniques, which can require reactions at high temperature for a relatively long period of time (days). In order to overcome the demand of an increasing market, a synthesis occurring in a short time period would be attractive for the production of commercial phosphors.

Flame spray pyrolysis is a one step process that allows the preparation of nanoparticles with homogeneous size distribution and the direct control of their physical properties during the synthesis. However, the understanding of how the optical properties change with the variation of the synthetic parameters is lacking.

The enhancement of the luminescence intensity of the NCs would be achieved with a suitable host, the right combination of dopants and the preparation of core-shell systems. The codoping of Yb^{3+} and Er^{3+} ions results in a higher intensity in the upconversion due to the energy transfer from the Yb^{3+} ions [33,87,115]. The addition of other ions, like Li^+ , is known to enhance the luminescence efficiency [41,97,102,116], but the reason is not well understood yet as well as the effect of the other alkali metals has not been studied yet. To avoid quenching the luminescence intensity because of surface agents, the surface of the NCs can be protected with a shell of undoped material (e.g. $\text{Gd}_2\text{O}_3:\text{Er}^{3+}$ core @ Gd_2O_3 shell) or a coating with SiO_2 .

Since the conventional preparation of core/shell systems requires several days, FSP would shorten the reaction times. It will be studied also the possibility of producing core-shell systems in one single step.

This work intends to present FSP as an attractive and versatile choice for the production of luminescent NCs. Firstly, the materials prepared by FSP have been compared with the ones prepared by another high temperature synthesis, propellant.

Then, the synthetic settings have been optimized choosing a known system as $\text{Gd}_2\text{O}_3:\text{Er}^{3+}$. In order to enhance the luminescence, different hosts have been selected (GdVO_4 , GGG) and synthesized for the first time by FSP. Finally, the preparation of core/shell systems ($\text{Gd}_2\text{O}_3@\text{SiO}_2$) has been developed. The versatility of FSP makes it a very suitable technique for the preparation of various nanomaterials tailored directly during the synthesis.

3. *Theory*

This chapter is a reference to the theory necessary to understand the main techniques used in this thesis. For the part relative to the optical spectroscopy, the texts of Di Bartolo [117], García-Solè [21] and Henderson [25] have been taken as reference.

3.1 Approximation of the free ion, Hamiltonian and term symbols.

Lanthanide ions are slightly affected by the environment of the crystal where they are incorporated, because of their electronic configuration. Their common oxidation state is Ln^{3+} , which corresponds to an electric configuration $[\text{Xe}]4f^n$ and, as a consequence, the properties of lanthanide ions depend on the 4f electrons. In particular, the shielding effect of the 5s and 5p orbitals makes these ions only imperceptibly perturbed by the crystal field. In fact, the resulting spectra show sharp lines, similar to the ones of the free ions, and the negligible shift of the spectral lines, observed when the lanthanide ions are inserted into a crystal, is caused by the perturbation of the Hamiltonian. Because of the above mentioned conditions, the Hamiltonian can be resolved using the approximation of the weak crystal field.

The Hamiltonian that defines the energy levels of the electrons in the free ion (H_{FI}) can be expressed as the sum of three terms:

$$H_{FI} = H_0 + H_{ee} + H_{SO} \quad (3.1)$$

where

- H_0 describes the interaction with the electrons in the unfilled 4f shells
- H_{ee} reflects the Coulomb interaction between the electrons
- H_{SO} represents the spin-orbit interaction and it represents the interaction between the spin momentum and the orbital.

The first term, H_0 , is described with the approximation of the central field: each electron moves, independently from the other electrons of its shell, in an electrostatic field, with spherical symmetry. The solutions of this Hamiltonian are characterized by the quantum numbers n (principal quantum number) and l (azimuthal quantum number). For the 4f orbitals, as in the case of lanthanide ions, $n=4$ and $l = 3$.

The two following terms, H_{ee} and H_{SO} , are corrections more or less negligible, but necessary, to the solution of this first Hamiltonian. When the spin-orbit interaction represents only a small perturbation of the energy level structure, H_{ee} is much higher than H_{SO} ($H_{ee} \gg H_{SO}$), in agreement with the approximation of Russell-Saunders. On the contrary, when the Coulomb interaction is negligible, H_{SO} is much higher than H_{ee} ($H_{SO} \gg H_{ee}$), as attributed to the *jj*-coupling scheme.

The lanthanide ions lie in an intermediate situation, where the terms H_{ee} and H_{SO} are similar. Therefore, they must be approached simultaneously, considering them as a perturbation of the 4f levels.

The Hamiltonian H_{ee} takes in consideration the correction of the electric field, created around the electron, because of the presence of other electrons in unfilled orbitals. As a consequence, the electric field will no longer be spherical. In this case, the energy states of the atom are described by the total orbital angular momentum quantum number, L , and the total spin angular momentum quantum number, S . In this way, the states with same electronic configuration, $4f^n$, but defined values of L and S , will still have defined energy. Generally, the resulting term symbols are labelled using the notation ^{2S+1}L , where L is designated by a letter ($S, P, D, F, G, H, I, \dots$) according to its numerical value ($0, 1, 2, 3, 4, 5, 6, \dots$). These terms show degeneracy, given by $(2L+1)(2S+1)$.

The spin-orbit Hamiltonian, H_{SO} , when treated like a perturbation of the calculated energy levels, breaks this degeneracy. Since H_{SO} produces a coupling of the vectors L and S , a new quantum number is introduced: J , called total angular momentum quantum number, which considers the interactions between all the spins and the orbital angular momenta.

As a result, the quantum levels are defined by the labels $^{2S+1}L_J$ and are energetically separated by a distance proportional to the larger of the J value, as indicated by the Landé interval rule. The degeneracy of these levels is given by $(2J+1)$ and could be broken, totally or partially, when an external field is applied.

The Dieke diagram (Figure 2.2) shows the energy positions of the levels of the different lanthanides in the trivalent status in LaCl_3 (Dieke 1968). The energy levels are labelled according to the previous explanations.

As said before, in the case of lanthanide ions, H_{ee} and H_{SO} have the same order of magnitude, in an intermediate situation, between the Russell-Sanders coupling and the *jj*-coupling. In this case, the terms are treated as a mixture of the states with same J but with different values of L and S .

3.2 Crystal field effect.

When an ion is incorporated in a solid, the interaction between the ion in question and the neighbouring ions in the material must be considered. In general, the distribution of charge, associated to these neighbouring ions, generates an electric field, commonly known as crystal field, which has an effect on the studied ion. For this reason, the Hamiltonian of the crystal field, H_{CF} , is added to the term of the free ion, in order to consider properly the perturbations on the system.

$$H = H_{FI} + H_{CF} \quad (3.2)$$

As it has been said, one of the main characteristics of the lanthanide ions is the presence of valence electrons shielded by the 5s and 5p orbitals. For this reason, in these ions, the effect generated by the crystal field is very little and modify only slightly their properties. In this way, the Dieke diagram can be used as main reference for the different ions of the rare earths and to identify their positions in the levels, independently from the matrix.

For lanthanide ions, the crystal field is weak. As a consequence, the splitting of the different energy levels is attributed to $H_{ee} > H_{SO} > H_{CF}$ (Figure 3.1). As general rule, the degree of splitting of the degeneracy depends on the group symmetry of the site occupied by the ion in the material and it will be higher as lower the degree of symmetry is.

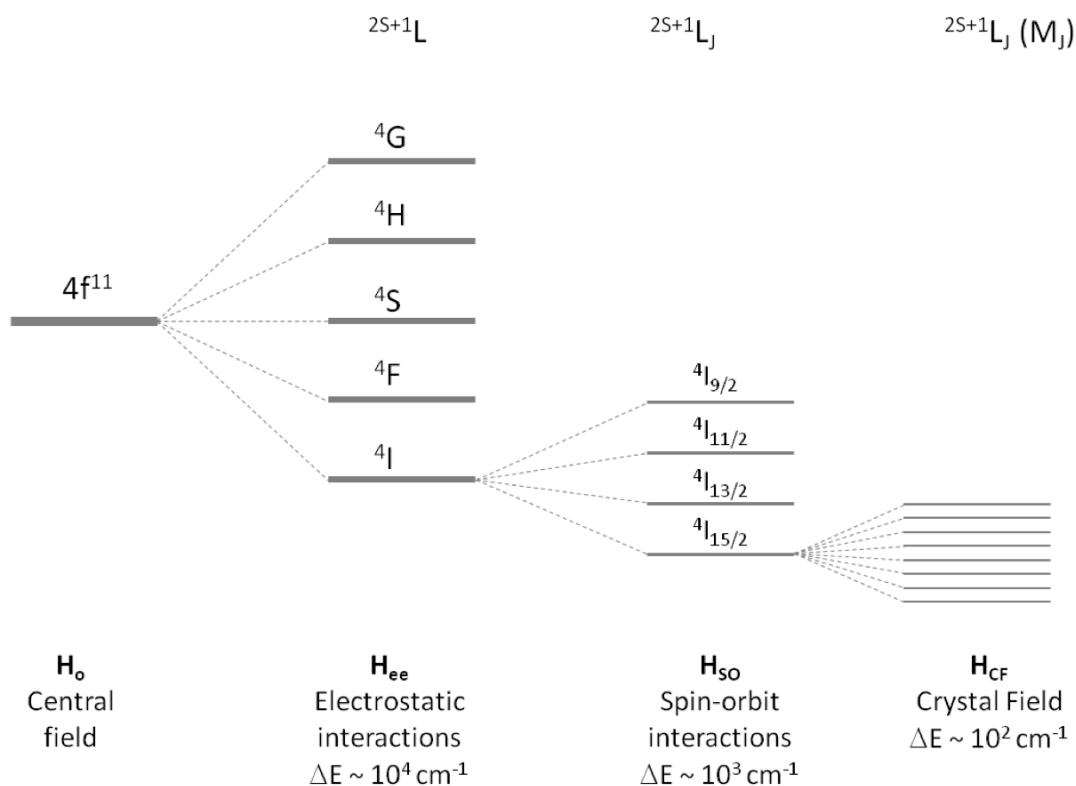


Figure 3.1: Effect of the various perturbations on the ion for the $4f^{11}$ configuration (Er^{3+}).

Experimentally, it has been observed that, for the lanthanide ions, the separation between the levels, ΔE , associated to the presence of the crystal field is generally lower than the other perturbations. For example, the splitting of the degeneracy produced by the spin-orbit term gives levels energetically separated by units of 10^3 cm^{-1} , while the Stark splitting generates levels separated by 10^2 cm^{-1} .

The crystal field Hamiltonian is considered as a perturbation of the levels $^{2S+1}L_J$, obtained from the free ion and it is defined by

$$H_{CF} = \sum_{i=1}^N eV(r_i, \theta_i, \varphi_i) \quad (3.3)$$

where $eV(r_i, \theta_i, \varphi_i)$ represents the potential energy created by the surrounding ions, in the position $(r_i, \theta_i, \varphi_i)$ of the i -th electron of the studied ion (considering the position in spherical coordinates), and the summation is extended to the N valence electrons of the ion.

In order to avoid laborious calculations, it is possible to deduct the information of the system with the symmetry of the optical active center, through the group theory. With this method, it is possible to determine the number of the Stark sublevels in which a $^{2S+1}L_J$ level is split, but not the energetic position of each state. Moreover, this procedure is also useful to deduct the selection rules of the transitions within the generated Stark sublevels.

3.3 General selection rules: from forbidden to forced transitions.

Once the different energy states have been determined, it is necessary to study how an electron can pass from one state to the other, gaining (absorption) or giving energy (emission).

When an ion goes from an excited state to another at lower energy, the excess energy can be liberated in different ways, mainly by emission of photons and emission of phonons. The probability that an excited state would relax to another state radiatively (i.e. generating photons) is given by the coefficient of spontaneous emission of Einstein:

$$A = \frac{n\omega_0^3}{3\pi\hbar\epsilon_0c} |\mu|^2 \quad (3.4)$$

where n is the refraction index of the medium, c the speed of light in vacuum, ϵ_0 the vacuum permeability, μ is the element of the matrix of the dipolar electric moment, and ω_0 is the energetic distance between the initial and the final state, in frequency units. Since in the law ω is cubic, the probability of the transition will be as higher as bigger the energetic separation is.

On the other hand, the probability that the transition takes place non-radiatively (i.e., through the emission of lattice phonons) depends on the energy distance between one level and the immediately inferior one. In this way, the lower the energetic separation is, the higher is the probability of having a non-radiative transition.

In the Dieke diagram, the main radiative levels are marked with a small dot, thus the rest will present an important non-radiative component. As it can be noted, the radiative levels encounter a higher distance from the following excited level, in agreement with the just introduced equation.

However, in lanthanide ions, according to the general selection rules, the transitions between the states in the configuration $4f^n$ are parity forbidden (Laporte rule) and, as a consequence, there should not be any photonic emission observed from any transition. However, the emissions and the absorptions associated to these transitions are characteristic, show high intensities, generate very sharp lines and are well localized.

Various mechanisms have been suggested to explain the observed intensity of the transitions of the lanthanide ions. Molecular vibrations are too weak to relax sufficiently the parity forbidden selection rule. However, when the ions are inserted in a low symmetry site, there are interactions between the ions and the crystal field, and a mixture between opposite parity wave functions could take place (e.g. $4f^{n-1}5d$). The effect of this mixture is not sufficient to change the position of the energy states, but is enough to change the electric dipole transitions from forbidden to forced. As a consequence, the intensity of the emission is significantly enhanced.

3.4 Judd-Ofelt theory and radiative transitions.

In 1962, Judd and Ofelt studied simultaneously, and independently, the intensities of the spectral lines and they formulated a theory about the transition probabilities.

When calculating the transition probability between one level and another, either in a absorption or emission process, the main issue is encountered in the determination of the mixed initial and final states. For this purpose, in the case of lanthanide ions, the crystal field can be treated like a first order perturbation that creates states with a parity combination.

However, while applying this procedure, it is necessary to know in detail the parameters of crystal field and energies states and the eigenfunctions of the various configurations. Since this is a very complex problem, as previously said, the Judd-Ofelt theory applies a series of approximations with the aim of making the calculation more accessible:

- In an excited configuration, the splitting, due to the Stark effect in a multiplet, is negligible, compared with the configuration energy as a whole, i.e. the considered configurations are degenerate.
- The energy separation between the states of the main configuration, $4f^n$ and $4f^{n-1}5d$, are independent from the total angular momentum J , i.e. an average value can be used.
- The various Stark sublevels of each multiplet are homogeneously populated
- The material in which the lanthanide ions are incorporated is isotropic.

Although in some cases the first approximation could not be accurate, the results obtained through the Judd-Ofelt theory are acceptable, as they are in agreement with the values of a great number of matrices and ions.

The validity of the third approximation is temperature dependent, since the distribution of the population between the Stark levels depends on the Boltzmann distribution. In most of the cases, this approximation can be considered acceptable at room temperature and, as assumed, at higher temperatures, especially when the splitting in the Stark sublevels is little.

The last point makes the theory developed by Judd and Ofelt valid for only certain matrices. However it is possible to extend this study in anisotropic materials.

Through these approximations it is possible to obtain a simple expression for the intensity of the spectral lines in forced electric dipole transitions, S_{de} , which keeps in consideration the reduced matrix elements of the tensor operator of the free ion ($U^{(\lambda)}$).

$$S_{de} = \sum_{\lambda=2,4,6} \Omega_{\lambda} \left| \langle 4f^n(\gamma SL)J \| U^{(\lambda)} \| 4f^n(\gamma' S' L')J' \rangle \right|^2 \quad (3.5)$$

where Ω_{λ} are known as Judd-Ofelt intensity parameters, which determine the strength and the nature of the odd-parity crystal field.

The reduced matrix elements, referred to the free ion, as a combination of the Russell-Saunders states, are tabulated [118]. The Ω_{λ} parameters vary according to the ions and the matrix, but they are independent, in particular, from the $J - J'$ transition that characterize the force of the crystal field over the ion.

Starting from equation 3.5, and knowing the Judd-Ofelt parameters, it is possible to determine the intensity of the lines of all the transitions associated to a certain ion. Moreover, starting from the Judd-Ofelt theory, the selection rules for the $4f^n$ electric dipolar forced transitions have been derived:

- $\Delta J \leq 6$; $\Delta S = 0$, $\Delta L \leq 6$
- For a Ln^{3+} ion with an even number of electrons:

$J = 0 \leftrightarrow J' = 0$ is forbidden

$J = 0 \leftrightarrow$ odd J' values are weak

$J = 0 \leftrightarrow J' = 2, 4, 6$ should be strong.

3.5 Energy transfer

Energy transfer is the process where a previously excited ion relaxes, totally or partially, giving its energy to a second neighbouring ion, which inverts, transferring an electron from a state to a higher energy state. The first ion is called donor (sensitizer) and the second is called acceptor (or activator).

According to this definition, an energy transfer phenomenon could generate emission by direct excitation or by upconversion. Independently from the kind of process that occurs, in order to maintain the conservation of energy during the transfer, it is necessary that the emission band of the donor ion coincides, or overlaps, with the absorption band of the acceptor ion, in a certain range of wavelengths. However, in some cases, in which the overlapping between the two bands is absent or very small, it is still possible to observe energy transfer processes. In order for this process to occur, it is necessary to adjust the energy balance of the process, which can be achieved by taking or giving energy to the environment, where the ions are inserted, i.e. the matrix. Since in the lattice energy is available in form of phonons, these processes are called “phonon assisted”. In all the other cases, the process is called “resonant” (Figure 3.2).

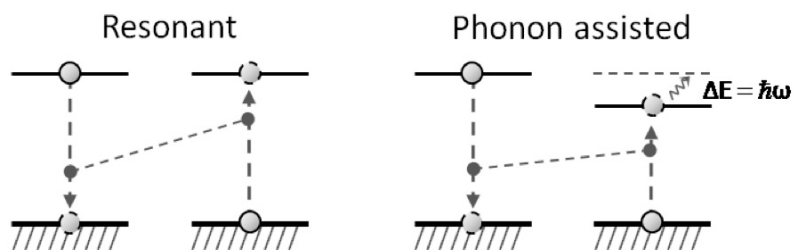


Figure 3.2: Resonant and phonon assisted energy transfers

For both resonant and non resonant phenomena, the energy transfer process can be classified according to the kind of interaction between the donor and the acceptor. Mainly, it can be defined radiative transfer, when the interaction occurs through the emission and the absorption of a photon, and non-radiative transfer, if this does not occur.

When the energy transfer occurs in radiative form, the donor ion relaxes emitting a photon that is, then, absorbed by an acceptor ion. For this reason, this process could be called “emission-reabsorption process”. This phenomenon occurs only between the same ions and it is common in matrixes doped with a high concentration of ions of the same element, with the assumption that the emission band of a transition of the donor overlaps the absorption band of the same transition of the acceptor ion.

On the contrary of what would be observed in presence of energy transfer, the emission from the donor ion varies during the emission-reabsorption process. In particular, the shape of the emission lines is affected accordingly to the concentration of the acceptor ions. The time necessary to the donor ion to delay its relaxation does not change. However, the radiative energy transfer does not excite simultaneously all the ions and, as a consequence, the experimental lifetime could be longer than in absence of transfer.

The simplest energy transfer processes usually involve transitions of acceptor ions that, from the ground state, populate an excited state. Because of the high population density of the ground level, these processes are the most probable. However, it is also possible that the acceptor ions would be in an excited state and they would originate a transition from the excited level.

There are different mechanisms that are responsible of the population density of the excited intermediate level of the acceptor ion, such as a direct excitation or the relaxation of the ion from a higher energy level. In some cases, it is possible that there is an existing energy transfer mechanism preceding the excitation of the acceptor ion, as it often occurs during upconversion emission mechanisms. In the same way, sometimes it is also possible that several consecutive energy transfer processes occur, as it happens during upconversion emissions in the visible, starting from infrared excitation.

The main mechanisms occurring during upconversion mechanisms are described in the following pages.

3.5.1 Excited state absorption (ESA)

In this case, a photon generated from the light source (pump photon) excites the ion to an intermediate excited level. Since this metastable state has a long lifetime, it is probable that it will be still populated as a second incoming pump photon excites the sample and consequently promotes the ion to the upper level, generating, as a consequence, an upconversion emission (Figure 3.3).

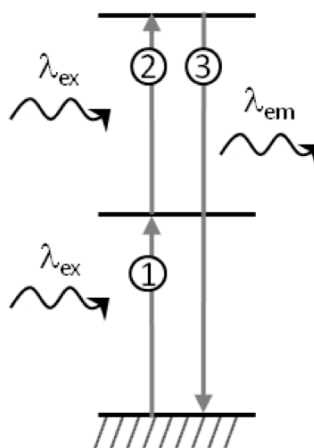


Figure 3.3: Excited state absorption mechanism

ESA mainly occurs when only a single ion is used as dopant and is typical of materials with low Ln^{3+} concentrations. The fact that the ion is initially in an excited state implies that, before the absorption of the photon, another process that populated this state must have happened. There are different mechanisms that can lead to this effect, but the most efficient is the one in which the ion is excited through direct absorption of another photon. In this case, the excited state absorption occurs through a sequential absorption of excitation photons.

3.5.2 Energy transfer upconversion (ETU)

Energy transfer is one of the most common energy transfer mechanisms for upconversion. In order for the mechanism to occur, the ions must be in close proximity. Therefore ETU is typical when the dopants are present in the matrix in high concentrations.

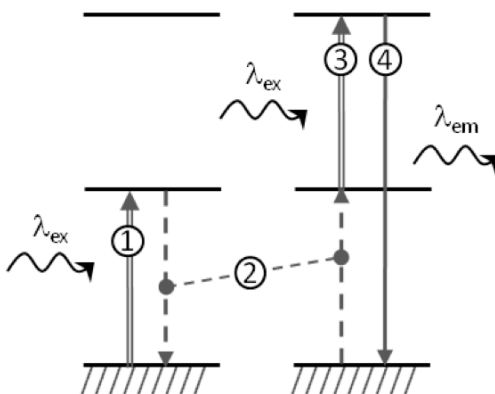


Figure 3.4: Energy Transfer Upconversion

In the ETU mechanism (Figure 3.4), the pump photon populates the intermediate excited state of the donor ion, which can promote an acceptor neighbouring ion through energy transfer to its intermediate state. Once the ion is in the intermediate state, a second photon coming from the excitation source, or from another neighbouring ion by energy transfer, is promoted to the excited state, from which the emission by upconversion occurs.

3.5.3 Cross relaxation (CR)

An alternative energy transfer mechanism is cross-relaxation (Figure 3.5), in which two neighbouring ions are both excited to the intermediate state by the pump photons. Subsequently, one ion acts as a donor, transfers its energy to the acceptor (3), which is promoted to the upper level, and returns non-radiatively to the ground state. From the upper excited the state, the emission by upconversion occurs.

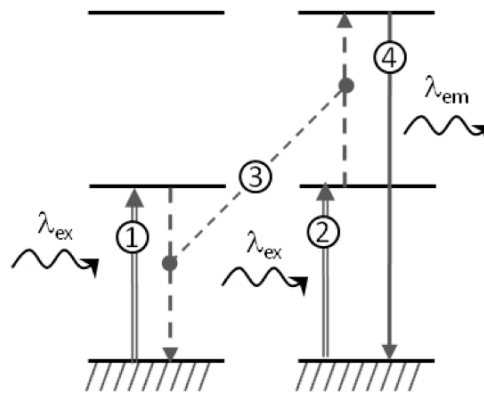


Figure 3.5: Cross-Relaxation mechanism

3.5.4 Photon avalanche (PA)

The phenomenon known as photon avalanche is a mechanism composed by an energy transfer process and an excited state absorption. Specifically, this mechanism generates upconversion intensity higher than the one generated with the other mechanisms.

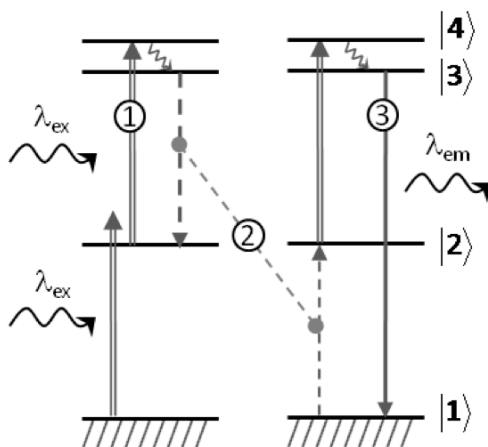


Figure 3.6: Photon Avalanche mechanism

In this mechanism (Figure 3.6), the excitation energy is not resonant with the transition between the ground level and the first excited state ($|1\rangle \rightarrow |2\rangle$), but the transition can occur, if phonon assisted. Since the excitation energy is resonant with the gap between the intermediate state ($|2\rangle$) and the higher one ($|4\rangle$), when the ions are in the first excited state ($|2\rangle$), the state at higher energy ($|4\rangle$) is easily populated.

Once the ion is in the $|4\rangle$ excited state, it relaxes non-radiatively to the state $|3\rangle$, which is energetically close to $|4\rangle$. From $|3\rangle$, the following step could be either a spontaneous relaxation to the lower energy states or a cross relaxation, as shown in Figure 3.6: ($|3\rangle \rightarrow |2\rangle : |1\rangle \rightarrow |2\rangle$).

Since the CR process is resonant, it will occur with high probability and, as a consequence, the ions, donor and acceptor, will eventually meet at the same intermediate level $|2\rangle$.

Following the described path, it is clear that starting from only one ion in the first excited state ($|2\rangle$), the PA mechanism generates ions with the same excited state (e.g. $|2\rangle$), duplicating, as a consequence, the probability that the ESA $|2\rangle \rightarrow |4\rangle$ will occur.

Consequently, all the process can continue occurring, separately, between two distinct ions. These two ions, when the CR occurs, involve other two ions, giving as a result four ions in the intermediate state $|2\rangle$. If all the process repeats several times, the final step has a high population density in the states $|2\rangle$ and $|3\rangle$, and the mechanism is self-sustaining.

As a result of all the consecutive processes, a very intense upconversion emission is generated from the level $|3\rangle$, which is one of the main characteristics of the PA process. This level of intensity is reached only starting from a certain excitation power, known as threshold power. When the threshold power is reached, the intermediate level ($|2\rangle$) is populated enough to start the generation of the avalanche.

3.6 Theory of the nozzles

The basics of the flame spray pyrolysis are now described. The texts of Knudsen [119] and Beek [120] have been taken as reference.

Nozzles are used to convert to kinetic energy part of the enthalpy or thermal content of a gas. This objective is obtained making the gas pass through a duct at variable section, maintaining the flow of the gas through the nozzle adiabatic.

The core of the flame spray pyrolysis is the nozzle of the burner, because its shape and configuration affects the flow dynamics of the gases and, as a consequence, the flame. The nozzle used in this work has a convergent-divergent shape.

In order to understand how this kind of nozzle affects the flame, a brief introduction on converging and diverging ducts is needed (Figure 3.7).

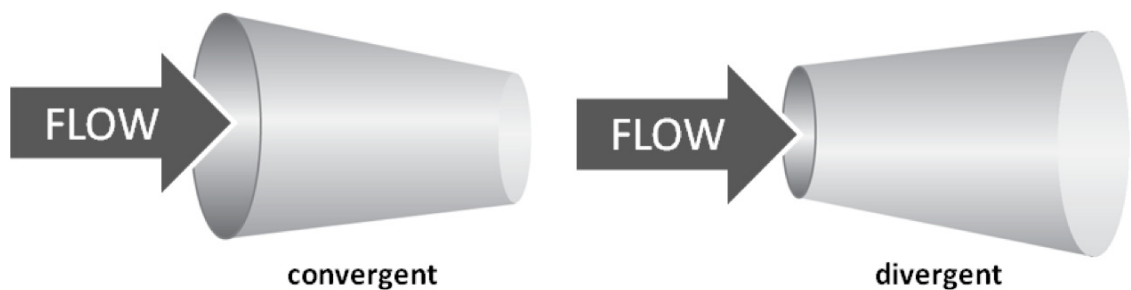


Figure 3.7: converging and diverging ducts.

The flow in ducts is determined by the following equation:

$$\frac{dv}{v} = -\frac{dA}{A} \frac{1}{(1 - Ma^2)} \quad (3.6)$$

Where v is the speed of the flow, A is the section area and Ma is the Mach number, defined as $Ma = \frac{v}{c}$, and c is the speed of sound.

The value of the Mach number defines the kind of flow passing through the nozzle: when $Ma < 1$ the flow is subsonic, when $Ma > 1$ the flow is supersonic and when $Ma = 1$ the flow is sonic.

In the case of subsonic flow ($Ma < 1$) velocity and section area change inversely, that is, when the section increases, the speed decreases, and vice-versa. This trend is consistent with the incompressible flow behaviour.

In the case of supersonic flow ($Ma > 1$) velocity and section change proportionally, that is, when the section increases the speed increases, and vice-versa.

In other words, a diverging duct will accelerate a supersonic flow, while a converging duct will accelerate a subsonic flow.

Now, combining the equation (3.6) with

$$-\frac{dv}{v} = \frac{d\rho}{\rho} + \frac{dA}{A} \quad (3.7)$$

we obtain:

$$-\frac{d\rho}{\rho} = \frac{dA}{A} \frac{Ma^2}{1 - Ma^2} \quad (3.8)$$

If we consider also the conservation of mass (continuity equation):

$$m = \rho Av = \text{constant} \quad (3.9)$$

and we consider a diverging duct, in case of subsonic flow ($Ma < 1$) at the increase of the section, the density increases as well (eq. 3.8) and, for the conservation of mass, the velocity must decrease. Therefore, with subsonic flow, velocity and section variation follow opposite variation.

On the other hand, in case of supersonic flow ($Ma > 1$) at the increase of the section, the density decreases and the velocity, for conservation of mass, must decrease. Therefore, with supersonic flow, velocity and section variation follow the same variation.

Equation 3.8, combined with the continuity equation, confirms what stated above.

Rearranging equation 3.6 with equation 3.8, we obtain:

$$\frac{dA}{dv} = -\frac{A}{v} (1 - Ma^2) \quad (3.10)$$

If $Ma = 1$, the condition of $\frac{dA}{dv} = 0$ is satisfied, which means that the area is at a minimum or at a maximum amount. This happens when two different types of ducts are combined sequentially: the section area has a minimum in a converging-diverging duct (Figure 3.8a), while it has a maximum in a diverging-converging duct (Figure 3.8b).

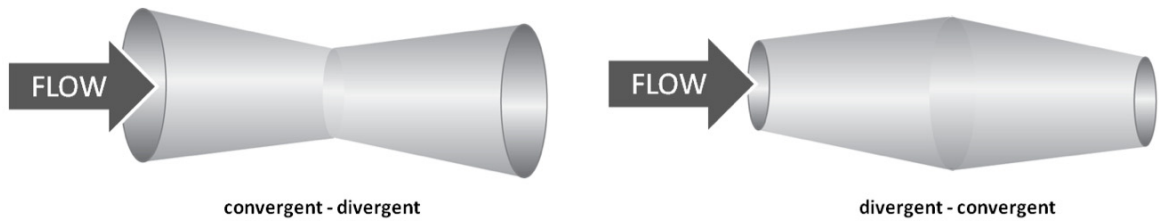


Figure 3.8: Converging-diverging duct (a) and diverging-converging duct (b).

Let us consider in detail the first case, the converging-diverging duct (Figure 3.9), which applies to the case of the nozzle in the burner.



Figure 3.9: converging-diverging duct and detail of the flow.

The flow enters the duct in subsonic flow ($Ma < 1$) in the converging section and the velocity increases until the section area reaches a minimum, where the flow is sonic ($Ma = 1$). While it is leaving the throat, the flow enters the diverging section of the duct in supersonic flow ($Ma > 1$) and the velocity increases as the section area increases. In other words, the converging-diverging area variation allows the achievement of supersonic flow from subsonic state.

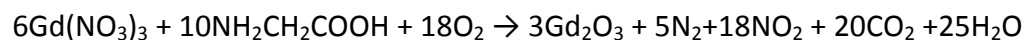
4. *Techniques*

4.1 Propellant Synthesis

Initially, the materials studied in this thesis have been prepared by using the propellant synthesis. In this method, stoichiometric amounts of $\text{Gd}(\text{NO}_3)_3$ and $\text{Er}(\text{NO}_3)_3$ are dissolved in an aqueous solution and mixed with glycine. The solution is heated over a Bunsen burner, in order to evaporate the excess of water. At the same time, glycine forms a gel and, when the ignition temperature is reached, a spontaneous ignition occurs. The products formed consist in a porous foamy powder. Although the temperature involved is high enough to allow the combustion to occur, the precursors are not often completely decomposed, probably because the combustion is not complete, and some brownish residues are left in the products. In order to avoid the formation of improper products, the powders undergo a thermal treatment (1 hour at 500°C) and, after this, they appear as a homogeneously white powder.

The temperature developed during the combustion reaction influences the particle size of the materials and can be modulated changing the ratio between fuel (glycine) and metal (nitrate precursors). In all the samples prepared in this thesis, the fuel/metal ratio has been kept at 1.2, in order to obtain particles with an average size of 20 nm.

The generic reaction of the propellant synthesis of G_2O_3 is:



Sample	Formula	Dopant concentration
Gadolinium Oxide	$\text{Gd}_2\text{O}_3:\text{Er}^{3+}$	0.1 %
		1 %
		10 %

Table 4.1: Samples prepared by Combustion Synthesis.

4.2 Flame Spray Pyrolysis Setup

In a second time, the luminescent materials have been prepared by Flame Spray Pyrolysis. The setup, shown in Figure 4.1, has been designed, made and assembled in the department of Chemistry and Biochemistry at Concordia University.

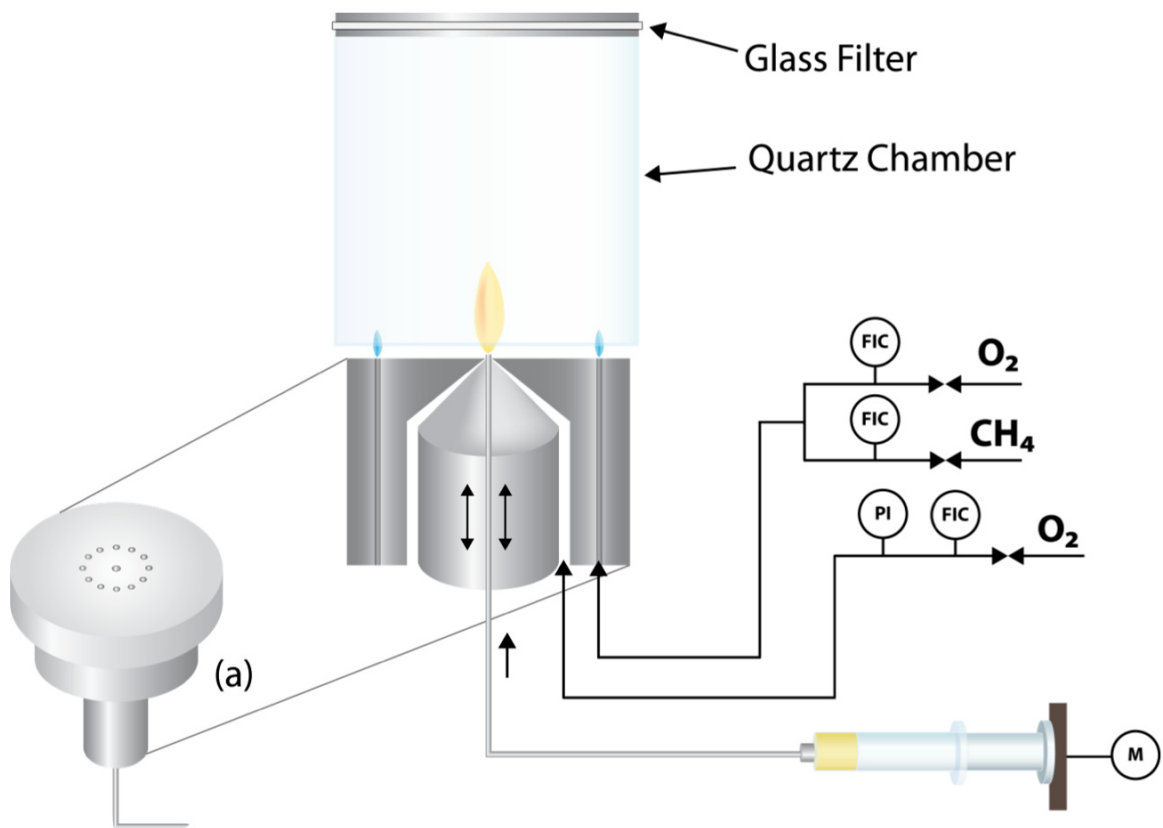


Figure 4.1: Schematic of the FSP setup

4.2.1 FSP synthesis

The FSP system used for this work has been inspired by the one described by Mädler et al [73]. A solution of metal precursors is injected with a syringe pump in the middle of the main nozzle of the burner, through a capillary tube. The solvent is combustible (e.g. propionic acid, 2-ethyl-hexanoic acid) and acts as a fuel and, with O₂, feeds the main central flame. Twelve flamelets, fed by a mixture of CH₄/O₂, surround the main flame, with the aim of igniting the combustion and maintain the stability of the central flame. As the solution is injected, it passes through the capillary tube and, when it reaches the end of the tube, each drop is dispersed by the oxygen of the main line in fine droplets. Instantaneously, the droplets are vaporized, while the precursors are burnt into metal oxide particles along the flame, going through nucleation, coagulation, coalescence and agglomeration. The nanocrystals so formed are collected on a glass microfiber filter, positioned at the top of the burner, with the aid of forced aspiration.

4.2.2 Burner

The burner is made by three concentric cylinders, the most important one being the central. This cylinder can move along the vertical axis of the burner and determines the aperture of the nozzle, which can be adjusted to vary the gas exit gap area from zero to a maximum of 0.433 mm². This affects the velocity of the gas at the exit (from subsonic to supersonic discharge) and, as a consequence, influences the dispersion of the precursors and the shape of the flame.

The aperture of the nozzle can be monitored with the pressure at the exit: when the nozzle is completely open the pressure drop is 0 bar and it increases as the nozzle is being closed. In order to measure the pressure drop at the exit of the line, a pressure gauge (0-10 atm) has been installed.

4.2.3 Materials

All the parts of the system are in stainless steel: the burner is in AISI 316 and the capillary tube ((Sigma Aldrich, $d=1.067\text{mm}$) is in AISI 304. To provide a better dispersion, the end of the capillary tube is positioned at a height of 0.5 mm from the burner.

4.2.4 Delivery of solution and gas

The rates of the solution and the gases affect the flame properties, such as shape and temperature, which is determined by the O_2/fuel ratio. Therefore, it is crucial to effectively regulate the settings of the system, not only for potential scaling up purposes, but also to have a proper control on the synthesis parameters.

The solution containing the precursors is injected with a syringe pump (Econoflow Harvard Apparatus, MA1 70-2205, syringe Popper micro-mate, 25 mL or 50 mL).

The gas flow rates of O_2 (Praxair, purity 99.993%) and CH_4 (Praxair, purity 99.0%) are independently controlled by mass flow regulators (MKS 1179A), managed by a control unit (MKS 247D). In order to avoid backfires in line, each gas line is equipped by a check valve.

4.2.5 Collection of nanocrystals

The produced powders pass through the quartz burner chamber (11.5 cm i.d., 30.5 cm L) and the product is collected on a glass microfiber filter (Whatman glass microfiber filter grade GF/A d = 15 cm).

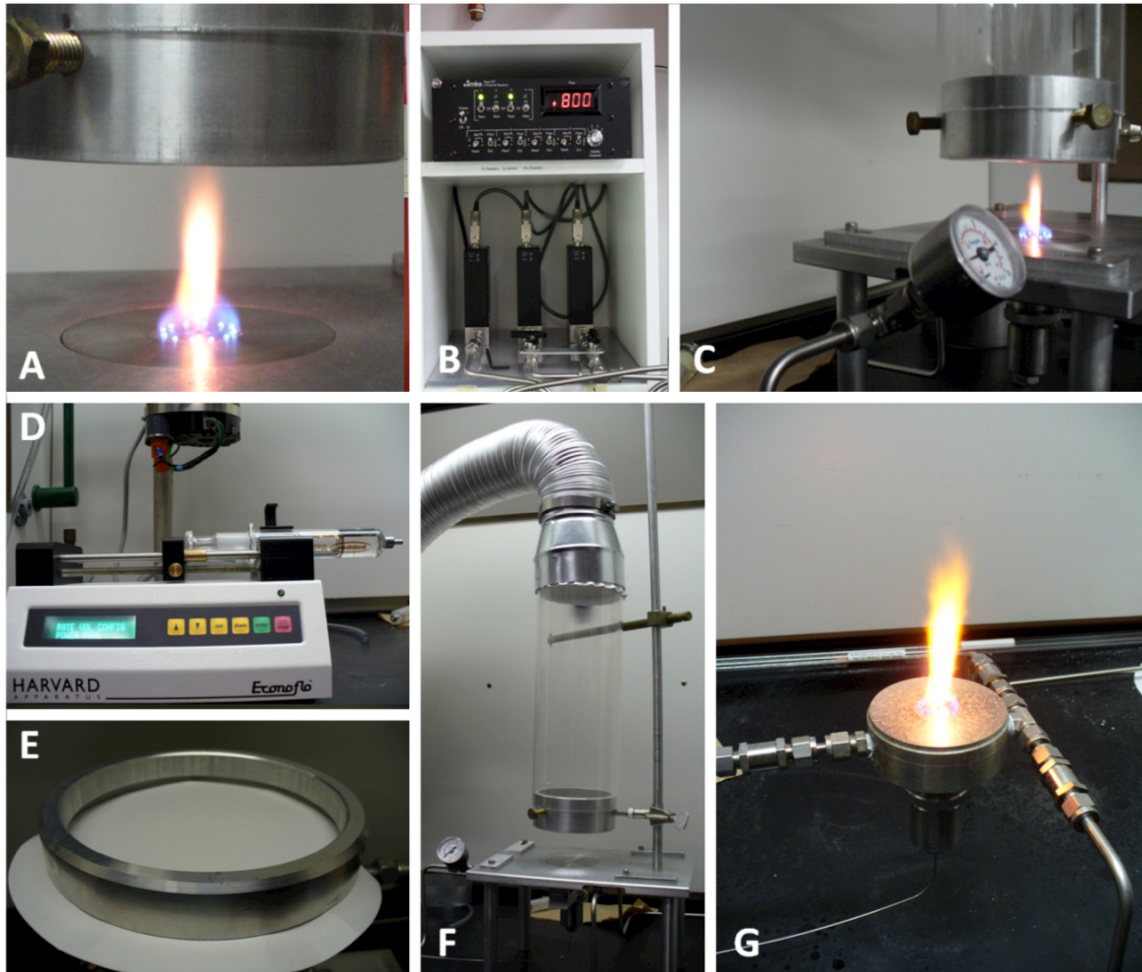


Figure 4.2: Details of the FSP synthesis setup. A: flame and flamelets, B: flowmeters and controller, C: flame and pressure gauge, D: syringe and syringe pump, E: glass fiber filter, F: collection of particles, G: flame and burner detail (note the concentric cylinders at the bottom of the burner).

4.3 Precursors Solution

Stoichiometric quantities of metal precursors are dissolved in 25 mL or 50 mL of organic solvents, in order to obtain a 0.1 M solution, under stirring at 60°C for 15 min.

The metal precursors and the organic solvent used in this work are summarized in the following tables.

Name	Formula	Details	Product
Gadolinium Acetate	$\text{Gd}(\text{CH}_3\text{COO})_3 \cdot 4\text{H}_2\text{O}$	Sigma Aldrich, purity 99.9%	Gd_2O_3
Gadolinium Nitrate	$\text{Gd}(\text{NO}_3)_3 \cdot 6\text{H}_2\text{O}$	Sigma Aldrich, p. 99.99%	Gd_2O_3
Tetraethyl orthosilicate	$\text{Si}(\text{OC}_2\text{H}_5)_4$	Sigma Aldrich, purity 99 %	SiO_2
Vanadyl acetylacetonate	$(\text{CH}_3\text{COO})_2\text{VO}$	Sigma Aldrich, purity 98%	GdVO_4

Table 4.2: Metal Precursors

Name	Formula	Details	Ln^{3+}
Erbium Acetate	$\text{Er}(\text{CH}_3\text{COO})_3 \cdot 4\text{H}_2\text{O}$	Sigma Aldrich, purity 99.9%	Er^{3+}
Erbium Nitrate	$\text{Er}(\text{NO}_3)_3 \cdot 5\text{H}_2\text{O}$	Sigma Aldrich, purity 99.9%	Er^{3+}
Ytterbium Acetate	$\text{Yb}(\text{CH}_3\text{COO})_3 \cdot 4\text{H}_2\text{O}$	Sigma Aldrich, purity 99.9%	Yb^{3+}
Ytterbium Nitrate	$\text{Er}(\text{NO}_3)_3 \cdot 5\text{H}_2\text{O}$	Sigma Aldrich, purity 99.9%	Yb^{3+}

Table 4.3: Lanthanide ion precursors

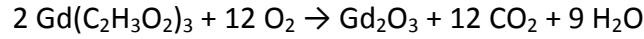
Name	Formula	Details	M^+
Lithium acetate	$\text{Li}(\text{CH}_3\text{COO}) \cdot 2\text{H}_2\text{O}$	Sigma Aldrich, purity 99.95%	Li^+
Sodium acetate	$\text{Na}(\text{CH}_3\text{COO})$	Sigma Aldrich, purity 99.0%	Na^+
Potassium acetate	$\text{K}(\text{CH}_3\text{COO})$	Sigma Aldrich, purity 99.0%	K^+

Table 4.4: Alkali metal ion precursor

Name	Formula	Details
2-Ethyl-hexanoic acid	$\text{CH}_3(\text{CH}_2)_3\text{CH}(\text{C}_2\text{H}_5)\text{CO}_2\text{H}$	Sigma Aldrich, purity > 99%
Propionic acid	$\text{CH}_3\text{CH}_2\text{COOH}$	Sigma Aldrich, purity 99.5%
Ethanol	EtOH	Sigma Aldrich, purity 99.8%
Xylene	$\text{C}_6\text{H}_4(\text{CH}_3)_2$	Sigma Aldrich, purity 98.5%
Toluene	$\text{C}_6\text{H}_5\text{CH}_3$	Sigma Aldrich, purity 99.8%

Table 4.5: Solvent (fuel)

The generic combustion reactions that occurs during the FSP for the production, for example of Gd₂O₃, is



Sample	Formula	Dopant concentration (%)	Solution rate (mL/min)	O ₂ rate (L/min)	ΔP (bar)		
Gadolinium Oxide	Gd ₂ O ₃ :Er ³⁺	0.1	2.00	2.00	2.00		
		1					
		10					
		1.00					
		1.33					
Gadolinium Oxide	Gd ₂ O ₃ :Er ³⁺	1	2.00	2.00	2.00		
			2.00	1.33	2.00		
			2.00	1.50	2.00		
			2.00	3.00	2.00		
			2.00	4.00	2.00		
			2.00	2.00	0.00		
			2.00	2.00	4.00		
			2.00	2.00	4.00		
Gadolinium Oxide	Gd ₂ O ₃ :Er ³⁺ , Yb ³⁺	Er ³⁺ :1 Yb ³⁺ :1	2.00	2.00	2.00		
Gadolinium Oxide	Gd ₂ O ₃ :Er ³⁺ , Yb ³⁺ , Li+	Er ³⁺ :1 Yb ³⁺ :1, Li ⁺ :1	2.00	2.00	2.00		
						Gd ₂ O ₃ :Er ³⁺ , Yb ³⁺ , Na+	Er ³⁺ :1 Yb ³⁺ :1, Na ⁺ :1
						Gd ₂ O ₃ :Er ³⁺ , Yb ³⁺ , K+	Er ³⁺ :1 Yb ³⁺ :1, K ⁺ :1
Gadolinium Oxide	Gd ₂ O ₃ :Er ³⁺ , Yb ³⁺ , Li+	Er ³⁺ :1 Yb ³⁺ :1	2.00	2.00	2.00		
Gadolinium Vanadate	GdVO ₄ :Er ³⁺ , Yb ³⁺	Er ³⁺ :1 Yb ³⁺ :1	2.00	2.00	2.00		

Table 4.6: Samples prepared by FSP

4.3.1 Preparation of the core/shell nanoparticles

A solution containing the synthesized core (e.g. $\text{Gd}_2\text{O}_3:\text{Er}^{3+},\text{Yb}^{3+},\text{M}^+$ or Fe_2O_3) is dissolved in ethanol with the stoichiometric amount of the shell nitrate precursor, in order to obtain a 0.1 M concentration. The solution is sonicated for 30 min to guarantee a good dispersion of the synthesized core. This precursor solution is then injected in the flame, following the usual procedure.

Sample	Formula	Dopant concentration (%)
Core: Gadolinium Oxide Shell: Silica	$\text{Gd}_2\text{O}_3:\text{Er}^{3+}, \text{Yb}^{3+}, \text{Li}^+@\text{SiO}_2$	$\text{Er}^{3+}:1 \text{ Yb}^{3+}:1, \text{Li}^+: 1$

Table 4.7: Core-shell samples prepared by FSP

4.4 Thermodynamics calculations

Considering the kind of syntheses employed in this work, the thermodynamics of the reaction plays an important role on the final products. Mainly, two values are considered: the volumetric enthalpy of combustion and the equivalence ratio.

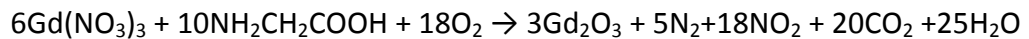
4.4.1 Volumetric Enthalpy of Combustion, ΔH_{CV}

For the FSP, the enthalpy of combustion is expressed as the enthalpy change during the combustion, relative to the volume of oxygen reacted, and it is measured in KJ/L_{O_2} . The ΔH_{CV}° is calculated as follows:

$$\Delta H_{CV}^\circ = \frac{\Delta H_{C(EHA)}^\circ \cdot d_{(EHA)} \cdot rate_{(EHA)}}{MW_{(EHA)} \cdot rate_{(O_2)}}$$

According to this calculation, the rate of solvent (EHA) and the rate of oxygen are inversely proportional.

For the propellant synthesis, the reaction occurring must be considered:



For comparison with the FSP, the enthalpy must be expressed in volumetric combustion enthalpy. Assuming to be in ideal conditions, this can be done as follow:

$$\Delta H_{CV}^\circ = \frac{\Delta H_{C(fuel)}^\circ}{volume_{(O_2)}} = \frac{\Delta H_{C(gly)}^\circ \cdot \frac{V_{(gly)}}{V_{(O_2)}} \cdot d_{(O_2)}}{MW_{(O_2)}}$$

The term $\frac{v_{(gly)}}{v_{(O_2)}}$ is the ratio between the stoichiometric coefficients of glycine and oxygen. However, as said previously, the ratio between fuel and oxidant $\frac{v_{(gly)}}{v_{(Gd)}}$ used in this work is 1.2, which is less than the stoichiometric ratio, 1.6. Therefore, the value of the ratio between glycine and oxygen, which is used to obtain ΔH°_{cv} , must be corrected, accordingly to the experimental conditions, to $\frac{v_{(gly)}}{v_{(O_2)}} = 0.42$.

4.4.2 Equivalence ratio, Φ

The equivalence ratio, Φ , is defined as the ratio between the oxidizer to fuel ratio and the stoichiometric oxidizer to fuel ratio:

$$\Phi = \frac{n_{OXIDIZER}/n_{FUEL}}{(n_{OXIDIZER}/n_{FUEL})_{stoich.}}$$

When $\Phi = 1$, the mixture is stoichiometric and the combustion synthesis is complete, when $\Phi < 1$, the mixture is fuel rich and the combustion is complete and, finally, when $\Phi > 1$, the mixture is fuel lean and the combustion is not complete.

For the propellant synthesis, the equivalence ratio is calculated as follow:

$$\Phi_{COMB} = \frac{n_{O_2}/n_{gly}}{(n_{O_2}/n_{gly})_{stoich.}}$$

As said previously, in the experimental conditions used for this work, the ratio between glycine and oxygen is 0.42. Therefore, $\Phi_{COMB} = 1.32$ for any propellant synthesis carried in this work. .

For the FSP, the equivalence ratio is calculated as follow:

$$\Phi_{\text{FSP}} = \frac{n_{\text{O}_2}/n_{\text{fuel}}}{(n_{\text{O}_2}/n_{\text{fuel}})_{\text{stoich.}}} = \frac{\frac{\text{rate}_{\text{O}_2} \cdot d_{\text{O}_2}}{MW_{\text{O}_2}}}{\frac{\text{rate}_{\text{fuel}} \cdot d_{\text{fuel}}}{MW_{\text{fuel}}}}$$

and the values of Φ_{FSP} vary according to the experimental settings of each synthesis.

4.5 Characterization

4.5.1 X-ray Powder Diffraction measurement and analysis

XRPD patterns are measured using a diffractometer (Scintag XDS-2000) equipped with a Si(Li) Peltier-cooled solid state detector, CuK α source at a generator power of 45 kV and 40 mA, divergent beam (2mm and 4mm) and receiving beam slits (0.5 m and 0.2 mm). Scan range is set from 20-80° 2 θ with a step size of 0.02° and a count time of 6 s. The sample is measured using a quartz “zero background” disk. The patterns are analyzed according to the Rietveld method using the MAUD program, under the assumption of isotropic peak broadening.

The particle size has been calculated by Scherrer equation:

$$d = \frac{k\lambda}{\beta \cos \theta}$$

Where d is the size of the crystallite, k is a constant dependent on the crystallite shape (0.89 for spherical crystals without cubic symmetry), λ is the X-Ray wavelength (0.154 nm), β is the Full Width at Half Maximum (FWHM) and θ is the Bragg angle.

4.5.2 Transmission Electron Microscopy (TEM)

TEM and ED analyses of the powder of nanoparticles are performed with a microscope (Philips CM200), operating at 200 kV equipped with a charge-coupled device (CCD) camera (Gaten). Prior to analysis, a minute amount of sample is dispersed through sonication for 30 min in an appropriate amount of ethanol to yield an approximate 0.1wt % solution. A drop of the resulting solution is evaporated on a formvar/carbon film supported on a 300 mesh copper grid (3mm in diameter).

4.5.3 Scanning Electron Microscopy (SEM) analyses

SEM analyses are taken with a Field Emission Gun Scanning Electron Microscope (Hitachi S-4700 FEGSEM). In order to avoid charging effects, the samples are Au-Pd coated (Anatech Hummer VI Sputter coater).

4.5.4 Thermogravimetric analysis (TGA and DTA)

TGA analysis has been carried on a Seiko Instrument Inc. TG/DTA6200. A known amount of sample is placed on the platinum crucible and, under N₂, it is thermally treated from room temperature to 1000°C, with a temperature program of 10°C/min.

4.5.5 Luminescence measurements

The setup for the luminescence measurements of the samples is described in Figure 4.4. Upconversion emission spectra have been collected after excitation with 978 nm wavelength laser diode (Coherent fiber-coupled F6 series, maximum power of 800 mW), coupled to a 100 μm (core) fiber.

For all the studies, the powder samples are firmly packed in a capillary tube ($d = 1\text{mm}$), which is fixed in a sample holder on a micropositioning adjustable stand (Oriol). A camera lens (Mamiya/Sekor, $f=55\text{ mm}$) has been used to focus the emissions, which are collected at right angle with respect to the incident beam.

The emitted light is dispersed by a 1m double monochromator (Jarrell-Ash Czerny-Turner) with an optical resolution of $\sim 0.25\text{ nm}$. The visible emissions are detected by a thermoelectrically cooled photomultiplier tube (Hamamatsu R943-02). The signal detected by the PMT is then amplified with a SR440 Standard Research Systems preamplifier (SR440 Standard Research Systems) and processed by a gated photon counter (SR400 Standard Research Systems). The signal is recorded under computer control using the software data acquisition/analyzer system (Standard Research Systems SR465).

The lifetimes (Figure 4.3) were measured by exciting the sample directly with the third harmonic (355 nm wavelength), generated from a pulsed Nd-YAG laser (Spectra Physics, Quanta-Ray INDI). The signal is detected with the same photomultiplier tube and analyzed with a two channel digital oscilloscope (Tektronix TDS 520A).

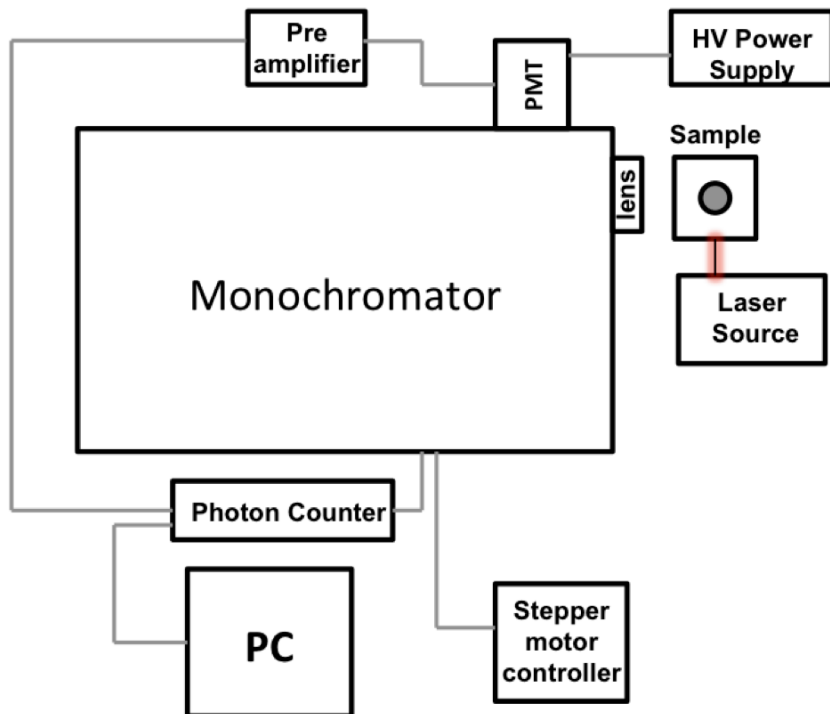


Figure 4.3: Experimental setup for decay times measurements.

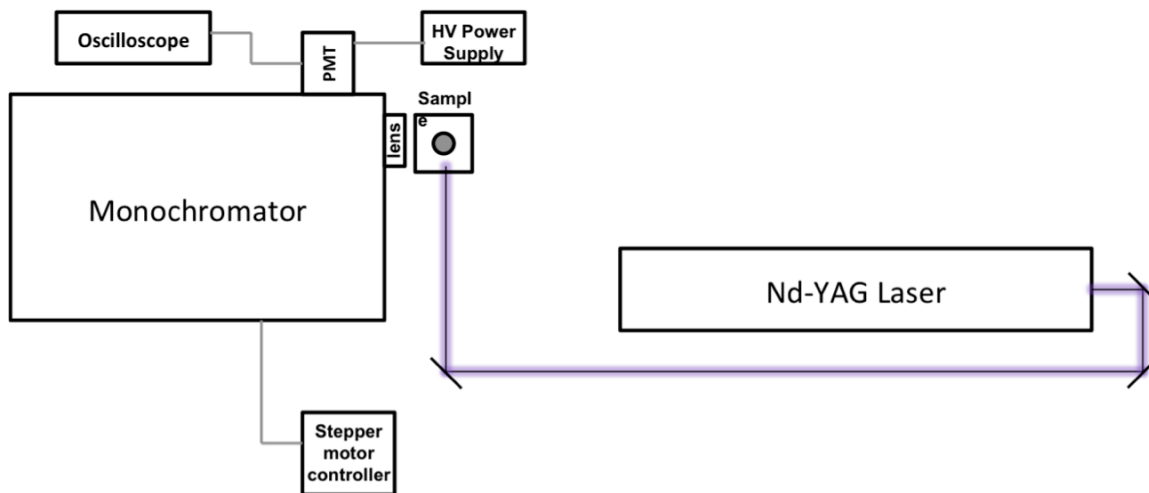


Figure 4.4: Experimental setup for UC emission measurements.

5. *Results and Discussion*

5.1 From Combustion synthesis to FSP

This work focuses mainly on the development of a new technique for the preparation of luminescent nanomaterials, flame spray pyrolysis. Therefore, at the beginning of this thesis, it was necessary to compare the new synthesis with a well-known technique, combustion synthesis, in order to observe similarities, differences and improvements. For the purpose of focusing only on the synthesis, the first system studied was a simple binary oxide, Gd_2O_3 , doped with only Er^{3+} .

5.1.1 Combustion synthesis: phase purity and morphology

Firstly, a series of samples with different concentrations of Er^{3+} have been prepared by combustion synthesis, with the aim to study the effects of the dopant concentration on the luminescence emission of the nanocrystals. Glycine has been used as a fuel and the amount of Er^{3+} used was 0.1, 1 and 10%. All the samples, as prepared, were brownish and, as a consequence, they have been treated at 500°C for 2 h, in order to eliminate the organic residues [67]. After the treatment, the solids were white and have been used, without further treatments, for their characterization.

The diffraction pattern of the XRPD analysis (Figure 5.1) revealed the presence of monoclinic gadolinium oxide (Gd_2O_3). The Bragg reflections matched those of the monoclinic phase of the un-doped reference material (JCPDS no. 160226), even if a minor component of cubic phase (ICSD 41270) has been found (2% by Rietveld refinement).

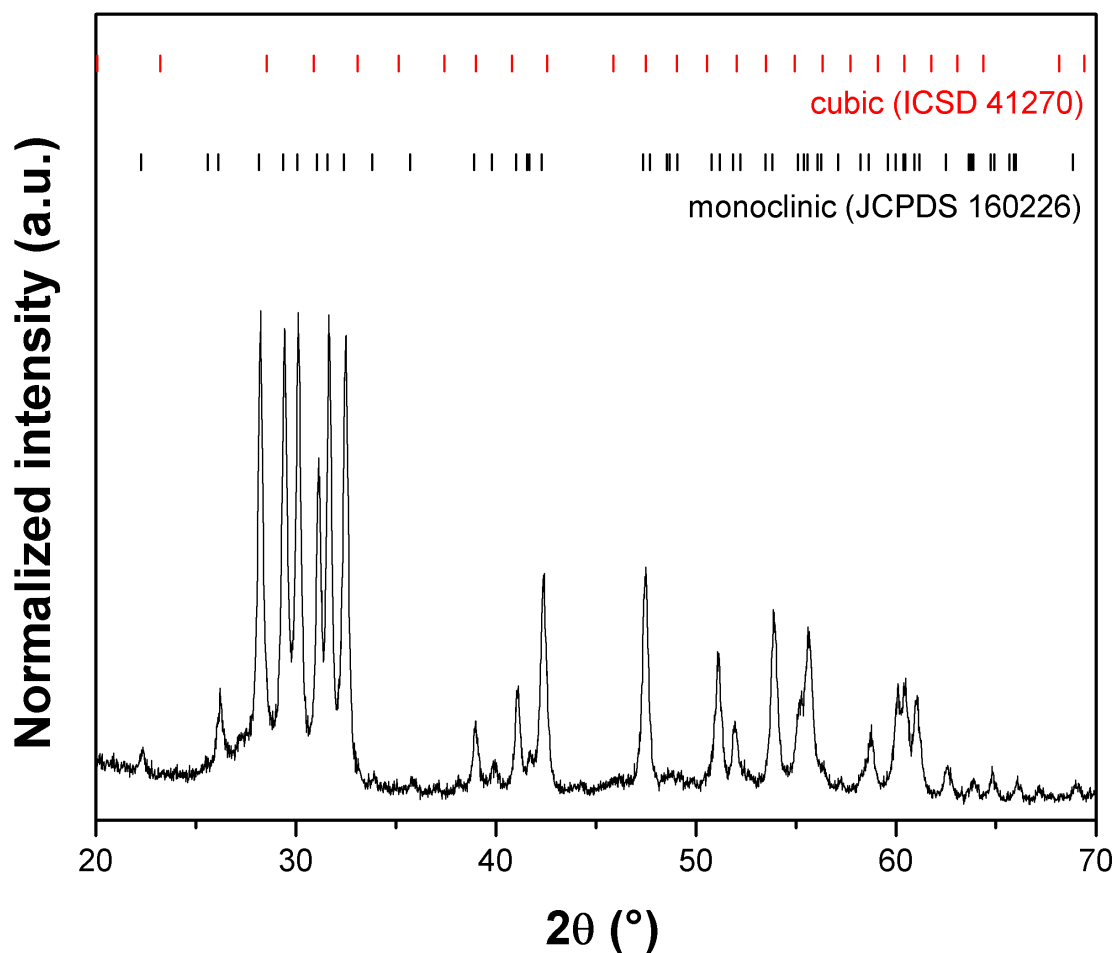


Figure 5.1: XRPD of $\text{Gd}_2\text{O}_3:\text{Er}^{3+}$ prepared by propellant synthesis

Furthermore, an analysis of the XRPD patterns was used to evaluate the crystallite size of the nanocrystalline $\text{Gd}_{2-x}\text{Er}_x\text{O}_3$ powders, using Scherrer's equation. The crystallite size was determined to be approximately 25 nm, in agreement with the data reported using a fuel/oxidizer ratio of 1.2 [121] and with the electron microscopy results (Figure 5.2).

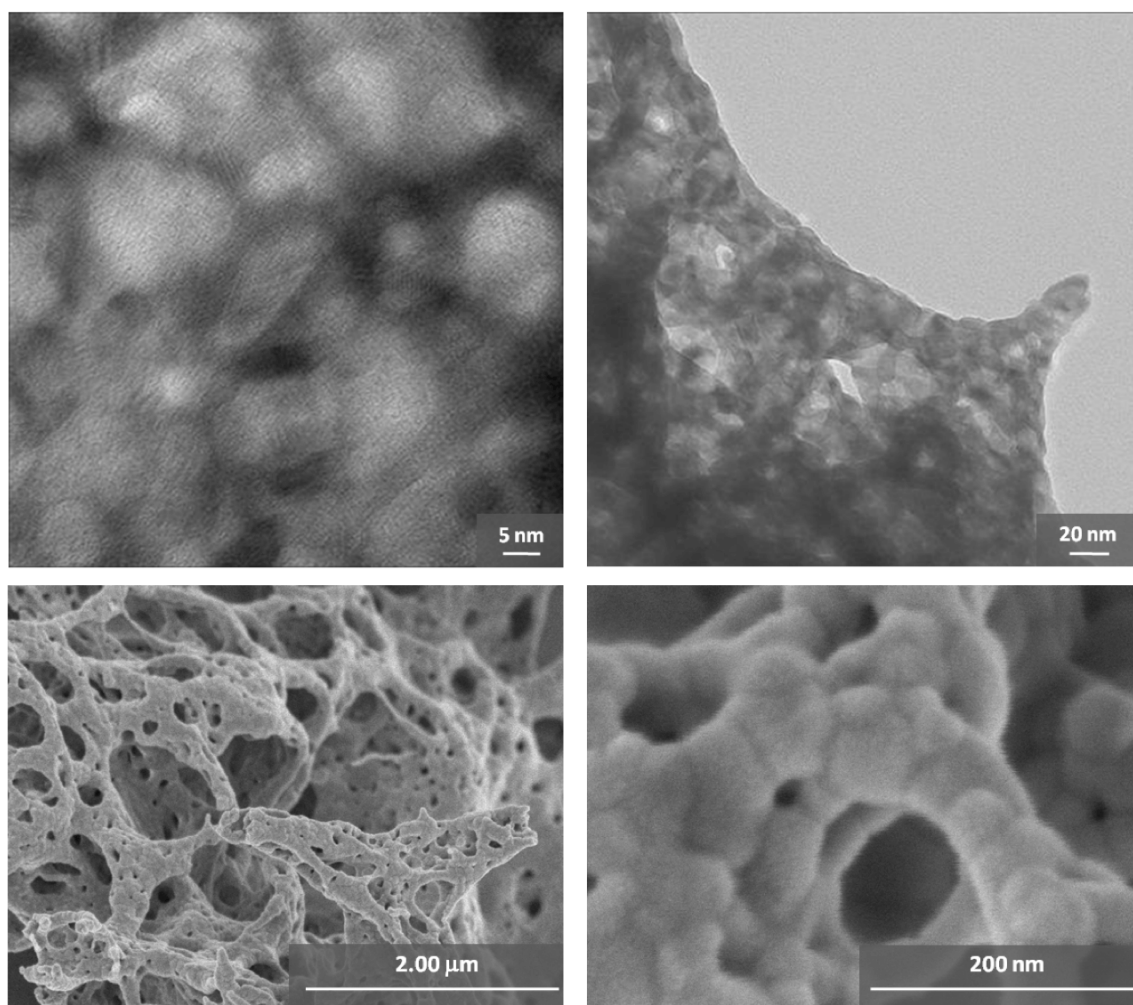


Figure 5.2: TEM (top) and SEM (bottom) images of $\text{Gd}_2\text{O}_3:\text{Er}^{3+}$ prepared by propellant synthesis

Scanning electron microscopy (SEM) and transmission electron microscopy (TEM) analysis of the $\text{Gd}_{2-x}\text{Er}_x\text{O}_3$ nanocrystals showed that the nanocrystals obtained by propellant synthesis were very porous with an open microstructure (Figure 5.2), similar to the ones observed for nanocrystalline yttria prepared using the same propellant synthesis [122].

The SEM images revealed the sponge-like structure, typical of the powders prepared by this technique. On the other hand, TEM images confirmed the high crystallinity of the samples through the clearly visible lattice fringes. However, they showed also how the structure of these samples is so compacted that it is almost impossible discern between the single particles.

5.1.2 Flame Spray Pyrolysis: Phase purity and morphology

In order to have a better control on the synthesis and produce more homogeneous nanocrystals, it has been developed a flame spray pyrolysis system. This high temperature synthesis not only allows a better control of the products properties, but it also occurs in one step, without the need of a subsequent thermal treatment [123].

The morphology of the prepared products is showed in Figure 5.3. The SEM images clearly present homogeneous and quasi-spherical nanocrystals, which are very different from the ones previously observed with combustion synthesis (Figure 5.3).

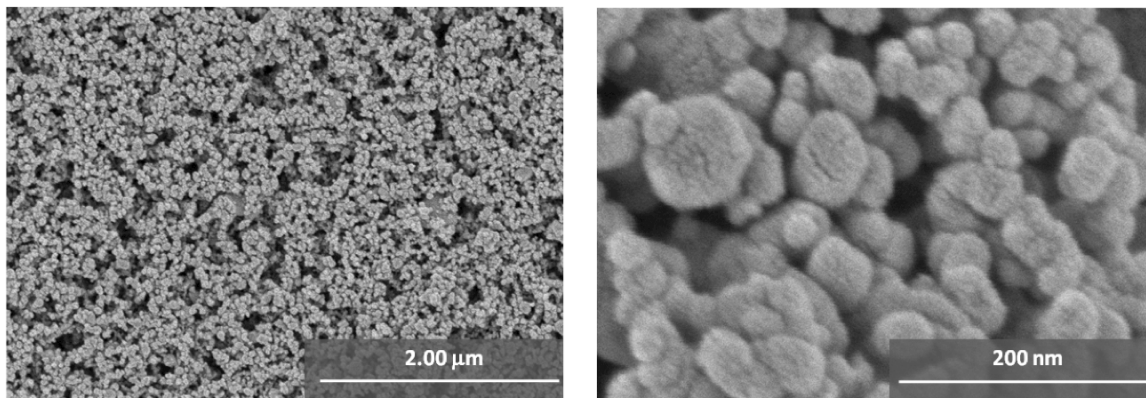


Figure 5.3: SEM images of $\text{Gd}_2\text{O}_3:\text{Er}^{3+}$ prepared by FSP

This morphology is in agreement with the controlled operation of the synthesis: the precursor solution is injected into the flame drop by drop, while in the case of the propellant synthesis an uncontrolled explosion occurs. The ability to produce samples with this kind of homogeneity makes FSP an appealing technique for the production of phosphors for displays.

Furthermore, the agglomeration observed in the nanocrystals produced by FSP was less compact than the one for the samples prepared by propellant synthesis. In fact, the higher dispersion that occurs when the precursors are injected into the flame of the FSP most likely prevents the massive agglomeration observed in the samples prepared by propellant synthesis. As observed with combustion synthesis, also the samples prepared by FSP showed high crystallinity, as it can be observed with the visible lattice fringes.

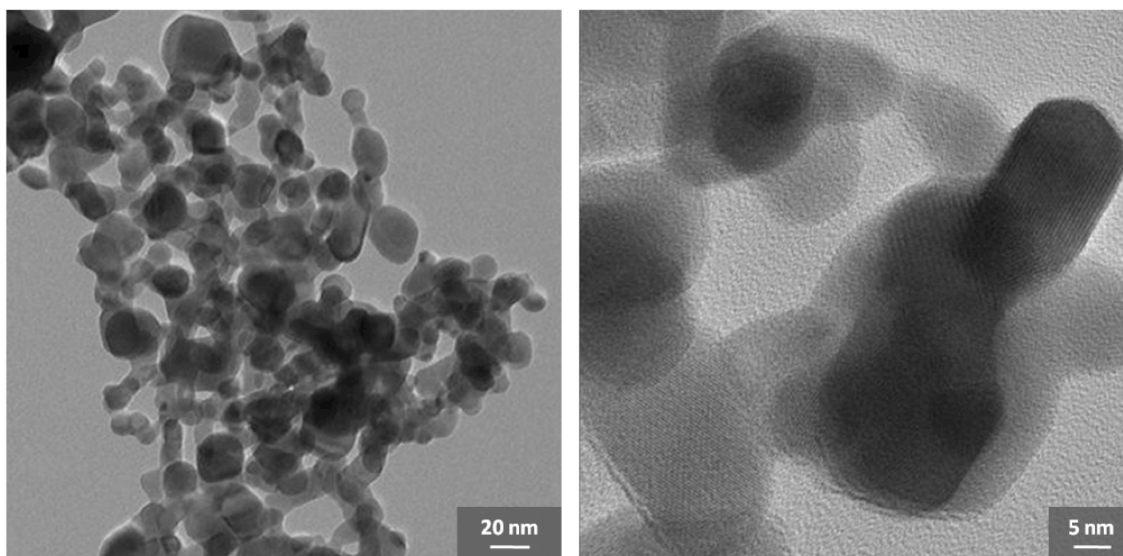


Figure 5.4: TEM images of Gd₂O₃:Er³⁺ prepared by FSP

In agreement with these results, the XRPD pattern (Figure 5.5) showed a monoclinic Gd_2O_3 phase, similarly to what found with the samples prepared by propellant synthesis, with a purity of 92% and a particle size of about 20 nm, as calculated from Rietveld refinement. The presence of a higher amount of cubic Gd_2O_3 phase in the sample prepared by FSP is most likely due to the fact that the temperature profile involved in the FSP favours the production of metastable systems [109].

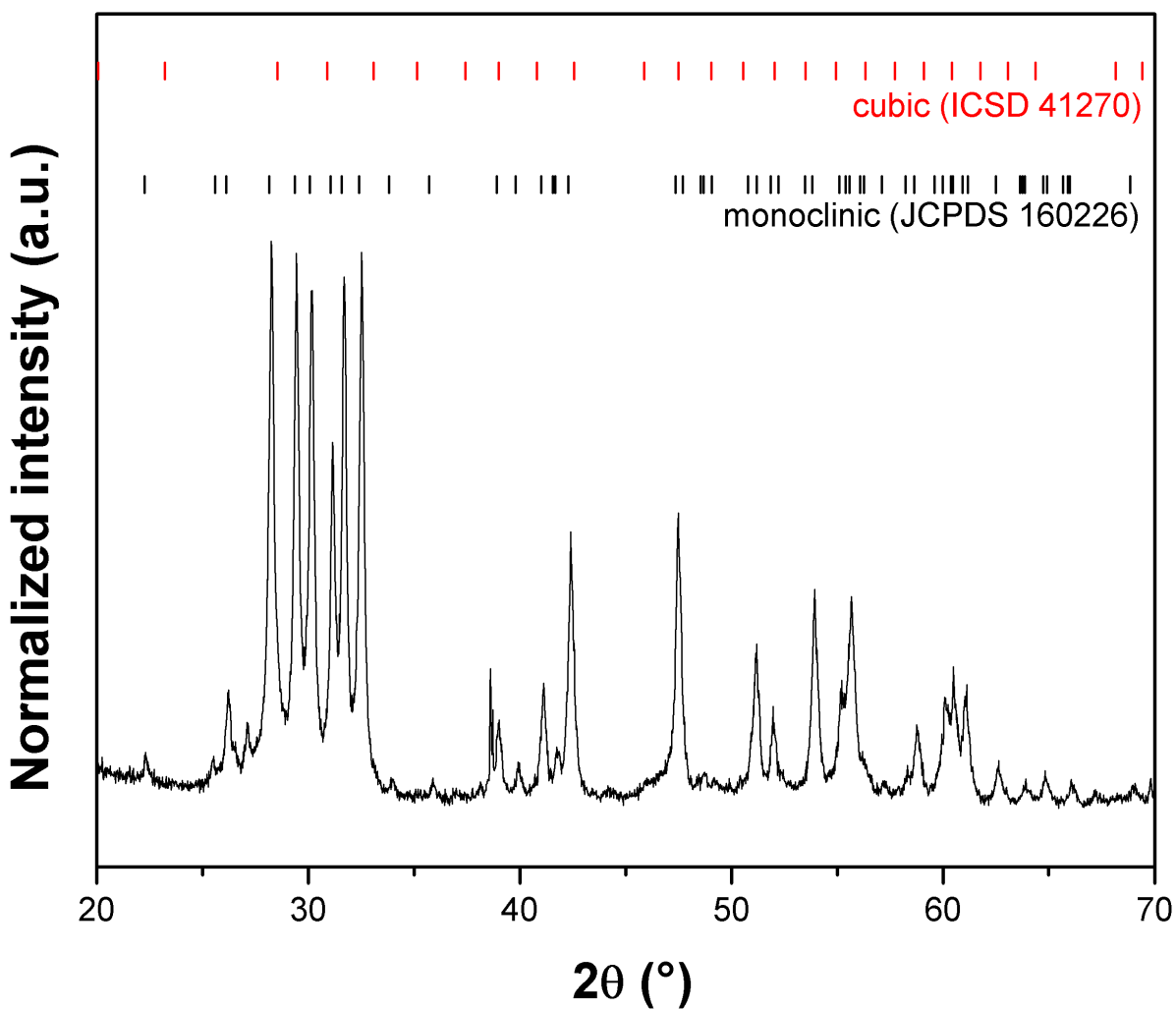


Figure 5.5: XRPD pattern of $\text{Gd}_2\text{O}_3:\text{Er}^{3+}$ prepared by FSP

5.1.1 Thermodynamics of the two synthesis

To understand the thermodynamics involved, the enthalpy in both the reactions was calculated, expressing the combustion enthalpy of the liquid fuel relative to the gas volume used. For combustion synthesis, the volumetric combustion enthalpy is -16 KJ/L, while for FSP it is -36 KJ/L (Table 5.1). The higher volumetric combustion enthalpy involved in FSP relates to the more elevated reaction temperature developed during the synthesis, resulting in nanocrystals with higher thermal stability and a decrease in residues.

	Propellant synthesis	Flame Spray Pyrolysis
Fuel	Glycine	90 % Xylene (in 2-Ethyl-Hexanoic Acid)
ΔH_c (kJ/mol)	-975	-4008
$\Delta H_c/L_{O_2}$ (kJ/L _{O₂})	-16	-36
Φ	1.3	0.3

Table 5.1: The combustion enthalpies of the propellant and FSP syntheses.

For the propellant synthesis, the oxygen amount depends on the stoichiometric ratio between the fuel and the oxidant, which in our case was 1.2. For the calculations, it was assumed that the amount of oxygen consumed during the reaction was stoichiometric. In the case of FSP, the amount of oxygen involved depends on the gas flow rate set during the synthesis.

Therefore, the equivalence ratio, Φ , was calculated to know if the mixtures were fuel rich ($\Phi < 1$) or fuel lean ($\Phi > 1$). For the propellant synthesis, this ratio, in the stoichiometric conditions employed ($\frac{v_{(gly)}}{v_{(Gd)}} = 1.2$), is 1.32 (Table 5.1). This indicates that the mixture used is fuel lean and leads to incomplete combustion, as it can be observed from the brownish residues present on the NCs, due to the presence of unburnt species. For FSP, the value of Φ is 0.3. This indicates that the mixture is fuel rich and, as a consequence, that a complete combustion occurs. In support of this, the NCs prepared by FSP were white as prepared and did not show the presence of major quantities of unburnt species.

While the ratio between oxygen and fuel flow rates cannot be modified in the propellant synthesis, FSP allows the variation of the settings, which affect the final properties of the products, such as particle size, upconversion intensity and phase purity. A systematic study of these variables will be the subject of the following chapter.

5.1.2 Luminescent properties of the nanocrystals

Following excitation into the $^4I_{11/2}$ state using 980 nm laser radiation, both green and red upconverted emissions were observed for all nanocrystalline samples, prepared by either propellant synthesis or FSP (Figure 5.6). As it can be observed from the spectra, the upconverted luminescence centered at 527, 552 and 665 nm was attributed to transitions from the $^2H_{11/2}$, $^4S_{3/2}$ and $^4F_{9/2}$ excited states to the ground state ($^4I_{15/2}$), respectively.

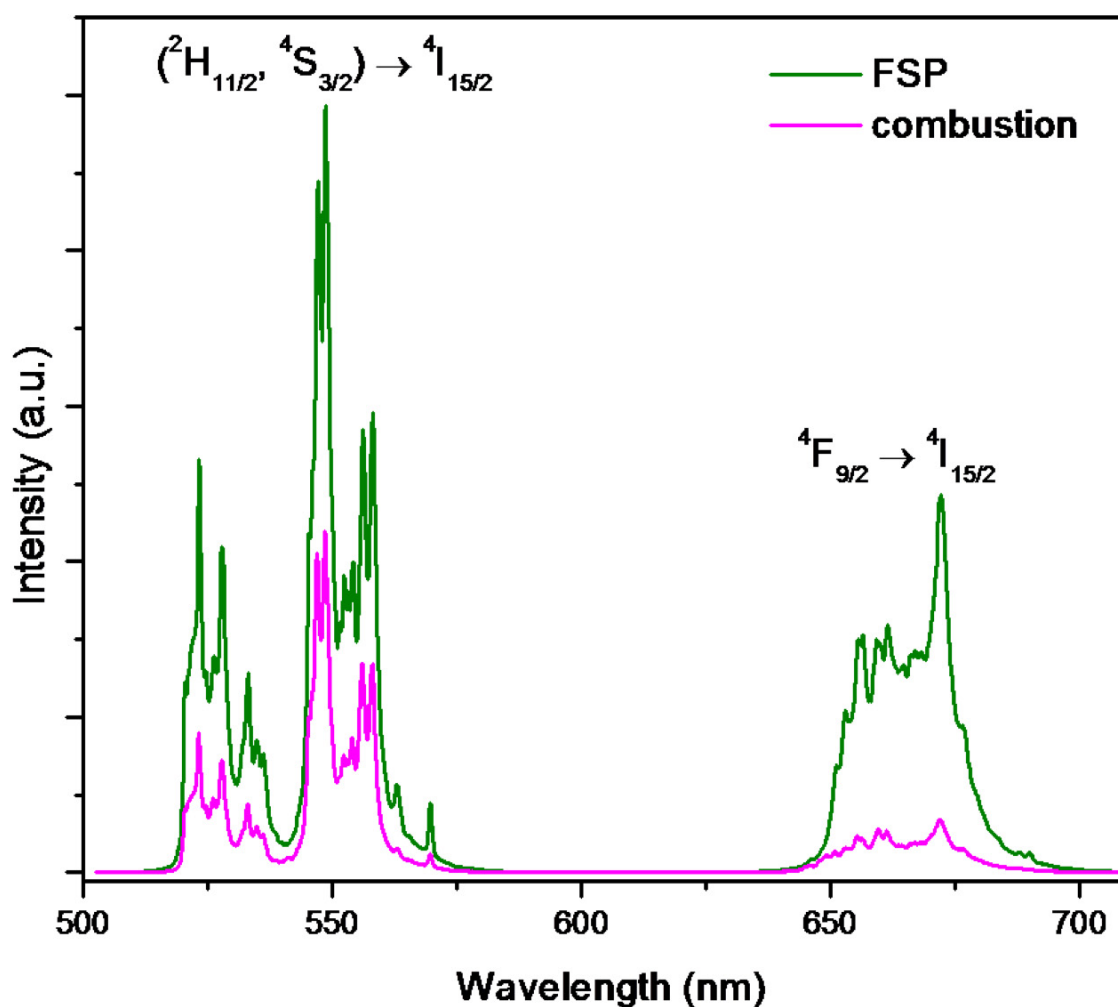


Figure 5.6: Room temperature luminescence of $Gd_2O_3:Er^{3+}$ prepared by propellant synthesis and FSP

The upconversion mechanisms at 980 nm are shown in Figure 5.7. Upconversion can occur via the ESA mechanism, where an Er^{3+} ion is promoted to an intermediate excited state, the $^4I_{11/2}$ level, from which a second incoming pump photon raises it to the $^4F_{7/2}$ level. After non-radiative decay to the lower lying $^2H_{11/2}$, $^4S_{3/2}$ and $^4F_{9/2}$ levels, the visible emission is observed. Since the ESA mechanism involves only the single ion, it is the prevalent mechanism in nanocrystals with low dopant concentrations.

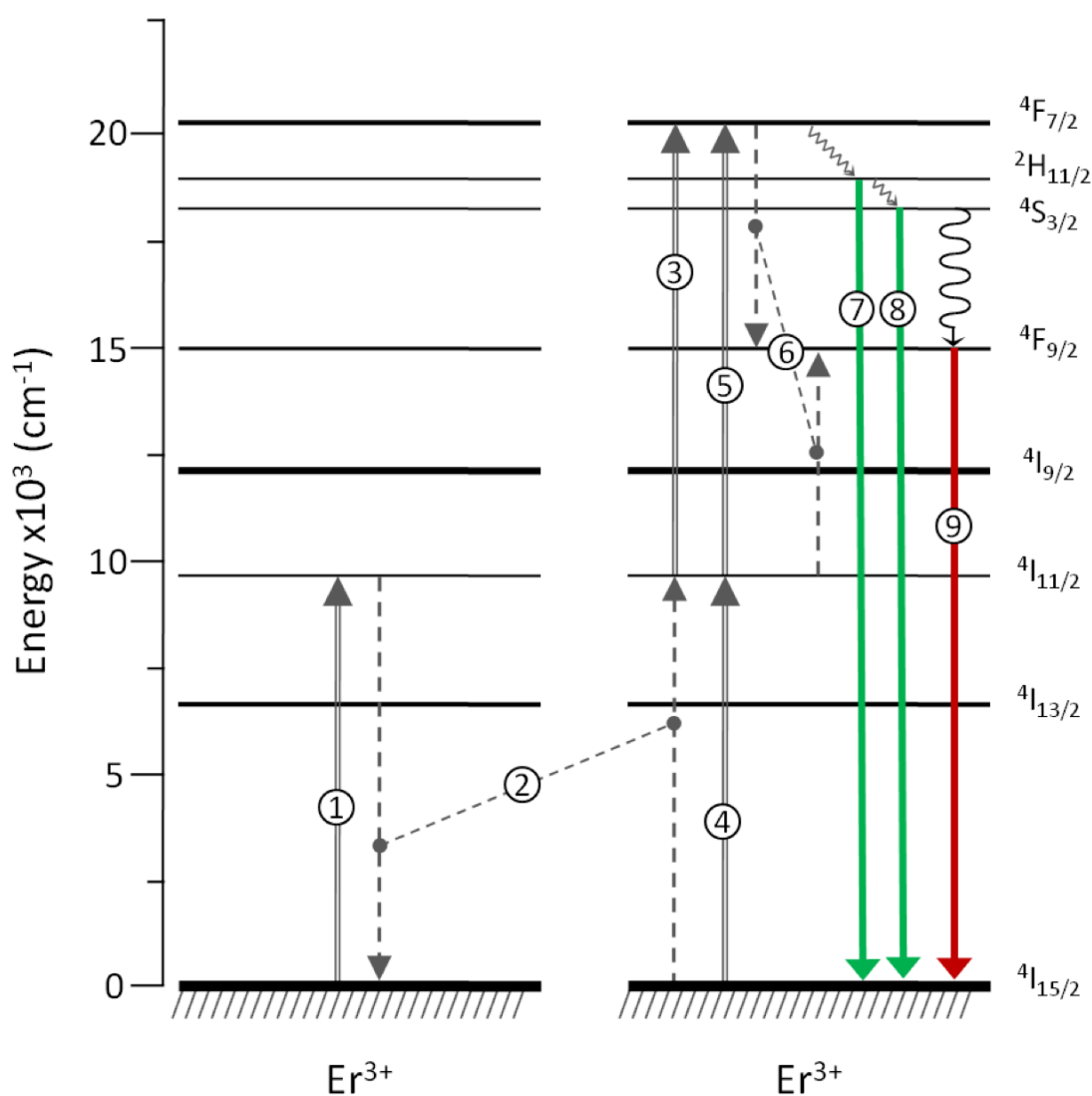


Figure 5.7: Upconversion mechanisms responsible for the green (7-8) and red (9) emission in Er^{3+} -doped Gd_2O_3 nanocrystals. – (1-2-3) energy transfer upconversion (ETU), (4-5) excited state absorption (ESA), and (6) cross relaxation [$^4F_{7/2}, ^4I_{11/2} \rightarrow ^4F_{9/2}, ^4F_{9/2}$] (CR).

Upconversion can also occur via the ETU mechanism, in which two ions in close proximity are both excited to the $^4I_{11/2}$ intermediate level. Acting as a donor, one of these two ions promotes, through energy transfer, a neighbouring Er^{3+} ion, firstly to its $^4I_{11/2}$ intermediate state, secondly to the $^4F_{7/2}$ excited state. Another mechanism is also possible, cross-relaxation (CR), where two neighbouring Er^{3+} ions are raised to the $^4I_{11/2}$ intermediate level. A cross-relaxation process will occur, bringing one ion to the $^4F_{7/2}$ level, subsequently resulting in the emission described above, while the other ion returns non-radiatively to the ground state. Since the last two mechanisms involve the interaction of neighbouring ions, the probability of ETU and CR occurring increases as the Er^{3+} concentration increases, due to the decreasing distance between Er^{3+} ions.

However, the compared samples in Figure 5.6 contain the same amount of Er^{3+} (1%) and this concentration is too low to affect significantly one transfer mechanism over the other. Since particle size and percentage of monoclinic phase are not different enough to affect the energy transfer mechanisms, the morphology (Figure 5.3) is probably the determinant reason influencing the intensity of the luminescence. In fact it has been reported that, for FED, samples with more homogeneous morphology show higher luminescence intensity compare to others with irregular morphology [93].

The samples, then, have been doped with various Er^{3+} concentrations, in order to study the differences in the luminescence emission. Normalized upconversion emission spectra acquired following 980 nm excitation for the $Gd_2O_3:Er^{3+}$ nanocrystals synthesized via propellant showed an enhancement of the red emission ($^4F_{9/2} \rightarrow ^4I_{15/2}$) with increasing dopant concentration (Figure 5.8).

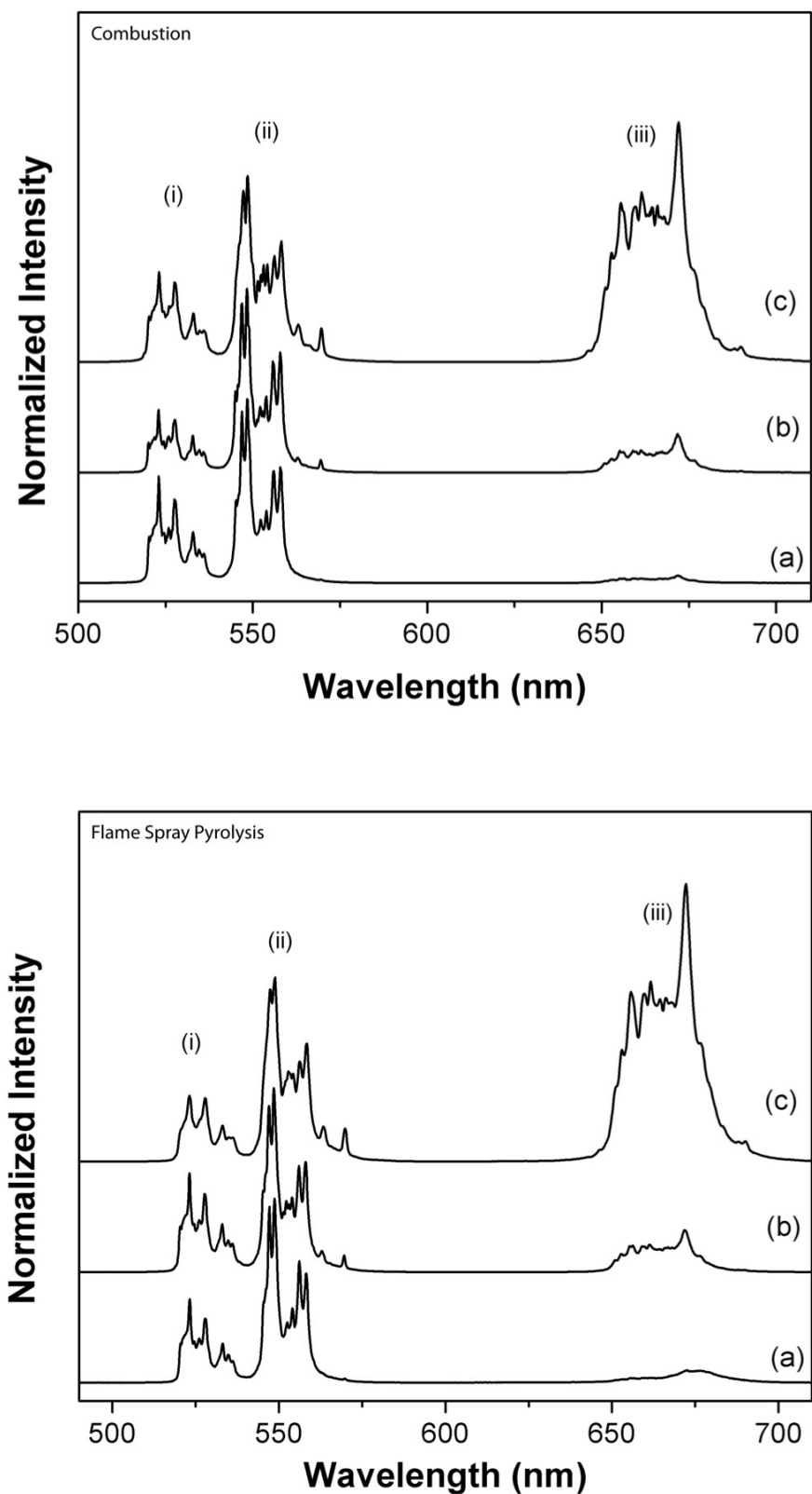


Figure 5.8: Room temperature upconversion spectra ($\lambda_{\text{exc}} = 980 \text{ nm}$) of $\text{Gd}_2\text{O}_3:\text{Er}^{3+}$ (a) 0.1 mol%, (b) 1 mol% and (c) 10 mol% prepared by propellant synthesis (top) or FSP (bottom) – (i) ${}^2\text{H}_{11/2} \rightarrow {}^4\text{I}_{15/2}$, (ii) ${}^4\text{S}_{3/2} \rightarrow {}^4\text{I}_{15/2}$ and (iii) ${}^4\text{F}_{9/2} \rightarrow {}^4\text{I}_{15/2}$.

Although the samples prepared by FSP showed a slightly larger increase in the red/green ratio for the samples doped with 1 and 10 mol% of Er^{3+} , the overall emission intensity are greater than the propellant ones for the three different concentrations.

The calculated red/green upconversion emission ratios were varied from 0.1 to 0.3-0.5 for the 0.1 and 1 mol% Er^{3+} -doped Gd_2O_3 nanocrystals prepared by both techniques (Table 5.2).

Er % conc. (mol %)	Ratio of the integrated intensity	
	Propellant synthesis	Flame Spray Pyrolysis
0.1	0.1	0.1
1	0.3	0.5
10	1.0	1.3

Table 5.2: The ratio of the integrated intensity of the ${}^4\text{F}_{9/2} \rightarrow {}^4\text{I}_{15/2}$ / (${}^2\text{H}_{11/2}$, ${}^4\text{S}_{3/2}$) $\rightarrow {}^4\text{I}_{15/2}$ emission bands after excitation using a wavelength of 980 nm

Increasing the Er^{3+} concentration (10 mol%), the red/green ratio increases to 1.0 for the sample prepared by propellant synthesis and 1.3 for the one prepared by FSP. In fact, increasing the concentration, and thus decreasing

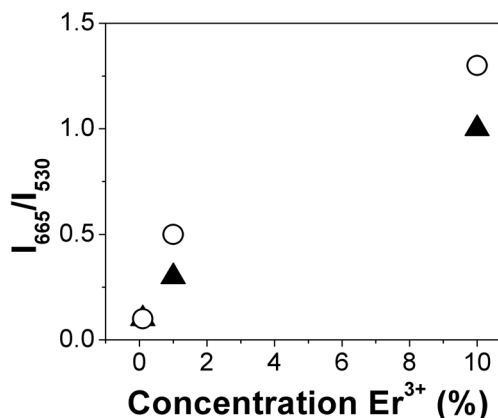


Figure 5.9: Plot of the ratio of the integrated intensity listed in Table 5.2 -▲ propellant synthesis, ○ FSP

distance between the neighbouring ions, favour cross-relaxation through the $[{}^4\text{F}_{7/2}, {}^4\text{I}_{11/2}] \rightarrow [{}^4\text{F}_{9/2}, {}^4\text{F}_{9/2}]$ mechanism, which is responsible for enhancement of the red emission, as previously reported in the literature [27,28]. Further population of the ${}^4\text{F}_{9/2}$ state may also occur through non-radiative decay from higher lying levels.

Comparing the two syntheses, the overall shape of the emission spectra does not change (Figure 5.8). However, the absolute upconverted emission intensity of the samples prepared by FSP is twice that of the nanocrystals prepared by propellant synthesis. In fact, the temperature involved during the synthesis affects the emission intensity of the nanocrystals [124]. The samples prepared by the propellant technique required a further thermal treatment at 500 °C for 2 h after preparation to eliminate the residual unburnt species; therefore, the nanocrystals synthesized by FSP were also treated at the same conditions for comparative reasons. However, this step does not affect the intensity of the luminescence emission in the samples prepared by FSP and it is not usually required in this method, since the high temperature developed during the synthesis is already sufficient to decompose the precursors and produce nanocrystals, eliminating the need for any further post-synthesis heat treatment.

5.2 Development of Flame Spray Pyrolysis

In order to achieve a better understanding of the Flame Spray Pyrolysis, Gd_2O_3 has been chosen as a probe to study how the variation of the operating parameters of the system affects the properties of the material, such as luminescence, particle size, phase purity and crystal structure. This study is of interest, in our view, because if the effect of each parameter on the final products is known, it is possible to tailor the properties of the produced compounds and plan them in advance. With the objective to focus only on the effects of the synthetic parameters, the Gd_2O_3 nanocrystals have been doped with only Er^{3+} .

For reference purposes, Figure 5.10 is reported below.

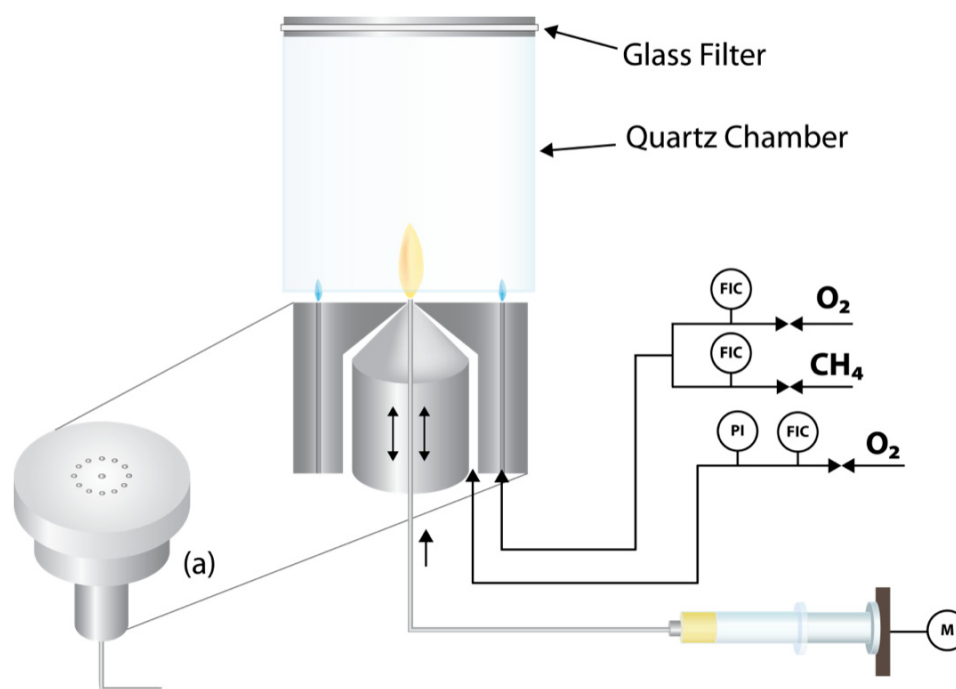


Figure 5.10: Setup of Flame Spray Pyrolysis

5.2.1 Synthetic parameters

The parts of the synthesis that can be varied are the following:

- a. Type of metal precursor
- b. Type of solvent/fuel
- c. Central flame oxygen flow rate
- d. Precursor solution flow rate
- e. Aperture of the nozzle

While a and b affect the synthesis from a strict chemical point of view, c, d and e influence the flow dynamics of the system and, as a consequence, the flame. In particular, the variation of the oxygen rate, of the fuel rate or of the opening of the nozzle affects the heat of combustion, the dispersion of the precursors in the flame and, finally, the length of the flame (Figure 5.11). Ultimately, these variations have an effect on the formation of the products in the flame and, as a consequence, of their properties. In order to understand how these settings affect the properties of the luminescent nanomaterials, each of the synthesis settings has been studied.

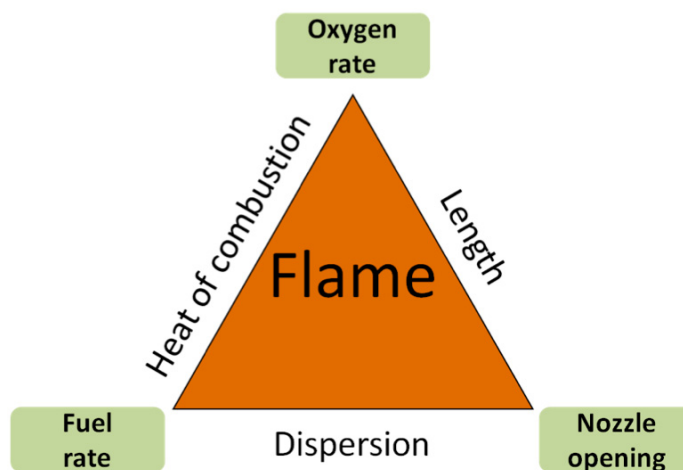


Figure 5.11: Variable synthesis settings and their effect on the flame.

5.2.2 Shape of the flame and mechanism of formation

The variation of the synthesis settings affects visibly the flame. As it can be seen in Figure 5.12, when the fuel flow rate is increased from 1 mL/min to 3 mL/min, the flame becomes longer, from 13 cm to 19 cm. In fact, a faster fuel flow rate provides more solution in the unity of time and the flame, as a consequence, is fed by more fuel.

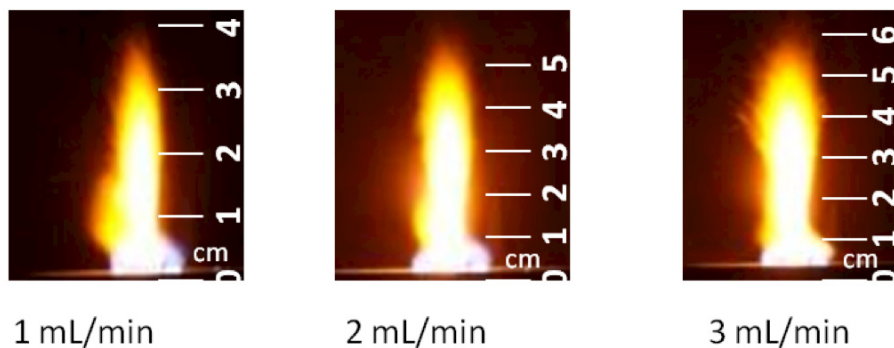


Figure 5.12: Effect of the fuel flow rate on the flame.

Similarly, when the oxygen flow rate is decreased from 3 L/min to 1 L/min, the flame becomes longer, from 9 cm to 18 cm (Figure 5.13). In fact, a higher oxygen rate increases the dispersion of the precursors when they enter the flame, decreasing also the collisions between the particles in the flame and, as a consequence, quenching the flame temperature.

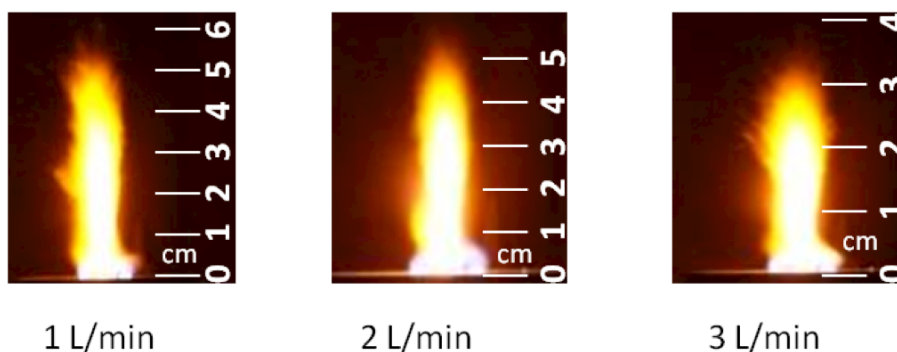


Figure 5.13: Effect of the oxygen flow rate on the flame.

Finally, when the nozzle is closed, and the pressure drop at the exit increases from 0 atm to 4 atm, the flame shortens from 20 cm to 9 cm (Figure 5.14). In fact, the velocity of the gas (O_2) inside the flame determines the residence time of the particles in the flame.

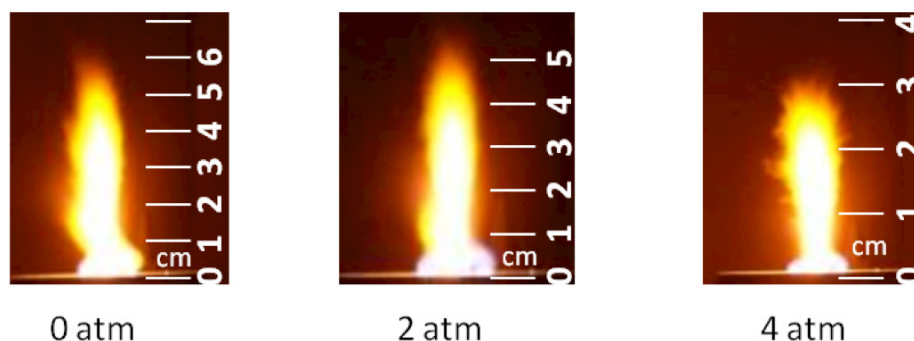


Figure 5.14: Effect of the opening of the nozzle on the flame.

The shape of the flame has an important impact on the properties of the final products. In fact, the mechanism of formation of the nanoparticles occurs entirely within the flame. As it can be seen in Figure 5.15, the length of the flame determines the time spent for the formation of the nanoparticles.

As the drop of precursor solution leaves the tip of the capillary tube, the solvent evaporates and burns and, as it enters, onto the hot part of the flame, the metal precursor is released and decomposed. After this, the nucleation occurs, followed by coalescence and condensation and, if the particles remain in the flame for a sufficient period of time, they can agglomerate [74].

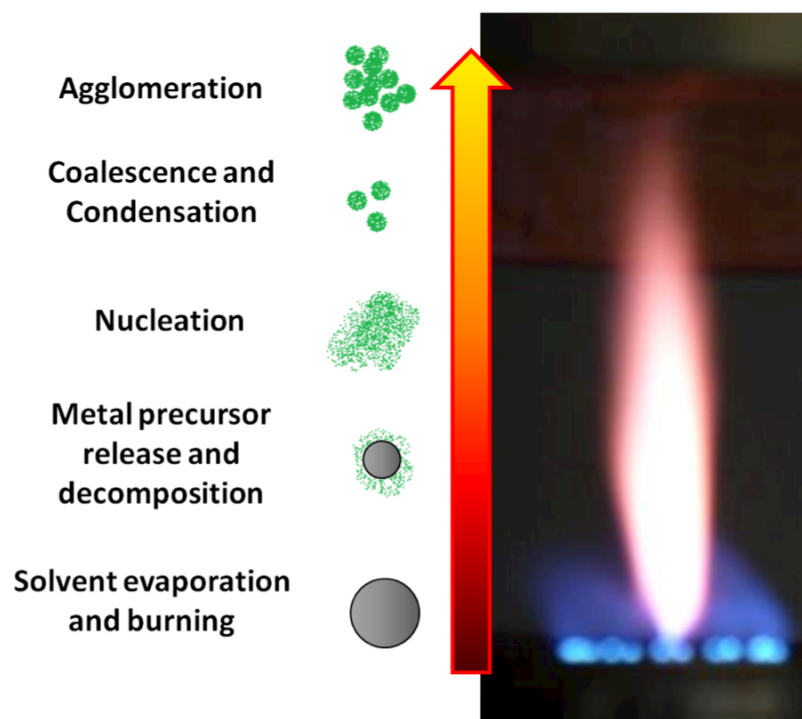


Figure 5.15: Formation of particles along the length of the flame

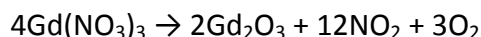
Hence, it is clear that the extension of the time period during which the particles stay in the flame will cause their size to increase and the aggregation processes will become more probable. On the other hand, a short flame will cause the formation of small particles. In any case, the time spent into the flame needs to be sufficient to allow the decomposition of the precursors and the formation of the desired phase of the product. Usually, the most favourable results are achieved when a compromise between these factors is sought.

5.2.3 Choice of metal precursor

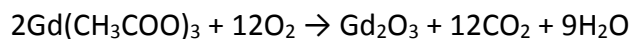
The choice of the metal precursor depends mainly on its solubility in the solvent used. In fact, the precursor solution needs to be limpid and stable, in order to not clog the capillary tube and maintain the continuity of the synthesis.

In this work, metal nitrates and acetates have been chosen as precursors.

Initially, metal nitrates have been used as precursors. However, the resulting products showed low purity phase, as, in fact, it has already been reported in literature [112]. However, nitrates have been chosen when ethanol was used as solvent for the preparation of core-shell nanoparticles. In general, ethanol is not a good solvent for flame spray pyrolysis because it evaporates too quickly when it exits the capillary tube and it creates lumps, which clog the needle. However, the endothermic decomposition of nitrates compensates the high volatility of ethanol.



Metal acetates are the main precursors used, because they dissolve well in the various chosen solvents and they lead to stable products, with high thermal stability, due to the high temperature that is developed during their exothermic decomposition:



5.2.4 Choice of solvent/fuel

In order to optimize the FSP settings and obtain the best conditions during the injection of the precursor solution, several solvents have been chosen (Table 5.3).

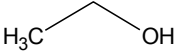
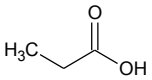
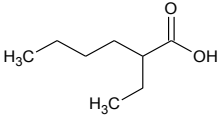
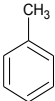
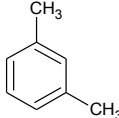
solvent	formula	bp (°C)	ΔH_{cv} (kJ/L)
Ethanol		78	-23.5
Propionic acid		141	-20.6
2-Ethylhexanoic acid		228	-30.1
Toluene		110	-36.8
Xylene		138	-36.9

Table 5.3: Solvents used for the preparation of the precursor solutions and their characteristics.

Considering that ethanol is used for the preparation of several luminescent nanoparticles [62,69,125], it has been the first solvent employed. However, as mentioned in the previous paragraph, EtOH is too volatile (bp: 78°C) and the drops evaporate too quickly to allow the precursor to decompose in a sufficient time. As a consequence, lumps are formed at the tip of the nozzle, which is clogged. In addition to this, it is difficult to collect the prepared powder sample.

With the purpose to overcome the clogging of the nozzle, propionic acid has been chosen as a solvent, because it has a ΔH_{cv} similar to EtOH, but higher boiling point (141 °C). However, the products presented a brownish color, which is not desirable for luminescence purposes, considering that dark coloured samples would absorb the excitation light to the disadvantage of the emitted light. Most likely, propionic acid does not provide, during its combustion, the conditions necessary to produce the material wanted. As a consequence, some unburnt residues are still present on the products. In fact, the powders have been treated at 500°C for 2 h and they turned white, showing bright luminescence. However, the main reason why FSP has been chosen is the possibility of preparing the samples in one step and, as a consequence, propionic acid has been discarded as a possible solvent.

It is known that solvents with longer chains provide a better combustion [75]. In particular, the presence of branching improves the combustion efficiency, as it occurs with the octane number for gasoline. Therefore, it has been chosen 2-ethyl-hexanoic acid (2EHA) as solvent. The prepared samples were white and they did not require any further treatment. Moreover, they showed bright luminescence, as they were synthesized. As a consequence, 2EHA was selected as solvent to prepare all the samples used to study the effect of the synthesis parameters (oxygen flow rate, fuel flow rate, nozzle opening) on the luminescent nanocrystals.

However, the samples prepared with 2EHA showed high composition of cubic phase (min 18%) and, because of their low grade of purity, are not suitable for high performance optical purposes. Therefore, solvents with higher ΔH_{cv} have been chosen, in order to provide higher temperature during the synthesis and prepare samples with higher phase purity.

For this purpose, toluene and xylene, were selected as solvents. However, they could not be used as pure solvents, because the dissolution of the acetates precursors is difficult and the solutions are unstable. In fact, they become cloudy during the injection, forcing the interruption of the reaction. To overcome this issue, mixtures of xylene and toluene with 2EHA have been prepared. The solubility of the precursors and the stability of the solution improved dramatically. Due to the higher volumetric combustion enthalpy of these solutions, the temperature in the flame was higher than with the other solvents and the obtained products showed higher purity. In general, when the molar concentration of xylene, or toluene, in 2EHA is increased, the volumetric combustion enthalpy increases and the equivalence ratio decreases, leading to reactions at higher temperatures and more fuel rich (Table 5.4).

The XRPD patterns (Figure 5.16) showed reflections typical of the monoclinic phase of Gd_2O_3 (JCPDS no. 160226), with a component of cubic phase (ICSD 41270). As the molar fraction of xylene increases, the monoclinic component increases and the sharper lines of the XRPD patterns indicate a better crystallinity.

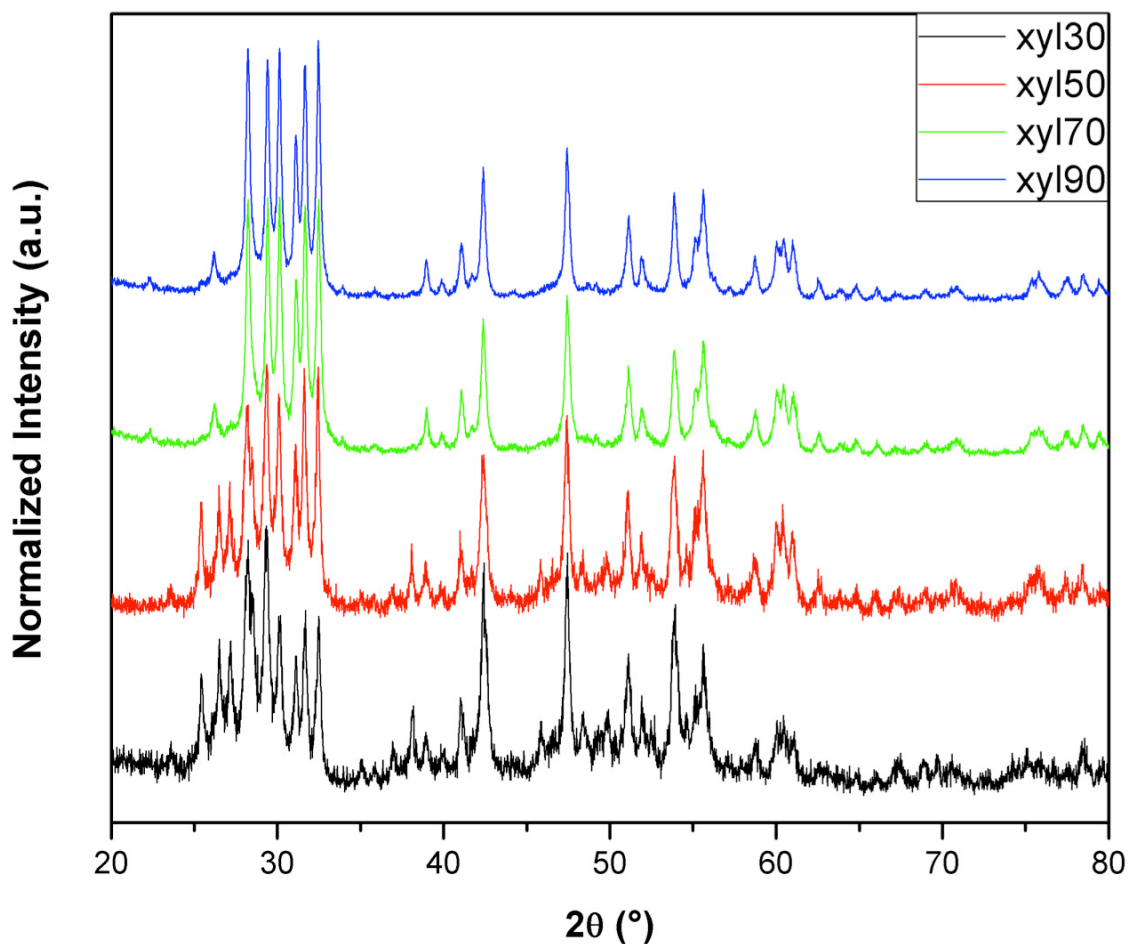


Figure 5.16: XRPD patterns of the samples prepared with different molar compositions of xylene (xyl) in 2EHA. Xyl# indicates the molar fraction of xylene in a xylene/2EHA solution.

% xylene in 2EHA	Φ	ΔH_{cv} KJ/L _{O2}	% monoclinic phase
30	0.266	-32.10	76
50	0.254	-33.46	81
70	0.242	-34.83	89
90	0.230	-36.19	93

Table 5.4: solutions of xylene in 2EHA.

5.2.5 Effect of the precursors solution flow rate

In order to study the effect of the precursors flow rate, a series of samples have been prepared, keeping the oxygen flow rate constant and obtaining synthetic conditions with volumetric combustion enthalpies of -15, -20, -30, -40, -45 KJ/L (Table 5.5). The oxygen flow rate was kept constant at 2 L/min and the pressure drop at 2 atm.

ΔH_{cv} KJ/L _{O2}	Fuel flow rate mL/min
-15	1.00
-20	1.33
-30	2.00
-40	2.66
-45	3.00

Table 5.5: Series of samples prepared to study the effect of the solution flow rate on the final properties of the nanoparticles. Oxygen flow rate is kept at 2L/min and the pressure drop at 2 atm.

For all the samples, the luminescence emission spectra, after excitation at 980 nm, have been collected at room temperature. As showed in Figure 5.17, the observed emissions are in the green and in the red region of the spectrum.

As this series of samples is doped with only Er³⁺, it can be considered that the UC mechanism is the same as the one reported in Figure 5.7, and previously described. In brief, the excitation at 980 nm populates, via different multiphoton energy transfer mechanisms (ETU, ESA, CR), the ⁴I_{11/2} level. From here, after non-radiative decay, the lower levels, ²H_{11/2}, ⁴S_{3/2} and ⁴F_{15/2}, are populated and their relaxation to the ground state, ⁴I_{11/2}, generates the observed green and red emissions.

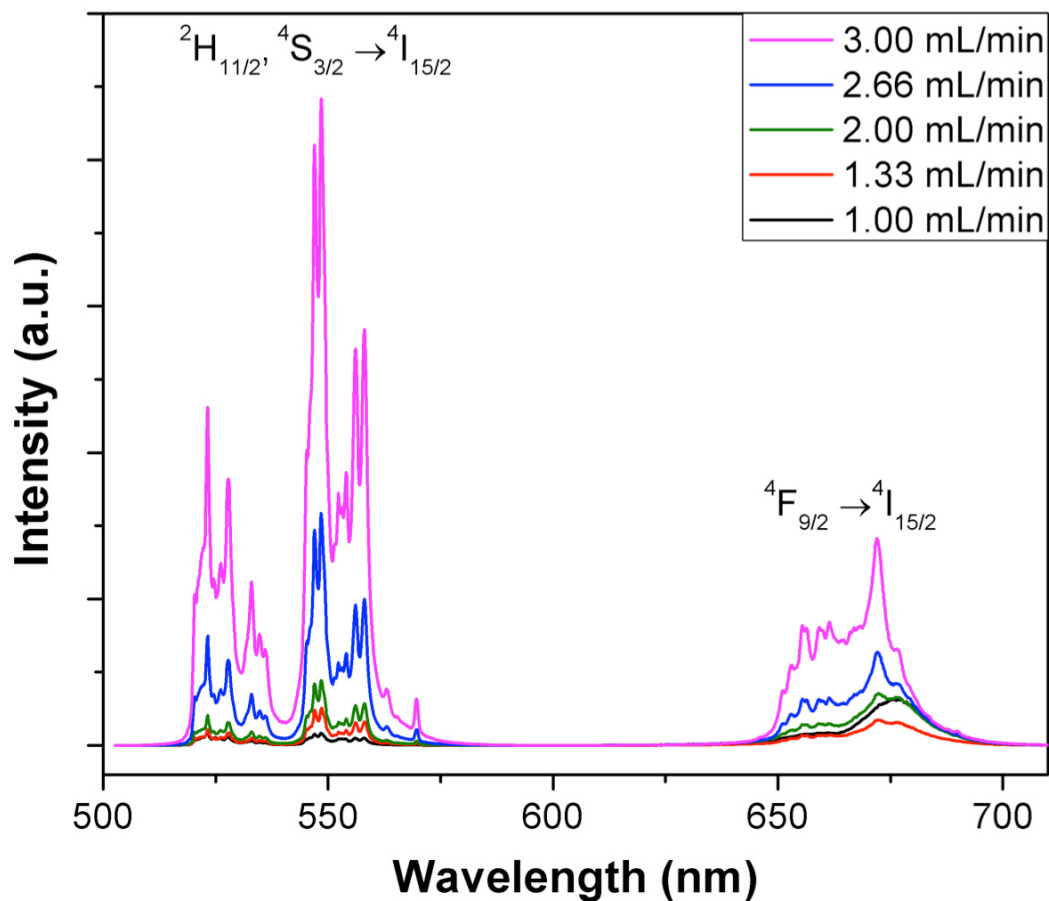


Figure 5.17: UC spectra of $\text{Gd}_2\text{O}_3:1\%\text{Er}^{3+}$ samples at different precursor solution flow rates. $\lambda_{\text{exc}} = 980 \text{ nm}$.

As it can be seen in Figure 5.17, the overall UC luminescence intensity increases, when the precursor solution flow rate increases. The curves of the sample prepared at the lowest flow rate have not a defined structure. In fact, the volumetric combustion enthalpy of the sample prepared at 1 mL/min is the lowest and probably, in these conditions, the crystallinity of the sample is too low to show structured features in the UC emission spectrum. For all the other samples, major differences in the shape of the spectra are not observed, but the ratio between the green and red emissions varies significantly with the variation of the fuel flow rate (Figure 5.18).

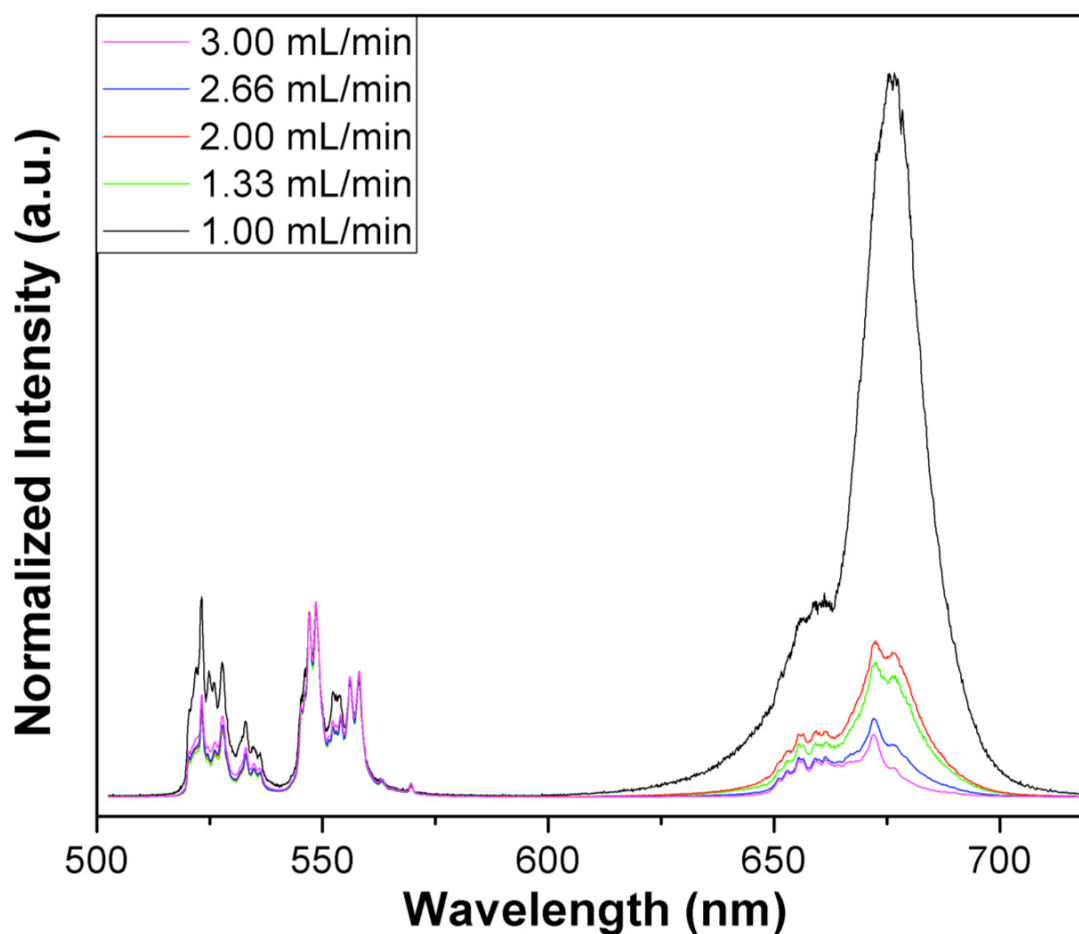
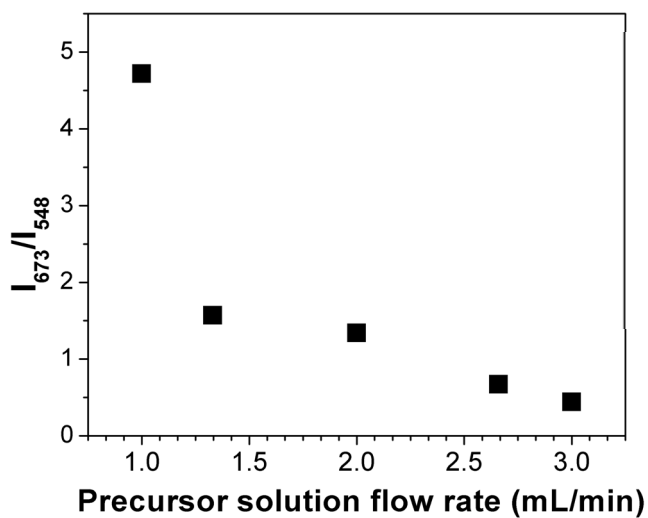


Figure 5.18: UC emission spectra, normalized to ${}^4S_{3/2}$, at different precursor solution flow rates. $\lambda_{\text{exc}} = 980$ nm



flow <i>mL/min</i>	Red/green ratio	ΔH_{cv} <i>KJ/L_{O2}</i>
1.00	4.72	-15
1.33	1.57	-20
2.00	1.34	-30
2.66	0.67	-40
3.00	0.44	-45

Table 5.6: red/green ratio of the samples prepared at different liquid flow rates

Figure 5.19: Intensity ratios between the red emission (${}^4F_{9/2}$, centered at 673 nm) and the green emissions (${}^2H_{11/2}$, ${}^4S_{3/2}$, centered at 548 nm)

The sample prepared at 1 mL/min shows again different features in the spectral lines. In particular, the emission from the $^2H_{11/2}$ level is higher than for the other samples. This level is hypersensitive to the crystal environment and the difference with the other samples confirms the presence of more defects in the Er^{3+} site and the low crystallinity of the sample prepared at 1 mL/min. In fact, the thermodynamics conditions of the synthesis (lowest volumetric combustion enthalpy of the series) support this hypothesis.

In order to calculate the ratios, the intensities of the green and red emissions have been integrated and the ratios between the red emission ($^4F_{9/2}$, centered at around 673 nm) and the green emissions ($^2H_{11/2}$, $^4S_{3/2}$, centered at around 548 nm) have been reported in Table 5.6: red/green ratio of the samples prepared at different liquid flow rates

As the precursor solution increases, the ratios between the red and the green emission decrease (Figure 5.19). The sample with the lowest volumetric combustion enthalpy, -15 kJ/L, prepared at 1 mL/min, shows a prevalent emission in the red, with a ratio red/green is around 5:1. This ratio drops almost three times (1:1.34) when the solution flow rate is increased at 2 mL/min, and it drops more than ten times for the sample at the highest volumetric combustion enthalpy, -45 kJ/L, prepared at 5 mL/min. This last sample showed a prevalent emission in the green, visible with the naked eye.

When the precursor solution flow rate increases, the volumetric combustion enthalpy increases and the temperature involved in the reaction is expected to increase as well.

A higher temperature during the formation of the nanocrystals makes the combustion more efficient and decreases the probability of unburnt species on the surface of the samples. In fact, the weight loss of the samples decreases as the precursor solution flow rate increases (Figure 5.20). While the sample prepared at 3 mL/min, with the highest volumetric combustion enthalpy, shows a weight loss of about 4.5%, the sample prepared at 1 mL/min, with the lowest volumetric combustion enthalpy of the series, presents a weight loss of almost 7%. The DTA measurements (Figure 5.20) showed mainly three peaks, which, in literature, have been identified as the decomposition of water (100°C) and carbonaceous species that are eliminated, between 200 and 300°C, by evolution of CO₂ [75].

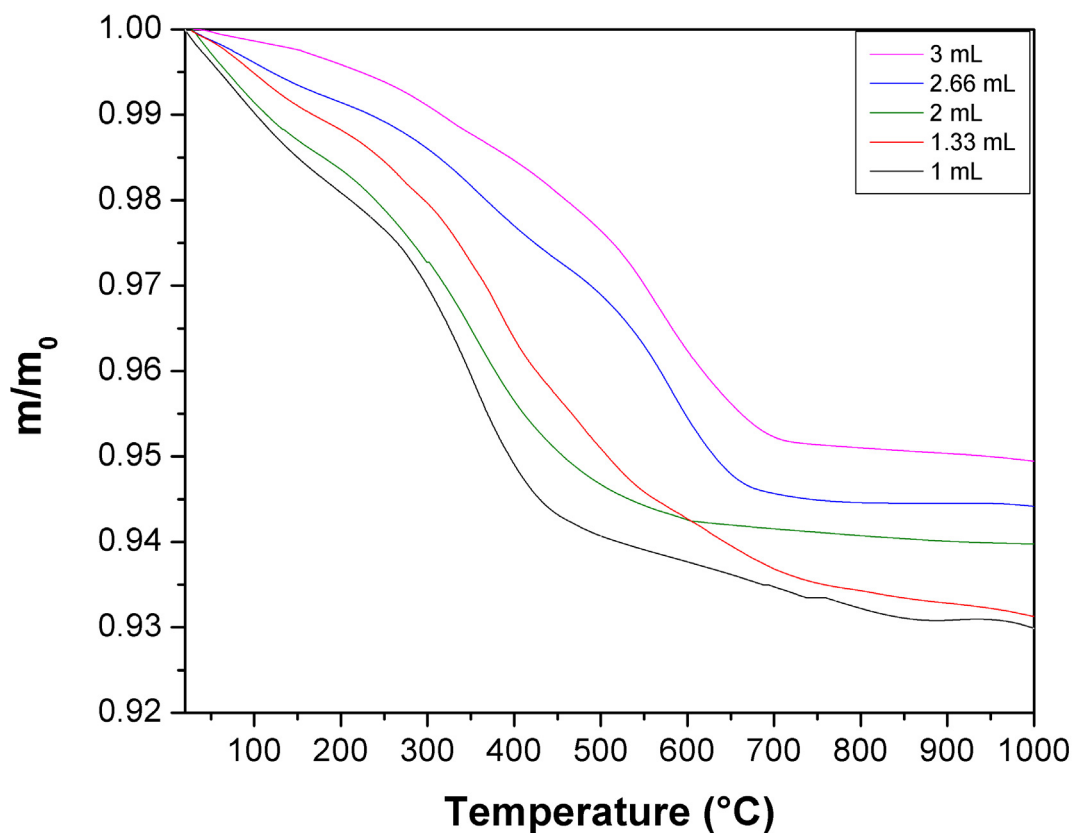


Figure 5.20: TGA measurements of Gd₂O₃:1%Er³⁺ samples at different precursor solution flow rates.

The increasing temperature developed during the synthesis, when the volumetric combustion enthalpy is increased, provides a better decomposition of the metal precursors and of the organic solvent. As a consequence, on the surface of the nanocrystals, a lower amount of hydroxylic groups, from water, and carbonates, from carbonaceous unburnt species, are present. These species have a quenching effect on the luminescence emission, because their vibrational energy (1500 cm^{-1} and 3350 cm^{-1}) can fill the gap between the ${}^4F_{7/2}$ and the ${}^2H_{11/2}$ energy states and they can increase the probability of populating of the ${}^4F_{9/2}$, via cross-relaxation, and decrease the probability of populating the ${}^2H_{11/2}$ and ${}^4S_{3/2}$ levels. The consequence of the presence of these species is a quenching of the overall luminescence, because the available photons do not pump efficiently the higher energy levels (${}^2H_{11/2}$ and ${}^4S_{3/2}$), and an increase in the red emission, because of the increased population of the ${}^4F_{9/2}$ level.

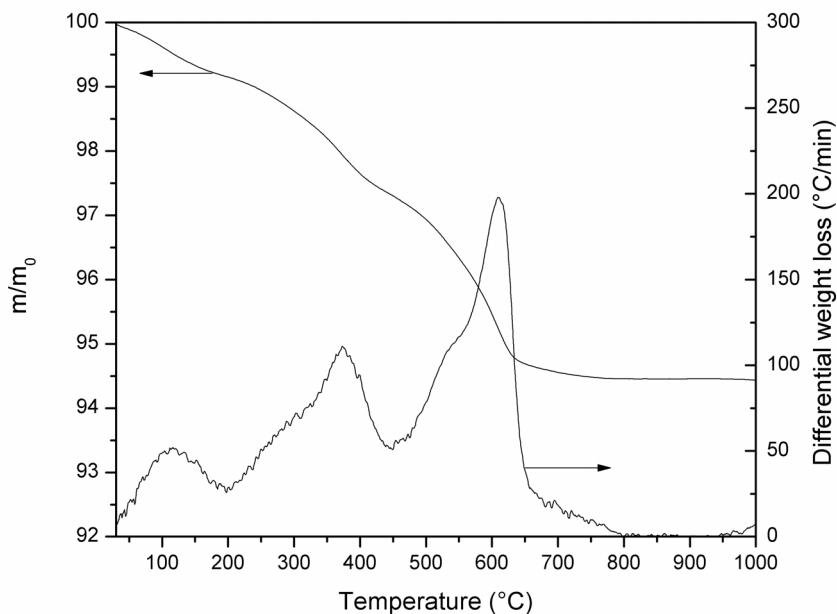


Figure 5.21: DTA and TGA of $\text{Gd}_2\text{O}_3:1\%\text{Er}^{3+}$ sample prepared at 2.66 mL/min.

Therefore, at the increase of the volumetric combustion enthalpy, and of the temperature developed during the reaction, the residues from unburnt carbonaceous species decreases. As a consequence, the overall emission intensity increases, as well as the red/green intensity, because of a higher probability to populate the $^4F_{9/2}$ level with a $[^4F_{7/2}, ^4I_{11/2}] \rightarrow [^4F_{9/2}, ^4F_{9/2}]$ cross-relaxation mechanism.

The temperature developed during the synthesis affects also the thermal stability of the samples (Figure 5.20). While all the other samples stabilized at about 700°C, the sample at 1mL/min becomes stable only above 780°C, confirming the incomplete combustion in the flame and a higher concentration of unburnt residues on the surface of the nanocrystals.

The rate of combustion affects also the phase purity of the samples. The XRPD patterns (Table 5.7) showed reflections typical of the monoclinic phase of Gd_2O_3 (JCPDS no. 160226), with a component of cubic phase (ICSD 41270), which varied with the precursor solution fuel flow rate (Table 5.7).

At the lowest rate, 1 mL/min, the amount of monoclinic phase is 93% and it decreases dramatically to 64%, as the precursors solution flow rate is increased at 3 mL/min, with the highest volumetric combustion enthalpy, -45 KJ/L.

The variation of the phase purity with different settings in samples prepared by flame spray pyrolysis has been reported for $Y_2O_3:Eu^{3+}$ [56]. In the reported case, it was possible to tune the phase purity of the samples (cubic or monoclinic) modifying the synthetic parameters.

In the samples prepared in this thesis, it has not been possible to produce a completely cubic or monoclinic Gd_2O_3 , because the limits used for the study of the parameters (1 mL/min and 3 mL/min in the case of the precursor solution flow rate) are imposed by the geometry of the employed nozzle: at settings lower or higher than the limits, it would not be possible to obtain a stable flame.

In the samples prepared in this work, when the precursor solution flow rates increase, and the volumetric combustion enthalpy increases, the percentage of monoclinic phase decreases. The monoclinic phase has a lower symmetry than the cubic phase. Therefore, an increase in the amount of monoclinic phase would suggest an enhancement of the intensity of the luminescence emission, because of the release of otherwise forbidden transitions.

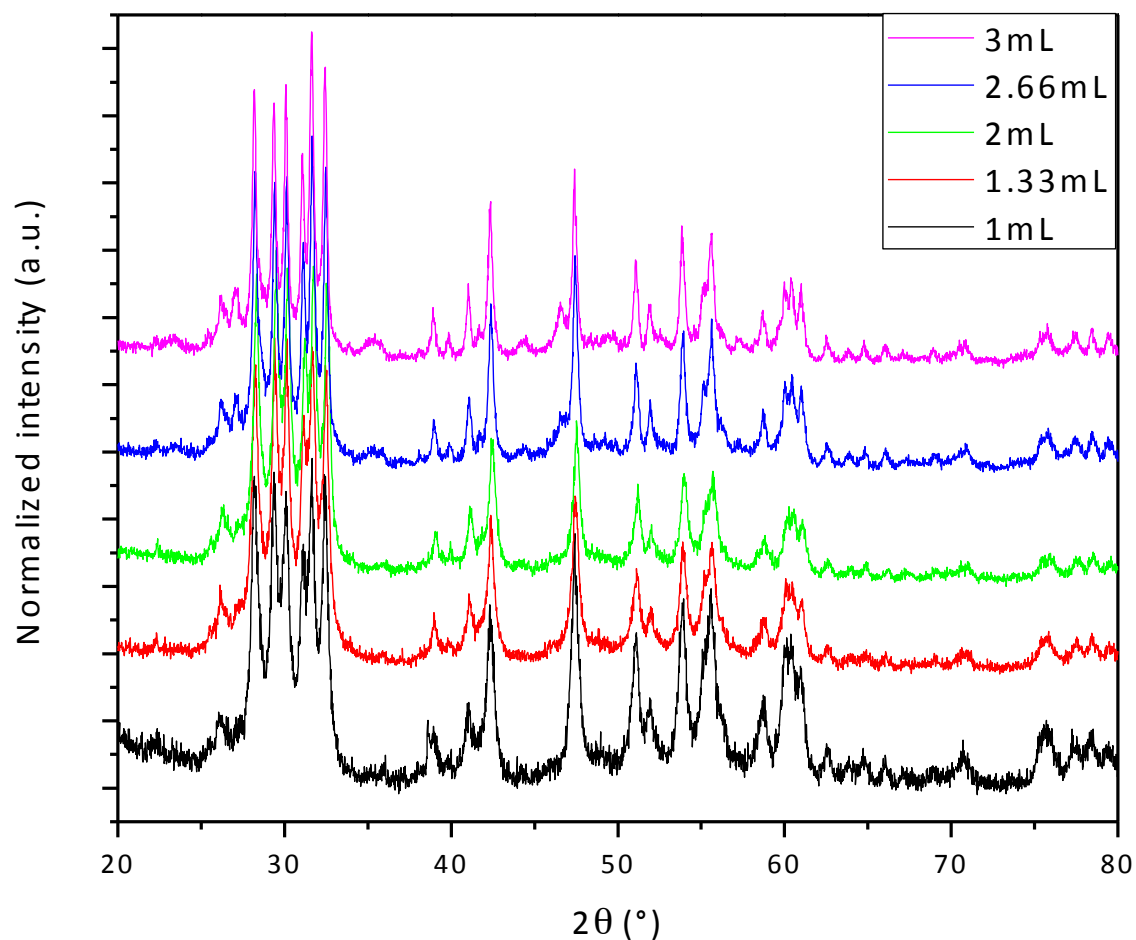


Figure 5.22: XRPD patterns of the samples prepared at different precursor flow rates.

flow <i>mL/min</i>	ΔH_{cv} <i>KJ/L_{O2}</i>	% monoclinic	d <i>nm</i>
1.00	-15	93	12
1.33	-20	89	13
2.00	-30	88	14
2.66	-40	80	20
3.00	-45	64	23

Table 5.7: Summary of the samples prepared at various precursor flow rates, showing the volumetric combustion enthalpy, the % of monoclinic phase and the size of the particles.

However, it has been observed that, increasing the solution flow rate, while the monoclinic phase decreases, the intensity of the luminescence emission increases (Figure 5.18), which is in contrast with the behaviour expected theoretically. As it can be observed in , in the cubic phase, the Er^{3+} ions could be allocated in two sites: one with symmetry C_2 and one with C_i , which is optically inactive due to presence of the inversion center. In the monoclinic phase, the ions could be allocated in three C_s sites, all of them optically active.

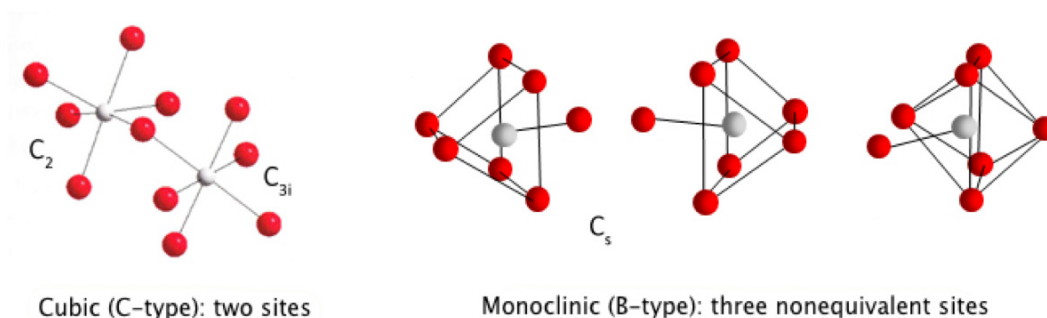


Figure 5.23: Cubic and Monoclinic phase of Gd_2O_3 .

Therefore, looking at the geometry, in the cubic phase only the 50% of the ions contributes to the UC emission, while in the monoclinic phase all the ions take part to the UC mechanisms. This means that, in addition to the symmetry decrease, samples with a higher monoclinic component are statistically supposed to contribute more efficiently to the luminescence emission, resulting in an increase in the intensity.

Ideally, in order to better understand the trend of the prepared samples, a sample with a cubic component higher than 90% should have been prepared. This would have allowed the comparison between the two extremes of the series. However, the apparatus limitations do not allow us to increase the fuel flow rate further.

With the objective to obtain a more complete picture of the observed trend, the particle size of the samples has been calculated by the Scherrer equation. As it can be seen in Table 5.7, when the liquid flow rate is increased, the particle size increases from 12 nm, at 1 mL/min, to 23 nm, at 3 mL/min. It is known that the luminescence intensity is dependent from the particle size. Therefore, it can be concluded that, in this series of samples, the increase of the emission intensity is mainly due to the increase of the particle size (Figure 5.24).

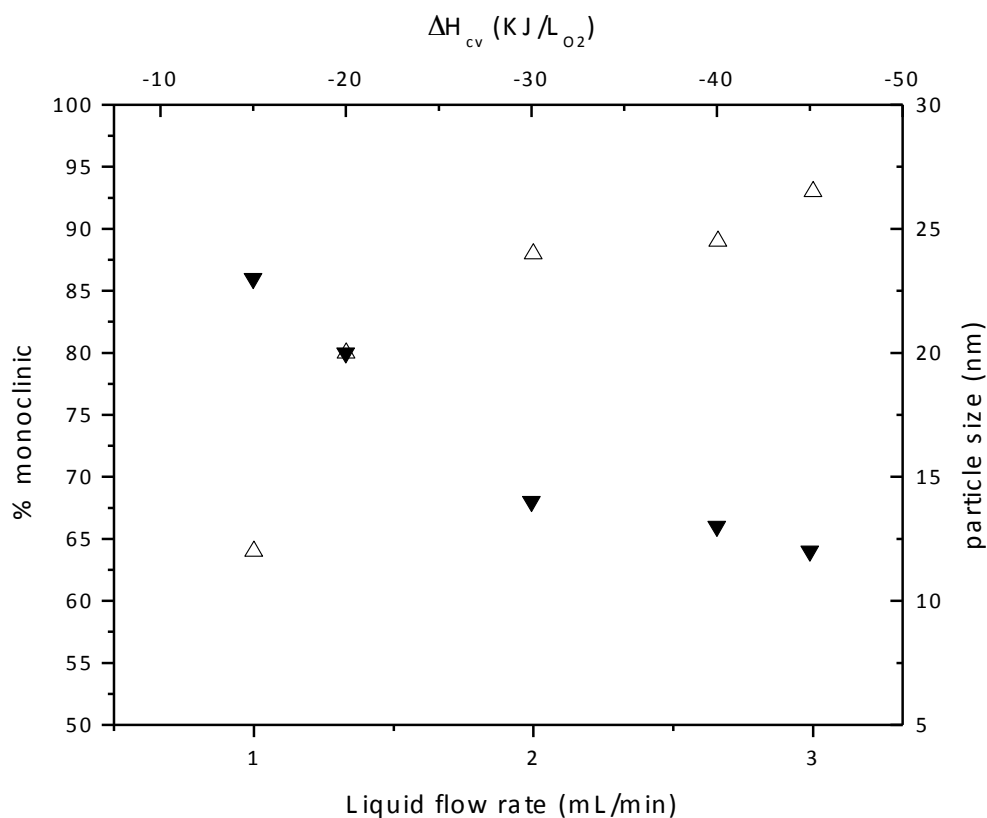


Figure 5.24: Plot showing the trend of the liquid flow rate and the volumetric combustion enthalpy respect to the % of monoclinic phase (▼) in the products and the particle size (△).

The particle size observed with TEM images is in agreement with the values calculated with the Scherrer equation. Moreover, the TEM images showed an increase in the agglomeration of the nanocrystals as the solution flow rate was increased (Figure 5.25).

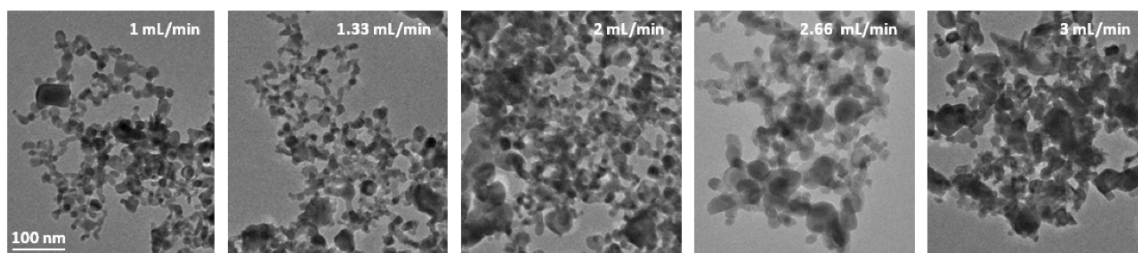


Figure 5.25: TEM images of $\text{Gd}_2\text{O}_3:1\%\text{Er}^{3+}$ samples prepared at different precursor solution flow rates

In fact, at the increase of the solution flow rate, the volumetric combustion enthalpy increases and, as a consequence, the temperature developed during the synthesis is expected to increase as well. Moreover, when the liquid flow rate increases, the flame becomes longer (Figure 5.12) and the particles spend more time in the flame, increasing the agglomeration time. As a consequence, it is plausible to observe a larger size of the nanocrystals.

5.2.6 Effect of the oxygen flow rate.

The precursor solution rate has been kept constant in the series of samples prepared to study the effects of the oxygen flow rate on the nanocrystals (Table 5.8). As for the previous section, synthetic conditions with volumetric combustion enthalpies of -15, -20, -30, -40, -45 KJ/L have been used. The precursors solution flow rate has been maintained at 2 mL/min and the pressure drop at 2 atm.

ΔH_{cv} KJ/L _{O2}	Oxygen flow rate L/min
-15	4.00
-20	3.00
-30	2.00
-40	1.50
-45	1.33

Table 5.8: Series of samples prepared to study the effect of the oxygen flow rate on the final properties of the nanocrystals. Precursor solution flow rate is kept at 2 mL/min and the pressure drop at 2 atm.

After excitation at 980 nm at room temperature, all the samples showed emission in the green ($^2H_{11/2}, ^4S_{3/2} \rightarrow ^4I_{15/2}$) and in the red ($^4F_{15/2} \rightarrow ^4I_{15/2}$), similarly to what observed for the previous series of samples (Figure 5.26)

Figure 5.26 shows that the overall UC luminescence intensity increases, when the oxygen flow rate decreases. There are not remarkable differences in the overall shape of the spectra, but the ratio between the green and red emissions, when the oxygen flow rate increase, undergoes a significant variation (Table 5.9 and Figure 5.27).

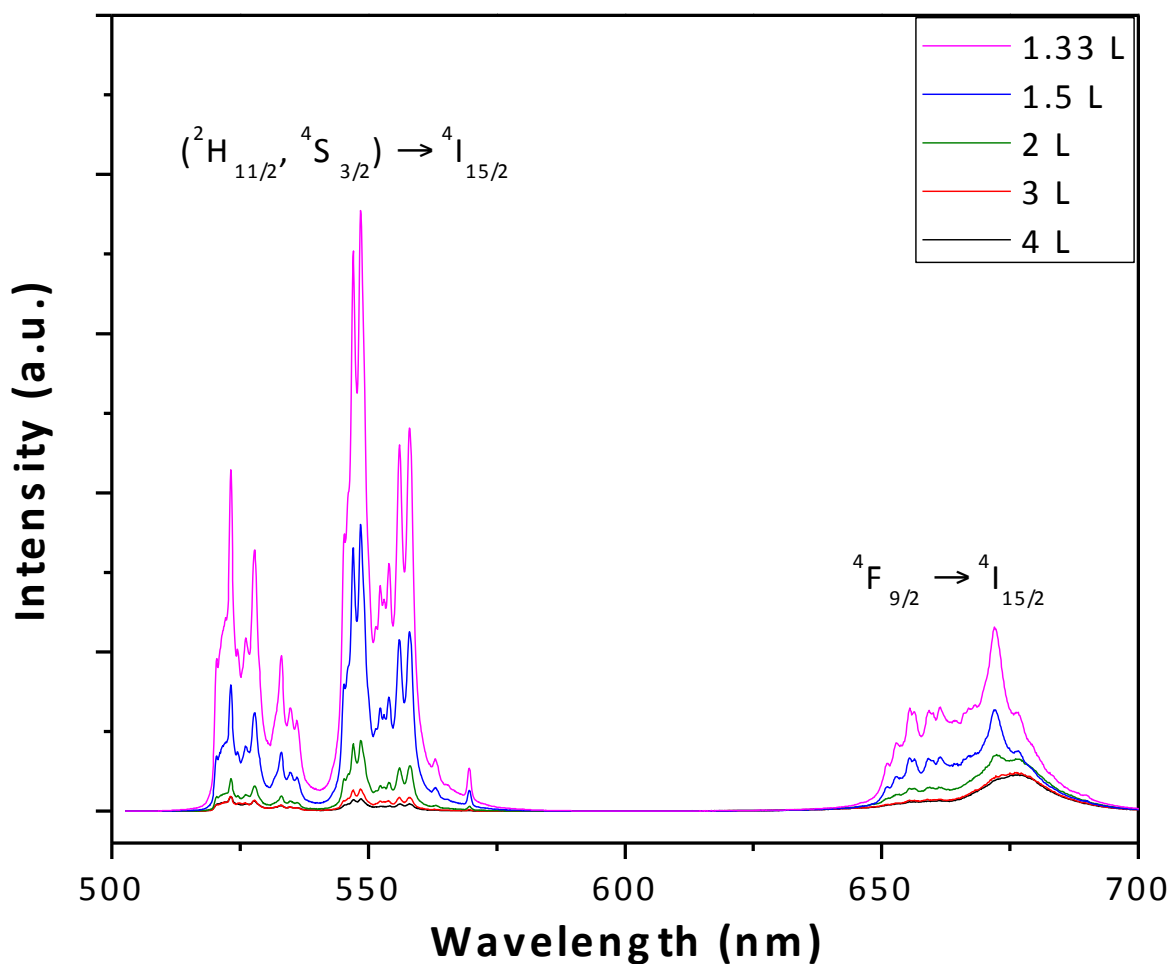


Figure 5.26: UC spectra of $\text{Gd}_2\text{O}_3:1\%\text{Er}^{3+}$ samples at different oxygen flow rates. $\lambda_{\text{exc}} = 980 \text{ nm}$.

As shown in Figure 5.27, the ratios between the red and green emissions increase at the decrease of the oxygen flow rate, and at the increase of the volumetric combustion enthalpy. The sample prepared at 4 L/min, with the lowest ΔH_{CV} , -15 KJ/L, presents the highest red/green ratio, 3.58, which decreases almost three times, 1.34, when the sample is prepared at 2 L/min. At the highest ΔH_{CV} , when the sample is prepared at 1.33 L/min, the red/green ratio decreases more than ten times, 0.44, compared to the initial value.

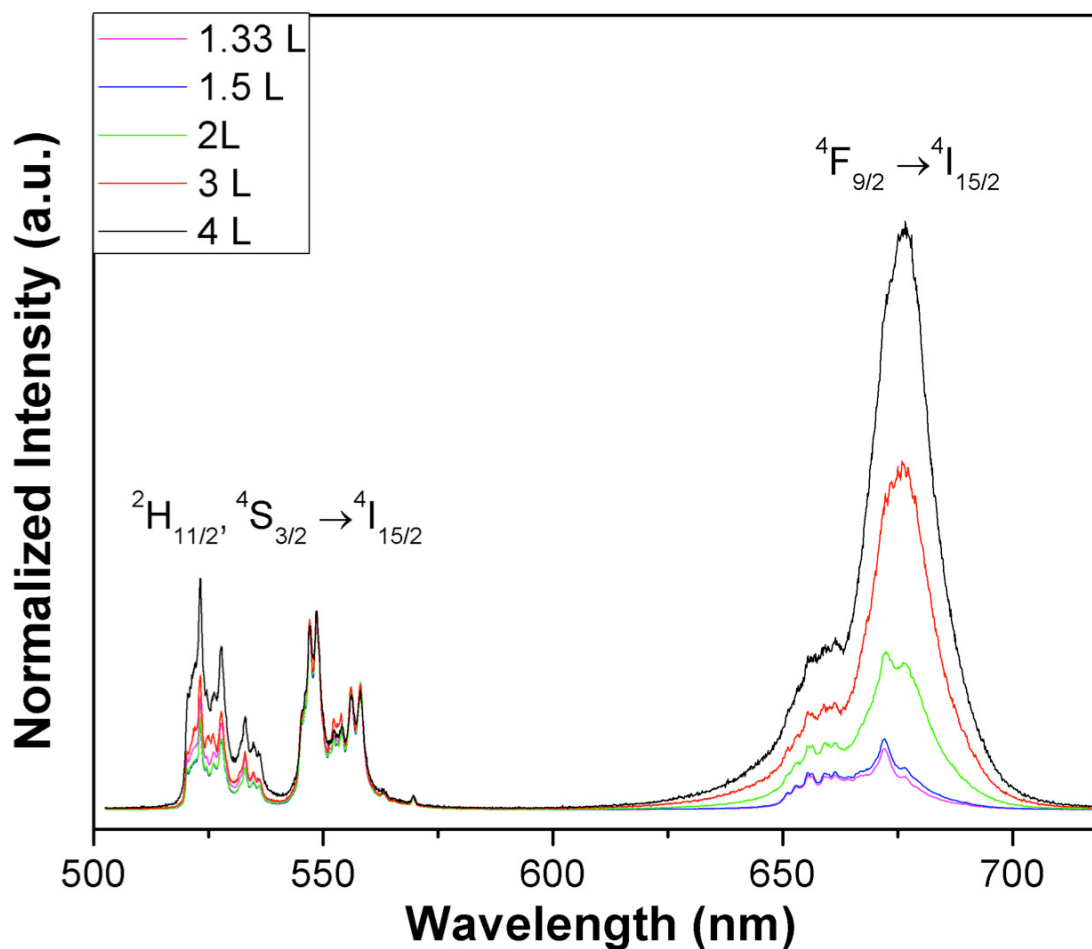
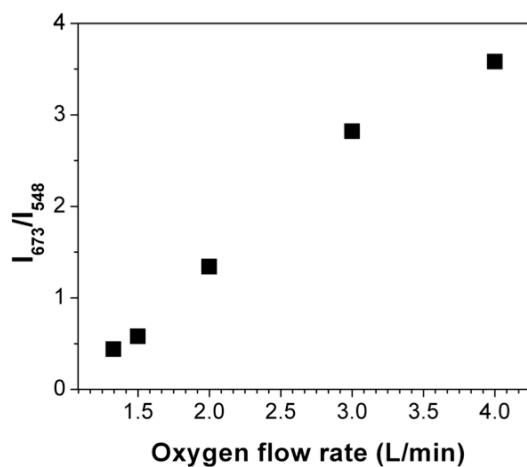


Figure 5.27: UC emission spectra, normalized to $^4S_{3/2}$, at different oxygen flow rates. $\lambda_{\text{exc}} = 980 \text{ nm}$



O ₂ flow L/min	Red/green ratio	ΔH_{cv} KJ/L _{O₂}
1.33	0.44	-45
1.50	0.58	-40
2.00	1.34	-30
3.00	2.82	-20
4.00	3.58	-15

Table 5.9: red/green ratio of the samples prepared at different oxygen flow rates

Figure 5.28: Intensity ratios between the red emission ($^4F_{9/2}$, centered at 673 nm) and the green emissions ($^2H_{11/2}$, $^4S_{3/2}$, centered at 548 nm)

At the decrease of the oxygen flow rate, when the volumetric combustion enthalpy increases, the reaction temperature increases. In fact, similarly to what observed in the previous series of samples, the TGA measurements (Figure 5.29)) show that the weigh loss decreases as the volumetric combustion enthalpy increases: from about 7.5 % at 4 L/min and -15 KJ/L, to about 5 % at 1.33 L/min and -45 KJ/L. This means that, as the reaction temperature increases, there is a lower amount of residues on the surface of the nanocrystals. Since these species could be identified with carbonates and hydroxylic groups, which act as quenching agents, the overall UC intensity emission increases (Figure 5.26) and the red/green ratio decreases (Figure 5.27).

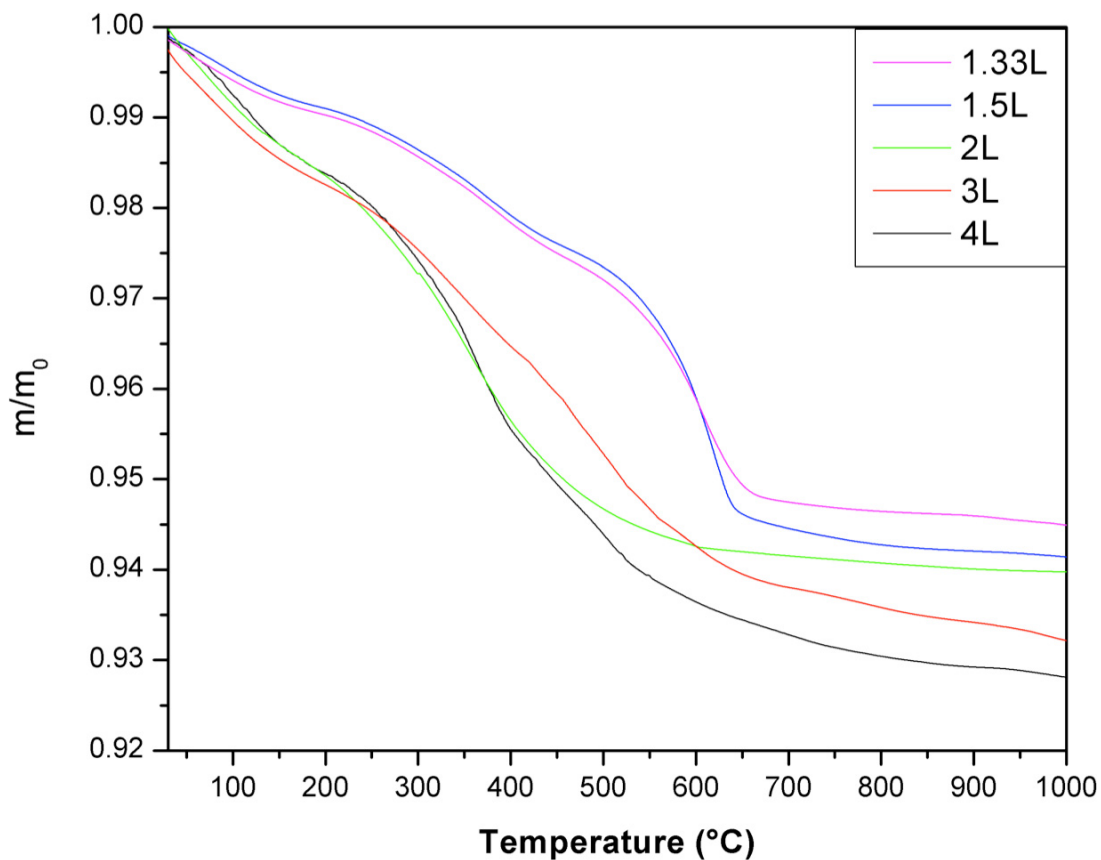


Figure 5.29: TGA measurements of $\text{Gd}_2\text{O}_3:1\%\text{Er}^{3+}$ samples at different oxygen flow rates.

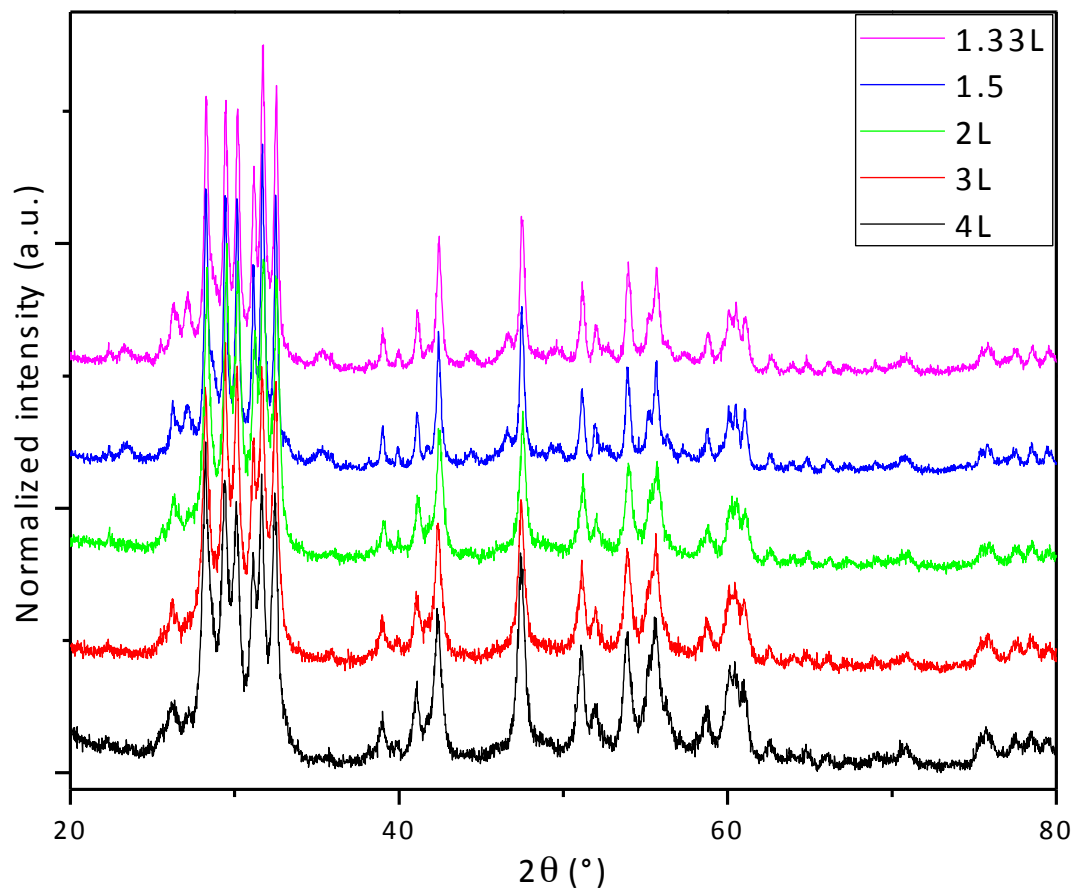


Figure 5.30: XRPD patterns of the samples prepared at different oxygen flow rates.

O₂ flow <i>L/min</i>	ΔH_{cv} <i>KJ/L_{O2}</i>	% monoclinic	d <i>nm</i>
4.00	-15	92	12
3.00	-20	90	13
2.00	-30	88	14
1.50	-40	63	20
1.33	-45	61	24

Table 5.10: Summary of the samples prepared at various oxygen flow rates, showing the volumetric combustion enthalpy, the % of monoclinic phase and the size of the particles.

The XRPD patterns (Figure 5.30) revealed the reflections of monoclinic Gd_2O_3 , with a cubic composition, variable with the variation of the oxygen flow rate. In fact, as it can be seen in Table 5.10, the percentage of monoclinic phase decreases as the oxygen flow rate decreases and the volumetric combustion enthalpy increases: from 92%, at 4 L/min and -15 KJ/L, the monoclinic composition drops to 61 % at 1.33 L/min and -45 KJ/L. Considering that at high oxygen flow rate the residence time is short and at low oxygen flow rates the residence time is long, the results are in agreement with other studies reported in literature. In fact, it has been observed that for $Y_2O_3:Eu^{3+}$ [56] monoclinic nanocrystals were synthesised at short residence time and cubic nanocrystals at long residence times.

The particle size, calculated by Scherrer equation, increased as the DHCV increases. The sample prepared at 4 L/min, at the lowest volumetric combustion enthalpy, have a particle size of 12 nm, while the sample prepared at 1.33 L/min, at the highest volumetric combustion enthalpy, have a particle size of 24 nm. In fact, as the oxygen flow rate increases, the volumetric combustion enthalpy increases and, along with it, the temperature developed during the reaction.

All the above-mentioned observations are summarized in Figure 5.31.

The key role of the oxygen flow rate is the dispersion of the precursors in the flame. It has been showed in Figure 5.13 that as the oxygen flow rate decreases the flame becomes longer. This means that the particles spend more time in the flame and their aggregation is more probable. In fact, TEM images (Figure 5.32) showed higher aggregation and bigger size as the oxygen flow rate went from 4 L/min to 1.33 L/min.

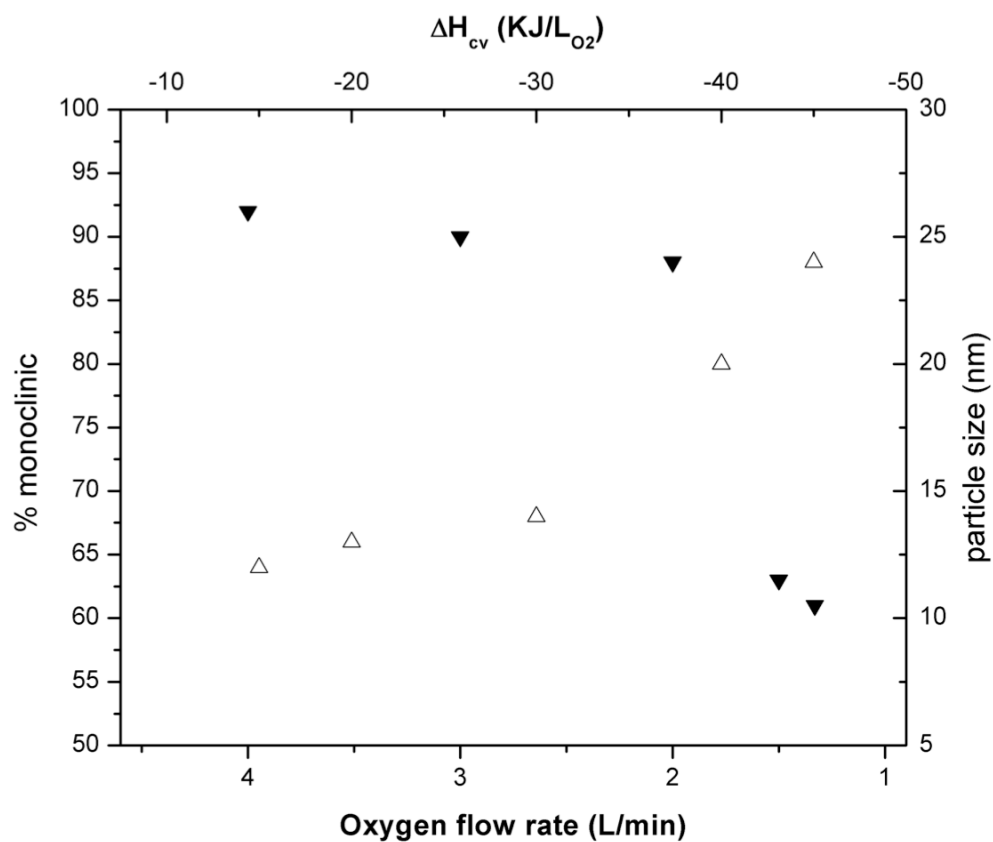


Figure 5.31: Plot showing the trend of the oxygen flow rate and the volumetric combustion enthalpy respect to the % of monoclinic phase (▼) in the products and the particle size (△).

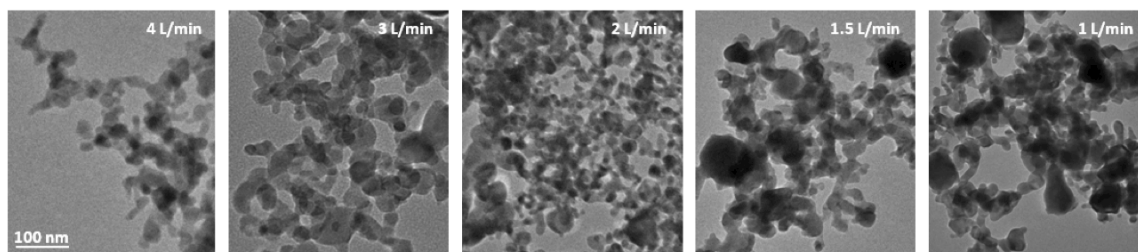


Figure 5.32: TEM images of $\text{Gd}_2\text{O}_3:1\%\text{Er}^{3+}$ samples prepared at different oxygen flow rates

5.2.7 Effect of the pressure drop

In order to study of the effect of the pressure drop on the final properties of the nanocrystals, a series of samples have been prepared at various openings of the nozzle, when the indicated pressure drop was 0 bar (nozzle completely open), 2 bar, 4 bar (Table 5.11). It was not possible to increase further the pressure drop at the exit of the nozzle, because of the limits imposed by the design of the burner. During the preparation of this series of samples, the solution and the oxygen flow rates have been kept constant at 2 mL/min and 2 L/min, respectively.

Opening of nozzle	Pressure drop <i>bar</i>
Completely open	0
Slightly closed	2
Almost completely closed	4

Table 5.11: Series of samples prepared to study the effect of the pressure drop on the final properties of the nanocrystals. Precursor solution flow rate is kept at 2 mL/min and the oxygen flow rate at 2l/min.

The prepared samples have been excited at 980 nm and the UC emission have been observed. Similarly to the previous samples, the main emission peaks were in the green (${}^2H_{11/2}, {}^4S_{3/2} \rightarrow {}^4I_{15/2}$) and in the red (${}^4F_{15/2} \rightarrow {}^4I_{15/2}$), as it can be seen in Figure 5.33. The shape of the spectra does not change, but the overall emission increases as the pressure drop decreases, which is when the nozzle is closed and the flame is longer.

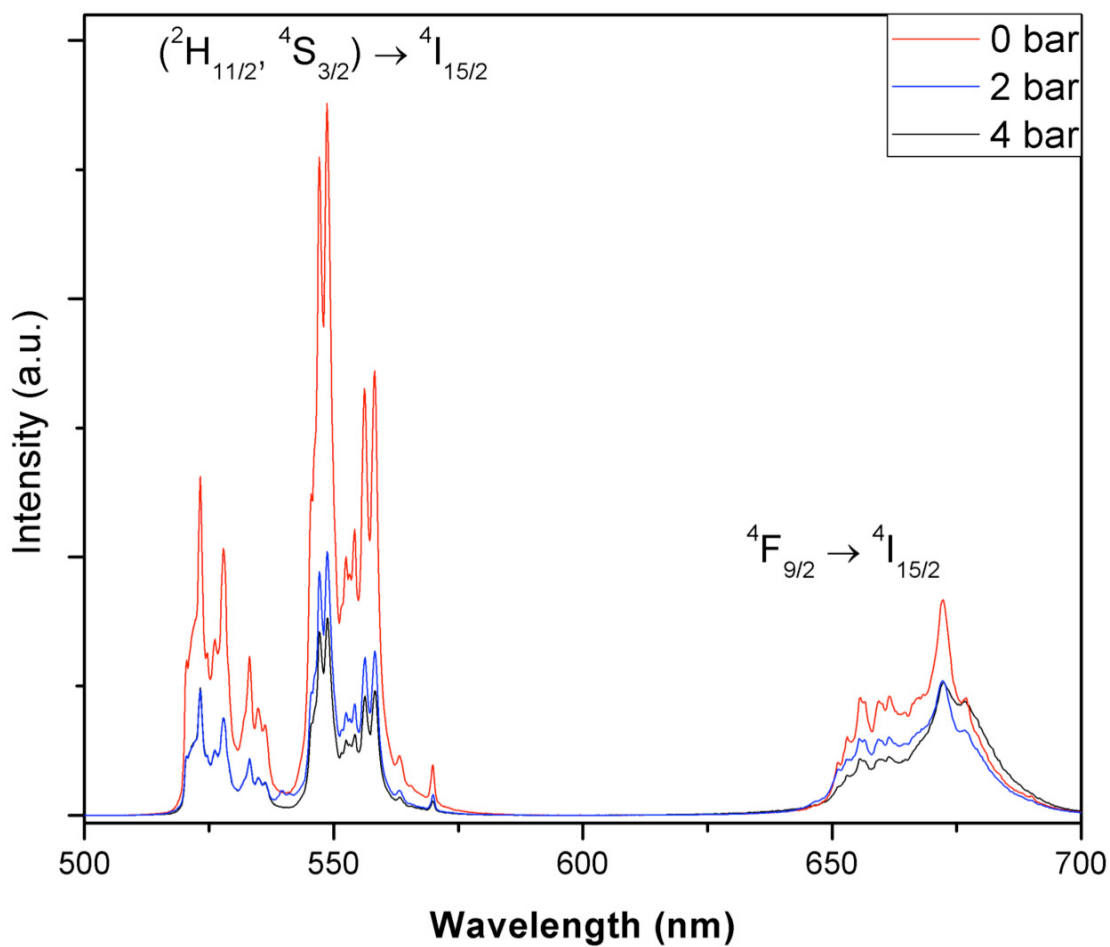


Figure 5.33: UC emission spectra at different pressure drops. $\lambda_{\text{exc}} = 980 \text{ nm}$

When the spectra are normalized to the green emission ($^4S_{3/2}$), it can be observed that the red emission increases as the pressure drop increases and, as a consequence, when the flame is shorter.

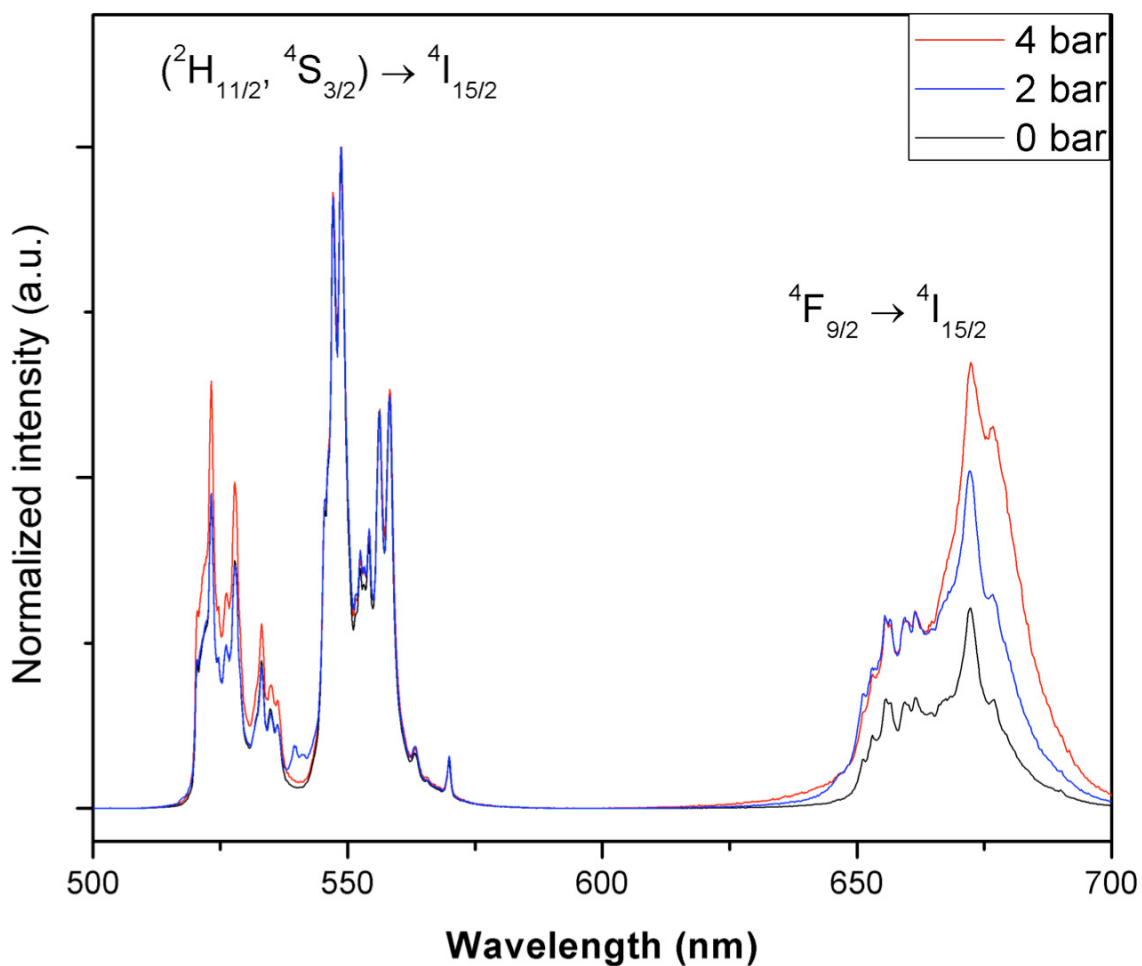


Table 5.12: UC emission spectra, normalized to $^4S_{3/2}$, at different pressure drops. $\lambda_{\text{exc}} = 980 \text{ nm}$.

The luminescence behaviour is explained by the results obtained with the XRPD analysis and the calculation of the crystal size by Scherrer equation (Table 5.13). In fact, the particle size resulted to decrease, from 16 nm to 11 nm, as the pressure drop is increasing, from 0 to 4 bar. This means that the increase in the luminescence observed in Figure 5.33 is due to a size effect: as the size of the nanocrystals increases, the intensity of the luminescence increases as well.

ΔP <i>bar</i>	<i>d</i> <i>nm</i>
0	16
2	14
4	11

Table 5.13: size of the nanocrystals prepared at different pressure drops.

The aperture of the nozzle does not have any direct influence in the calculated volumetric combustion enthalpy and, consequently, in the reaction temperature. However, as showed in Figure 5.14, the aperture of the nozzle has an effect on the length of the flame: when the nozzle is completely open ($\Delta P = 0$ bar), the flame is the longest and while the nozzle is closed ($\Delta P = 2, 4$ bar) the height of the flame shortens.

In fact, the opening of the nozzle affects predominantly the discharge velocity of O_2 : the higher the velocity, the shorter the flame. According to the available literature [126], as the nozzle is closed, the flow of the oxygen goes from subsonic to sonic to supersonic. A similar behaviour is expected for the system used in this work. However, a detailed study of the flow dynamics of this system is not part of the purpose of this thesis.

Considering the experimental observations (mainly the shape and the noise of the flame), it can be assumed that at 0 bar the oxygen flow rate is subsonic, at 2 bar is sonic and at 4 bar is supersonic.

5.3 Enhancement of the luminescence

In order to be used commercially, luminescent nanomaterials need to show very bright emission intensity. In order to achieve this, two aspects can be considered:

- Selection of the dopants: different dopants, with appropriate concentration, can improve the probability of energy transfer, with the consequent enhancement of the luminescence.
- Host materials. When the phonon energy of the host materials is low, the gaps between the energy levels are not easily filled and, as a consequence, the non-radiative relaxations, which have a quenching effect, are less probable. Moreover, the intensity is increased when Ln^{3+} ions are inserted in low symmetry sites, because of the release of selection rules, which allow transitions, otherwise forbidden.

5.3.1 Combination of dopants: Er³⁺ and Yb³⁺

As explained in Chapter 5.2, the development of the FSP synthesis has been carried out with materials doped with only Er³⁺, for simplicity reasons. However, when Er³⁺ is combined with Yb³⁺, the upconversion emission intensity is enhanced. In fact, the ²F_{5/2} state of Yb³⁺ is resonant with the ⁴I_{11/2} state of Er³⁺, and has a high absorption cross section, which makes this ion an ideal candidate to increase the efficiency of the upconversion process.

The results explained in the previous sections showed that the intensity of the luminescence of Gd₂O₃: Er³⁺ samples is the highest with a precursor solution of 90% toluene in 2EHA, injected at 2mL/min, 2L/min of O₂ and with a pressure drop of 2 bar. Therefore, a sample containing 1% of Er³⁺ and 1% of Yb³⁺ has been prepared in the above-mentioned conditions and the luminescence of the two samples has been compared (Figure 5.34).

As expected, the sample codoped with Er³⁺ and Yb³⁺ is almost three times (2.7) more intense than the sample singularly doped with Er³⁺. The enhancement of the luminescence is a direct consequence of the presence of Yb³⁺, which pumps more photons and increase the probability of energy transfers with the Er³⁺ energy levels.

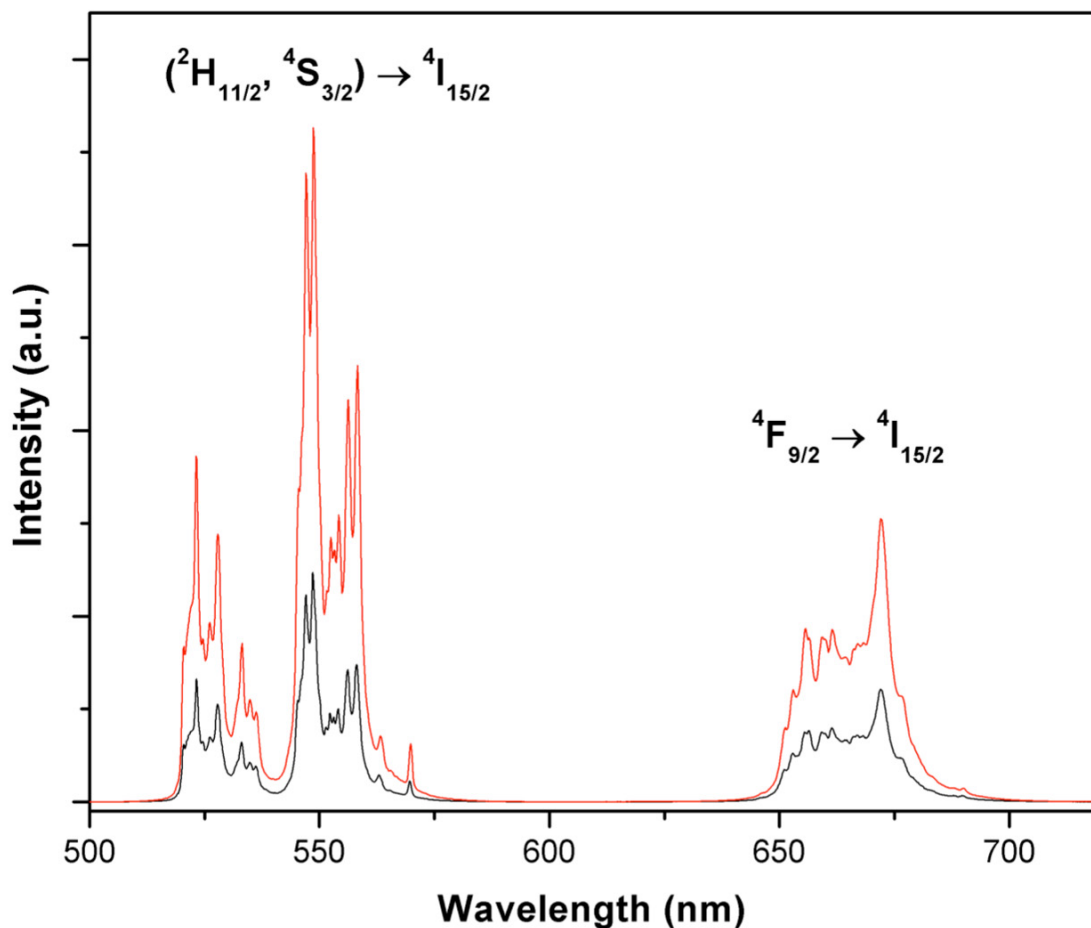


Figure 5.34: UC spectra of $\text{Gd}_2\text{O}_3:1\%\text{Er}^{3+}$ (-) $\text{Gd}_2\text{O}_3:1\%\text{Er}^{3+}, 1\%\text{Yb}^{3+}$ (-) samples. $\lambda_{\text{exc}} = 980 \text{ nm}$.

Moreover, the ratio between the red emission (${}^4\text{F}_{9/2} \rightarrow {}^4\text{I}_{15/2}$) and the green emission ($({}^2\text{H}_{11/2}, {}^4\text{S}_{3/2}) \rightarrow {}^4\text{I}_{15/2}$) slightly increases, from 1.5 for the Er^{3+} -doped sample to 1.8 for the $\text{Er}^{3+}, \text{Yb}^{3+}$ -doped sample. The increase in the red emission is due to the energy transfer mechanisms (Figure 5.35). In fact, in addition to the mechanisms described for the Er^{3+} -doped samples (Figure 5.7), Yb^{3+} ions contribute to the energy transfer from the excited ${}^2\text{F}_{5/2}$ state to the ${}^4\text{I}_{11/2}$ states of Er^{3+} . This energy transfer contributes also to the population of the ${}^4\text{F}_{9/2}$ level and, as a consequence, the red emission is enhanced.

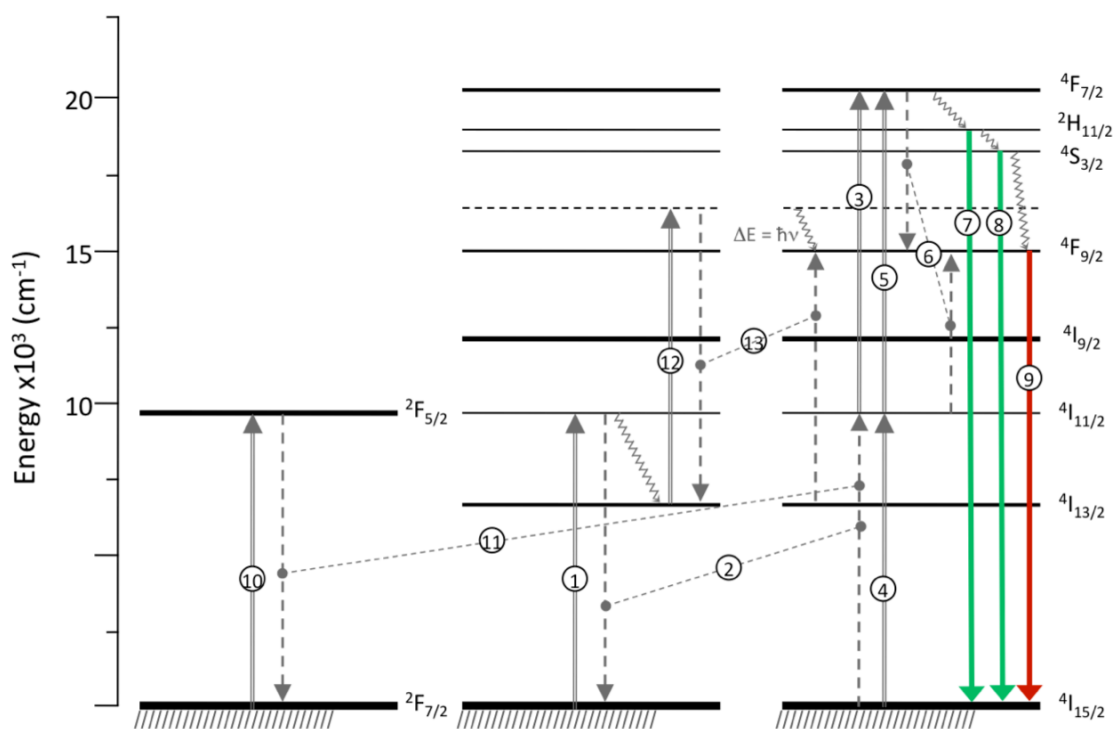


Figure 5.35: Upconversion mechanisms responsible for the green (7-8) and red (9) emission in Er^{3+} , Yb^{3+} -doped Gd_2O_3 nanocrystals. – (1-2-3) energy transfer upconversion (ETU), (4-5) excited state absorption (ESA), and (6) cross relaxation [$^4\text{F}_{7/2}$, $^4\text{I}_{11/2}$] \rightarrow [$^4\text{F}_{9/2}$, $^4\text{F}_{9/2}$] (CR), (10-11-3) ETU from Yb^{3+} , (12-13) ETU and lattice dissipation.

As seen previously, the $^4\text{F}_{9/2}$ level can be populated, not only by non-radiative relaxation from the $^4\text{S}_{3/2}$ level, but also from cross-relaxation between the $^4\text{F}_{7/2} + ^4\text{I}_{11/2}$, $^4\text{F}_{9/2} + ^4\text{F}_{9/2}$ levels. In particular, in presence of Yb^{3+} ions, the CR is enhanced.

However, Yb^{3+} ions increase the probability of another mechanism that contributes to the population of the $^4\text{F}_{9/2}$ level. A 980nm pump photon excites the Yb^{3+} ions from the ground state to the $^2\text{F}_{7/2}$ excited state that, by energy transfer, donates its energy to a neighbouring Er^{3+} ion, which is, consequently, excited to the $^4\text{I}_{11/2}$ level. After this, the ion decays non-radiatively to the $^4\text{I}_{13/2}$ lower lying level.

Since the energy gap between the $^4I_{11/2}$ and $^4I_{13/2}$ states is approximately equal to 3600 cm^{-1} , the high-energy phonons of carbonates and hydroxylic groups present on the surface of the nanocrystals could fill this gap. When the ion is in the $^4I_{13/2}$ excited level, another energy transfer from a neighbouring Yb^{3+} ion in the $^2F_{7/2}$ excited state populates the $^4F_{9/2}$ level, leaving a small excess of energy (about 1600 cm^{-1}), which is dissipated by the lattice of the nanocrystals. As a result, this mechanism further populates the $^4F_{9/2}$ energy state and contributes to the enhancement of the red emission in samples codoped with Yb^{3+} , particularly at high concentrations.

5.3.2 Combination of dopants: alkali metals

With the objective of further enhancing the emission intensity, a series of samples of $\text{Gd}_2\text{O}_3: \text{Er}^{3+}, \text{Yb}^{3+}$ codoped with 1% of alkali metals was prepared. In the following discussion, the sample doped with only Er^{3+} and Yb^{3+} is used as reference and defined as blank.

The UC spectra of the samples, upon excitation at 980 nm, are illustrated in Figure 5.36.

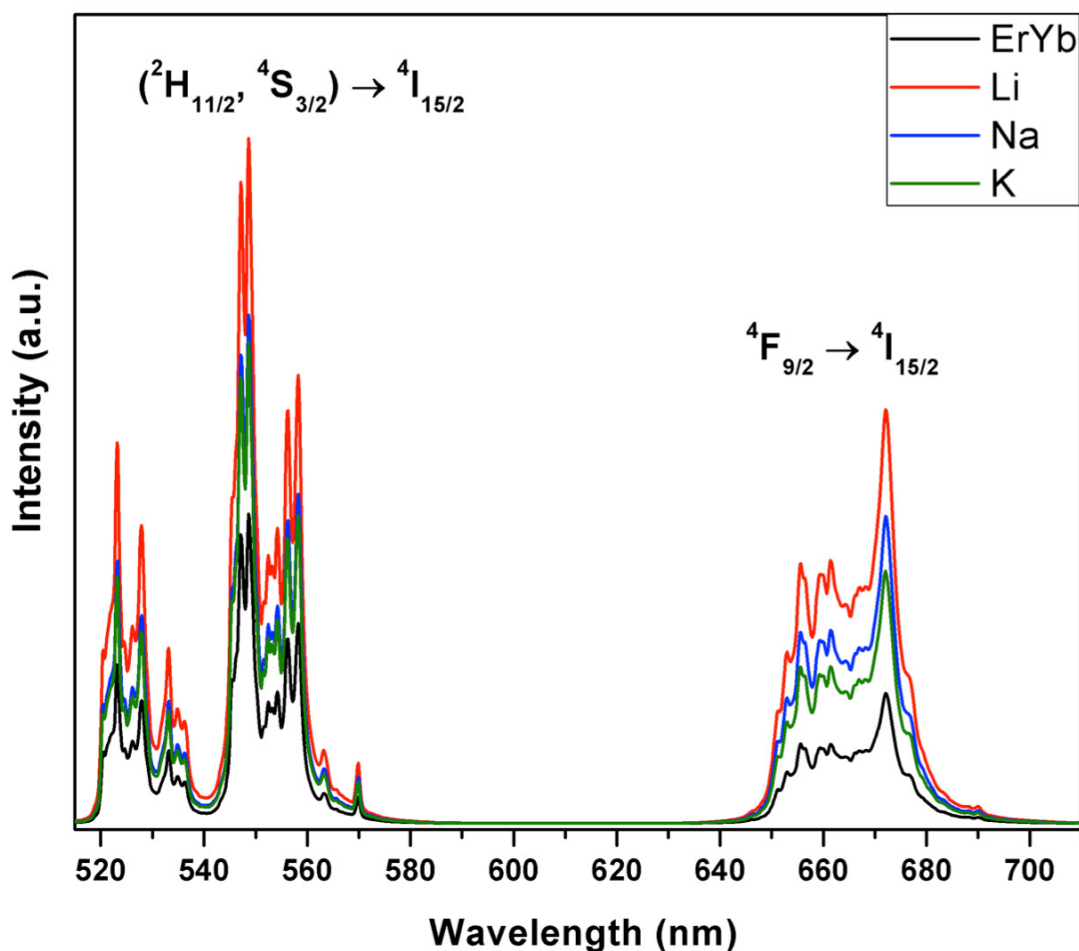


Figure 5.36: UC spectra of $\text{Gd}_2\text{O}_3:1\%\text{Er}^{3+}, 1\%\text{Yb}^{3+}, 1\%M^+$ samples, where M^+ is an alkali metal. $\lambda_{\text{exc}} = 980$ nm.

The shape of the overall spectra is the same, but the intensity of the emission increases when alkali metals are added, with the highest effect with Li^+ .

In particular, the intensity increases almost twice with K^+ (1.7) and Na^+ (1.9) and reaches the highest value with Li^+ (2.6). The ratios between the red emission ($^4\text{F}_{9/2}$) and the green emissions ($^2\text{H}_{11/2}$, $^4\text{S}_{3/2}$) increase with the incorporation of the alkali metals, but do not vary significantly within the alkali metal-doped samples (Table 5.14).

Alkali Metal ion	Red/green ratio	ionic radius (pm)
blank	0.55	-
Li^+	0.68	76
Na^+	0.77	102
K^+	0.75	138

Table 5.14: Red/green ratios of alkali metal-doped samples.

Most commonly, a cation is incorporated in a crystal replacing the cation of the matrix. However, considering the charge mismatch that would be created with the incorporation of alkali metals in this way and the size of these ions, it is more probable that alkali metals would be inserted in the interstitial sites of the lattice.

The size of the ions and their volume are summarized in Table 5.15. In particular, the very small size of the Li^+ ion emerges, in comparison with the other ions and supports the hypothesis that Li^+ ions would occupy the interstitial sites of the crystals instead of replacing the Gd^{3+} ions.

	Ion	Ionic radius (pm)	Volume of ion (\AA^3)
Alkali Metals	Li^+	76	230
	Na^+	102	556
	K^+	138	1376
Lanthanides	Gd^{3+}	93.8	432
	Yb^{3+}	86.8	342
	Er^{3+}	89	369

Table 5.15: size of the ionic radii of the alkali metals and of the Ln^{3+} ions

The samples have been analyzed by XRPD analysis and the patterns have been refined with the Rietveld method, in order to observe the changes in the lattice parameters. As shown in Figure 5.37, the XRPD patterns revealed the reflections of monoclinic Gd_2O_3 , with a cubic composition, variable with the type of alkali metal incorporated in the crystal. In general, the shape of the XRPD patterns does not show significant changes after the incorporation of alkali metals.

The refinement did not show any significant change in the lattice parameters (Table 5.16) to clarify the role of Li^+ in the crystal and the particle size is very similar for all the samples. With this last information, in particular, an enhancement of the luminescence due to a size effect can be excluded.

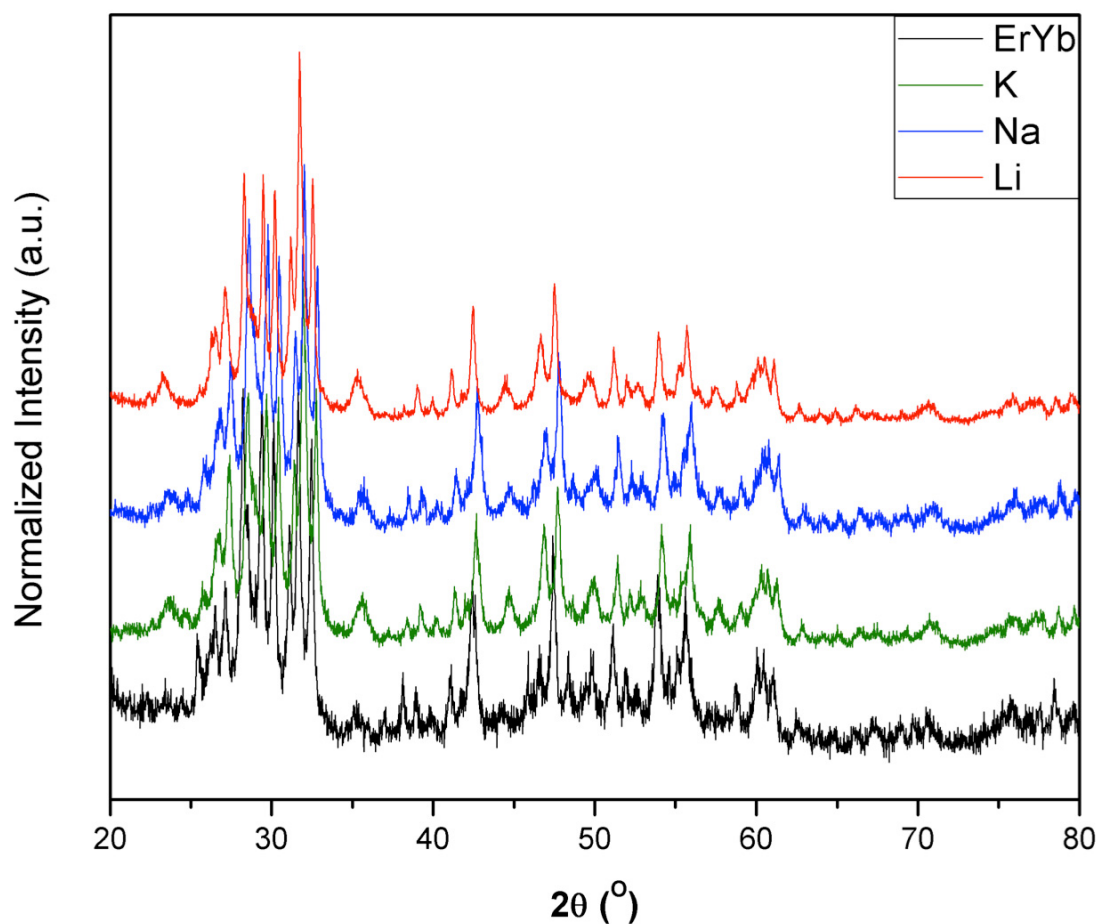


Figure 5.37: XRPD analysis of $\text{Gd}_2\text{O}_3:1\%\text{Er}^{3+}, 1\%\text{Yb}^{3+}, 1\%\text{M}^+$ samples, where M^+ is an alkali metal.

	1 % Er^{3+} 1% Yb^{3+}	1 % Er^{3+} 1% Yb^{3+} Li^+	1 % Er^{3+} 1% Yb^{3+} Na^+	1 % Er^{3+} 1% Yb^{3+} K^+
ionic radius (Å)		76	102	138
a	14.111	14.109	14.002	14.128
b	3.576	3.578	3.536	3.581
c	8.7738	8.772	8.686	8.781
β	100.017	100.058	99.903	100.036
volume	436.0	436.0	423.6	437.5
size (nm)	15.6	15.9	15.9	15.5

Table 5.16: Cell parameters calculated by Rietveld refinement of the samples doped with alkali metals.

In order to better understand the luminescence behaviour, the decay times of the green emitting state ($^4S_{3/2}$) have been measured, upon excitation at 355nm (Table 5.17). The values are in good agreement with previous results [24].

Sample	Decay time (μs)
blank	34.1
K^+	57.3
Na^+	56.2
Li^+	95.6

Table 5.17: Decay times (τ) of the alkali metal undoped and alkali metal doped $\text{Gd}_2\text{O}_3:1\text{Er}^{3+},10\text{Yb}^{3+}$

An example of the obtained curve is shown in Figure 5.38. As the excitation is done directly to the Er^{3+} ions, the temporal decay shows an exponential behaviour with time. The lifetimes have been calculated from the fitting of the curves.

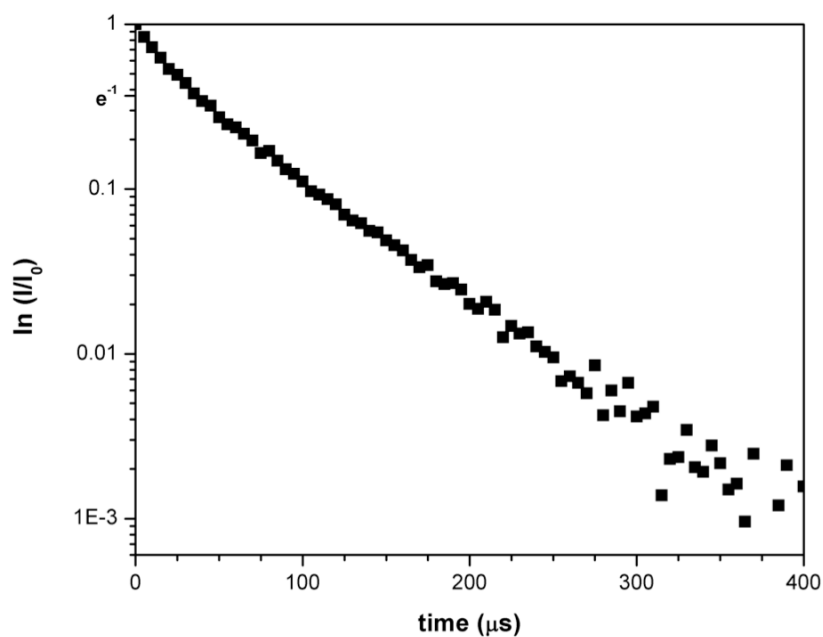


Figure 5.38: Decay time curve of $\text{Gd}_2\text{O}_3:1\%\text{Er}^{3+}, 1\%\text{Yb}^{3+}$ sample at the green emitting state ($^4S_{3/2}$).

In agreement with the trend observed for the luminescence intensity, the decay times increase along the period of the alkali metals. In particular, an increment is observed from the blank to the samples doped with K^+ and Na^+ , which show similar values. When Li^+ is added, the decay time dramatically increases of almost three times, compared to the blank.

The protraction of the decay times is attributed either to an increase of the probability of energy transfers or to an increase in the Er^{3+} luminescence. Considering that the samples are excited at 355 nm, an increase in the energy transfer should not be appreciated under UV excitation, because, in these conditions, Er^{3+} energy levels are directly excited. The variation of the values of the decay times according to the size of the alkali metals suggests that the presence of alkali metal ions in the matrix increases the luminescence of Er^{3+} emission, because of the distortions that they create in the Er^{3+} ion environment. Therefore, it can be assumed that the presence of alkali metal ions in the lattice generates distortions around the lanthanide sites, with a decrease in the symmetry.

In order to obtain a better understanding of the behaviour of the alkali metals in G_2O_3 crystals, it would be necessary to carry more sophisticated structural analysis, which would involve a synchrotron. However, various studies on luminescent oxides doped with Li^+ reported a significant enhancement in the emission intensity[88,95,104,127-130].

Some studies attribute to this phenomenon a variation in the Er-O bonds, with the consequent formation of oxygen vacancies and distortion of the sites. Up to date, however, the explanation of the effect of Li^+ ions on luminescent materials is not entirely clear and leaves several open questions, whose answers are beyond the objective of this thesis.

5.3.3 Host materials: preparation of GdVO₄

Flame Spray Pyrolysis has been widely used for the preparation of binary oxides, as luminescent materials, but any compound produced via combustion synthesis can be prepared by FSP. However, the main limitation lies in the availability of precursors that can be dissolved in organic solvents and form stable solutions.

In order to increase further the luminescence intensity, GdVO₄ was chosen, as it is not hygroscopic as Gd₂O₃ and it presents brighter emission. This crystal is not only an interesting lasing material, but also contains gadolinium, which could be used in compounds for Magnetic Resonance Imaging and biological applications.

Initially, nanostructured gadolinium vanadate doped with 1% Er³⁺ was prepared with a solution made with acetate ions. Gadolinium acetate, Vanadyl acetate and Erbium acetate were heated at 60°C and stirred for 20 minutes. The resulting green limpid solution was stable. Some crystals were formed after 48 hours, but they were easily dissolved after heating the solution. The resulting samples were powders of a green colour and they did not show UC emission. After treatment at 500°C for 2 hours, the samples were still slightly green and turned white only after being treated at 800°C for 2 hours. After this further thermal treatment, the samples showed bright green emission UC after excitation at 980nm. The green colour of the as-prepared samples was probably the result of incomplete combustion residues, which have been decomposed after thermal treatment.

The XRPD analysis revealed the phases of gadolinium orthovanadate (JCPDS 86-0996), with space group $I41/amd$ (space group no. 141). The vanadate structure is confirmed for all the samples, treated and untreated. However, the sample treated at 800°C shows higher crystallinity than the others, as it is suggested by the sharp peaks.

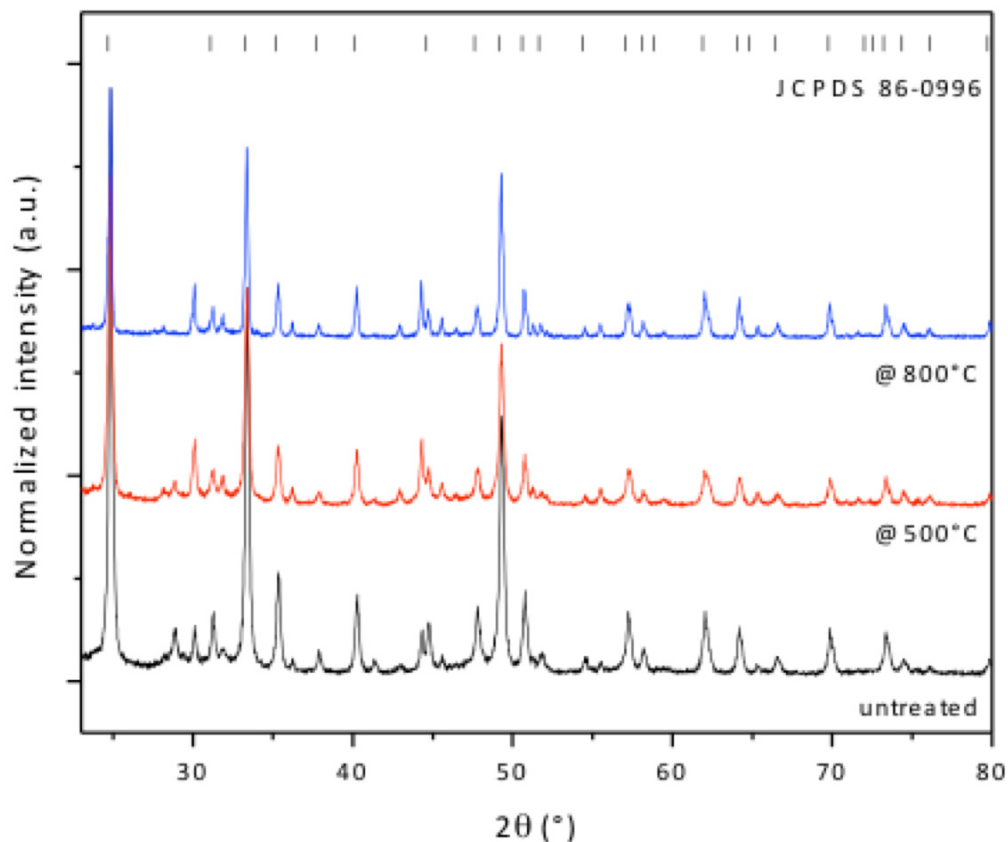


Figure 5.39: XRPD patterns of GdVO₄:1%Er³⁺.

GdVO₄ has a zircon-type structure (Figure 5.40) and the lanthanide ions replace the gadolinium ions sites, which are coordinated with dodecahedral oxygen and have D_{2d} symmetry [131].

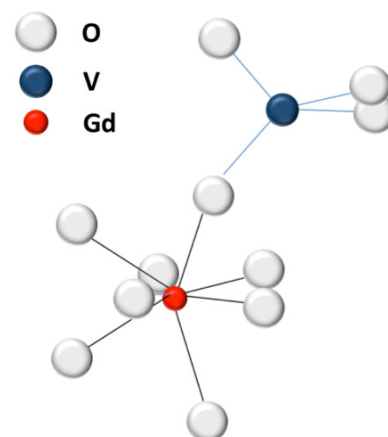


Figure 5.40: structure of GdVO₄.

As showed in TEM images (Figure 5.41), the nanocrystals are slightly aggregated and have the typical morphology of the materials prepared by FSP. The presence of visible lattice fringes in the high-resolution image is in agreement with the high crystallinity observed in the XRD analysis. The distance between the lattice fringes measures 4.64 Å, which is attributed to the (101) planes of GdVO₄ and is in agreement with the value reported in literature, 4.76Å (JCPDS 86-0996).

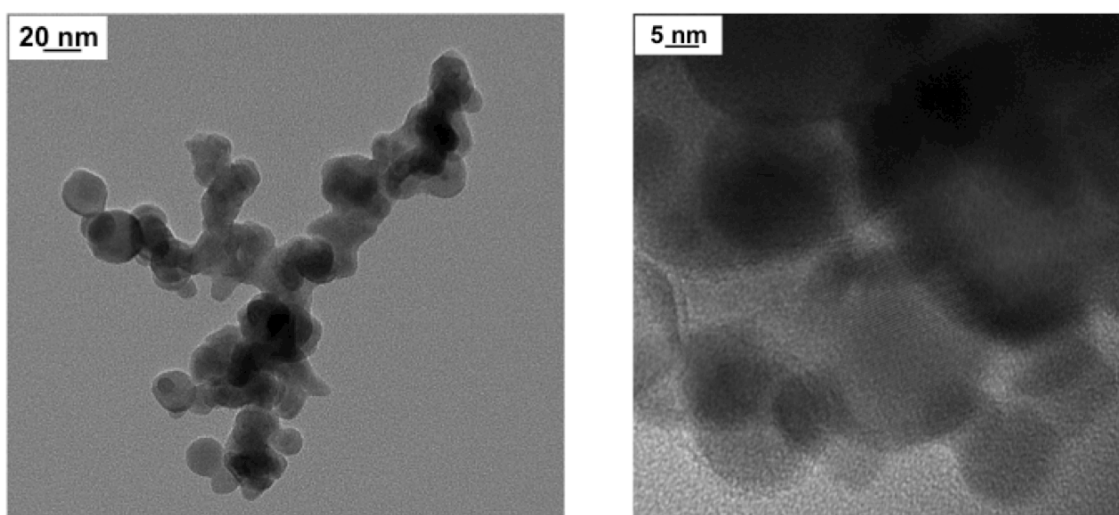


Figure 5.41: TEM images of GdVO₄: 1%Er³⁺

The sample treated at 800°C showed upconversion emission, after excitation at 980 nm, with two predominant emissions in the green and in the red (Figure 5.42).

The green emission peaks centered at 525 nm and 549 nm, were attributed to the $^2H_{11/2} \rightarrow ^4I_{15/2}$ and $^4S_{3/2} \rightarrow ^4I_{15/2}$ transitions, while the peak in the red emission region, centered at 671 nm, was attributed to the $^4F_{9/2} \rightarrow ^4I_{15/2}$ transition.

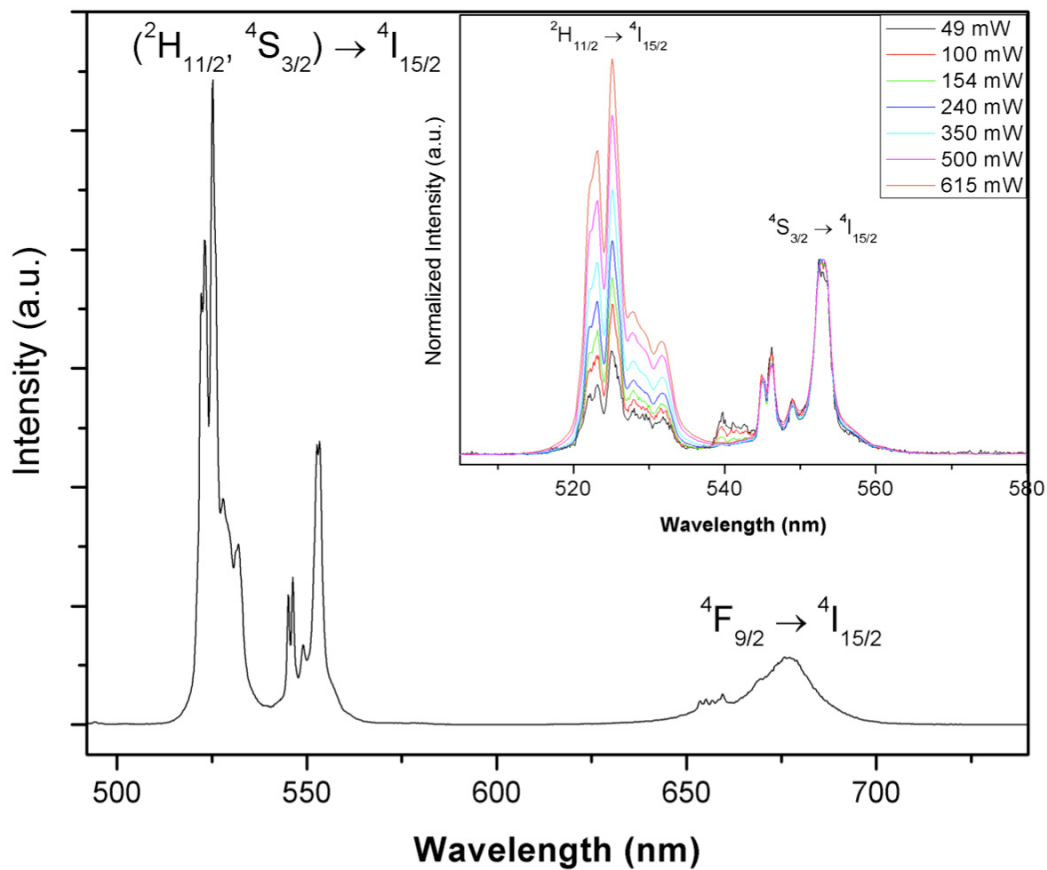


Figure 5.42: UC emission of $\text{GdVO}_4:1\text{Er}^{3+}$. $\lambda_{\text{exc}} = 980 \text{ nm}$. The inset shows the emission of the sample, normalized at the ${}^4\text{S}_{3/2}$ peak, at different excitation power.

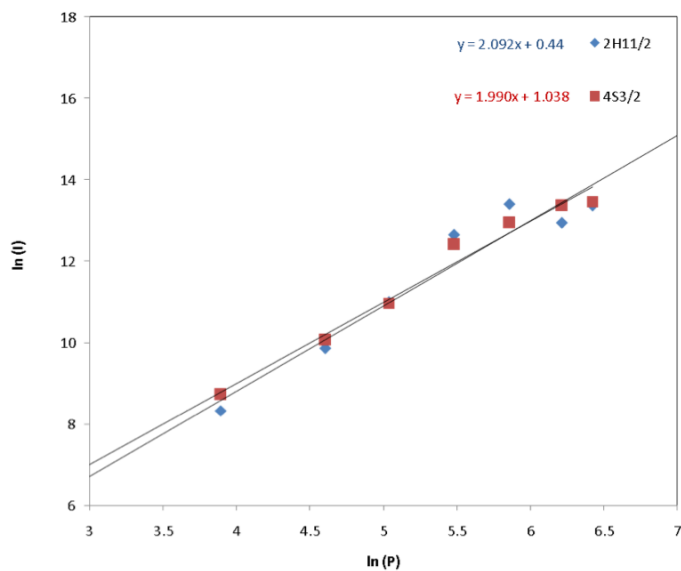


Figure 5.43: Power study of the $\text{GdVO}_4:1\text{Er}^{3+}$ upon excitation at 980 nm .

Emission spectra were collected at different excitation powers. As the excitation power is increased from 50 mW to 615 mW, the emission intensity increased (Figure 5.43) and affected, particularly, the ratio between the ${}^2\text{H}_{11/2}$ and the ${}^4\text{S}_{3/2}$ manifolds (Figure 5.42 inset). In fact, the ${}^2\text{H}_{11/2}$ energy level, which is separated from the lower lying level ${}^4\text{S}_{3/2}$ by a small energy gap (about 700 cm^{-1}), is hypersensitive. When part of the energy excitation beam is dissipated as heat, the temperature in the local environment of the Er^{3+} ions increases and, as a consequence, the ${}^2\text{H}_{11/2}$ level could be populated by thermalization. The UC mechanism is similar to the one described previously for Gd_2O_3 and the slope of the curves $\ln(P)$ vs $\ln(I)$ confirmed that the excitation process occurs via two photons.

In order to prepare the samples in one step, without further thermal treatment, a mixture of xylene and 2EHA in ratio 7:3, with higher combustion enthalpy than 2EHA, has been used as solvent. The samples were white as-prepared and showed bright green luminescence, visible by the naked eye. The one step sample has been analyzed as the previous ones, leading to the same results.

The results of the prepared GdVO_4 are important not only because this NC show a bright luminescence intensity, but also because, to our knowledge, this is the first time that the synthesis of upconverting GdVO_4 prepared by FSP has been reported.

5.4 Core shell systems

Nanostructured oxides can be integrated in core-shell systems for two different reasons, both with the purpose of using these materials for biological applications. Firstly a silica shell facilitates the functionalization of nanocrystals and their water dispersibility. Secondly, a magnetic core aims for the preparation of multifunctional systems, such as magnetic and luminescent.

The results reported in this section are only preliminary and the focus is mainly oriented on the silica coating.

The previously described Gd_2O_3 , 1% Er^{3+} , 1% Yb^{3+} , 1% Li^+ nanocrystals prepared with FSP have been chosen as a core, because of their high intensity luminescence. A 0.1 M solution of the prepared oxides and TEOS have been sonicated for 30 min and used as precursor solution for the FSP.

The nanocrystals were still showing green luminescence. However, the emission intensity decreased, compared to the samples used as core, because of the presence of the silica layer, which probably absorbs part of the excitation intensity, along the light path. In fact, the measured decay times decrease as well for both the emissions, in the red and in the green.

The prepared $\text{Gd}_2\text{O}_3:1\text{Er}^{3+}, 1\text{Yb}^{3+}, 1\text{Li}^+@ \text{SiO}_2$ have been characterized by TEM analysis and clearly show silica coating around the Gd_2O_3 nanocrystals. Clearly, the core show aggregation, which is inevitable considering the nature of the synthesis employed for the preparation of the nanocrystals.

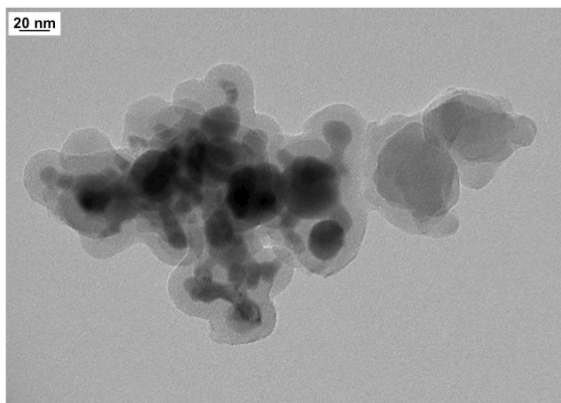


Figure 5.44: core-shell $\text{Gd}_2\text{O}_3:1\text{Er}^{3+}, 1\text{Yb}^{3+}, 1\text{Li}^+@ \text{SiO}_2$ prepared by FSP

For comparison, the nanocrystals have been coated also via the Stöber method (experimental details in Chapter 4.3.1), a traditional wet synthesis for silica coating. The nanocrystals have been characterized by TEM analysis and showed a similar morphology to what already observed for the samples prepared by FSP (Figure 5.45).

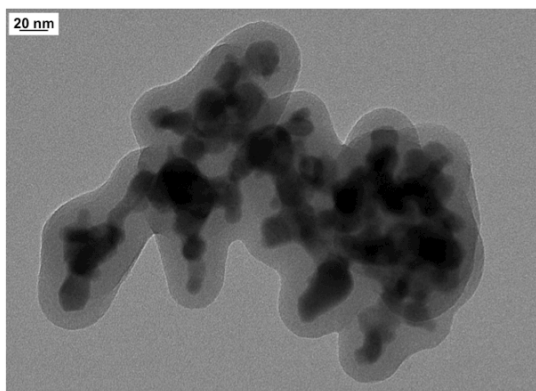


Figure 5.45: core-shell $\text{Gd}_2\text{O}_3:1\text{Er}^{3+}, 1\text{Yb}^{3+}, 1\text{Li}^+@ \text{SiO}_2$ prepared by Stöber method.

The main difference between the two synthesis is represented only by the time needed to prepare the core-shell systems: the Stöber method requires almost three days of reaction, while the FSP requires only one hour and half to prepare both core and core-shell system. This is considered really advantageous, mainly for scale-up purposes. However, the aggregation of the core nanocrystals is a limitation of the method, mostly if the nanocrystals are designed for biological applications.

During the preliminary studies, a one step FSP synthesis has been attempted, without success. In fact, the TEM images did not show any coating around the particles, suggesting the formation of composite systems.

6. *Conclusions*

6.1 From Combustion synthesis to FSP

A comparison of the structural, morphological and upconversion properties of Er^{3+} -doped Gd_2O_3 nanocrystals (mainly in the monoclinic phase) prepared by propellant synthesis and flame spray pyrolysis (FSP) was carried out. The nanocrystal samples prepared by FSP showed greater uniformity and less aggregation, which are desired morphological properties in various applications, such as in the display field. The upconversion emission intensity, following 980 nm excitation, was higher for the samples synthesized by FSP, without the requirement for further thermal treatment to eliminate the un-decomposed residues.

Moreover, enhancement in the red emission was observed following an increase of the dopant concentration (0.1, 1 and 10 mol%) in both samples. Low aggregation, uniformity and strong emission intensity, added to the possibility of varying the synthetic settings to modulate the properties of the final products, confirmed the high potential of the FSP technique for the production of Ln^{3+} -doped upconverting nanocrystals in one step.

6.2 Development of Flame Spray Pyrolysis

Summarizing the results reported in Chapter 5.2.5-5.2.7, the intensity of the luminescence increases when the precursor flow rate increases or the oxygen flow rate decreases or the nozzle is being closed (Table 6.1).

Increase of	ΔH_{CV}	d	% monoclinic	Luminescence intensity
Precursor solution flow rate	↗	↗	↘	↗
Oxygen flow rate	↘	↘	↗	↘
Nozzle opening	-	↘	-	↘

Table 6.1: Summary of the effects of the synthesis parameters on the final products. ↗ indicates an increase and ↘ indicates a decrease.

In general, when the synthesis is carried in conditions where the volumetric combustion enthalpy increases, the temperature developed in the flame increases and the particle size of the produced nanocrystals increases as well. Although the monoclinic component of the products decreases, the size effect is predominant and the intensity of the luminescence is enhanced.

The aperture of the nozzle does not have any effect on the volumetric combustion enthalpy, but it mainly affects the velocity of the oxygen at the exit of the line. This influences the length of the flame, with an effect on the particle size and, consequently, on the intensity of the luminescence.

At the light of the observed effects, in order to obtain highly efficient emitters, it is necessary to work at high precursor flow rates and low oxygen flow rate. However, these conditions would lead to big particle size. Therefore, the best synthetic settings lie in a compromise between these conditions. In our case, the best synthetic settings are 2mL/min for the precursor flow rate, 2 L/min for the oxygen flow rate and 2 bar for the pressure drop.

When working with luminescent materials, phase purity is a crucial requirement for the symmetry of the optic center and, as a consequence, for the transition probability and the intensity of the luminescence. Therefore, as described in 5.2.4, a solvent with higher combustion enthalpy (e.g. mixtures of xylene and 2EHA) would be more appropriate to produce nanoparticles with high monoclinic component.

In general, flame spray pyrolysis demonstrated to be an interesting technique for the production of nanostructured oxides, because, compared to the long batch traditional synthetic techniques, it is carried out in a very short time and can be run with inexpensive and easily available precursors [73]. The main advantages of this technique are its high rate of productivity, the easiness of the scale-up, and the preparation of products, at low cost, in continuous, and without the need of post-thermal treatments [132]. These are important requirements for the manufacturing of luminescent nanoparticles used for commercial purposes, particularly when high productivity is an imperative. However, FSP is limited to the design of the apparatus and to the chemistry of the combustion reaction that occurs in the flame.

The design of the apparatus influences the critical synthetic parameters below or over which it is not possible to set the synthesis [126]. The combustion reaction limits the choice of products to all those materials that can be produced with this kind of synthesis and the availability of their precursors [109]. As a consequence, it is really challenging prepare non-oxide compounds with this technique and this thesis is mainly focused on the preparation of oxide materials, with strong luminescence intensity.

6.3 Enhancement of the luminescence

The emission intensity of $\text{Gd}_2\text{O}_3:\text{Er}^{3+}$ nanocrystals increased with the incorporation of Yb^{3+} in concentration 1% Er^{3+} and 1% Yb^{3+} . The addition of Yb^{3+} enhances the energy transfer and, as a consequence, increases the efficiency of the upconversion process.

Alkali metals, especially Li^+ , increase further the emission intensity of the prepared $\text{Gd}_2\text{O}_3:\text{Er}^{3+}, \text{Yb}^{3+}$ nanocrystals. The overall increase of the luminescence and of the decay times suggests that their action is mainly due to the distortions that they create around the Er^{3+} site environment.

For the first time in the literature, GdVO_3 has been prepared by FSP in one step, without the need of any further thermal treatment. The crystals, doped with Er^{3+} , show very bright green luminescence intensity.

6.4 Core-shell systems

Silica-coated luminescent Gd_2O_3 have been prepared by FSP and compared with a traditional wet coating method. The flame spray technique resulted more convenient for the short time employed for the core-shell preparation, although the core nanocrystals resulted very aggregated. It has not been possible to prepare a core-shell system by FSP in one step.

7. *Future work*

7.1 Alkali metals

In order to better understand the effect of alkali metals on the luminescence intensity of nanostructured Gd_2O_3 , it is necessary to carry more specific structured analysis, such as X-Ray crystallography. Moreover, the preparation of single crystals would greatly contribute to the understanding of the distortions created by the presence of alkali metals around the Er^{3+} sites.

These studies should be accompanied by probe-spectroscopy investigation, with Eu^{3+} doped nanocrystals, in order to clarify the effect of the alkali metals on the optical active site.

7.2 Gadolinium vanadate nanocrystals

More dopant combinations should be studied for GdVO_4 nanocrystals prepared by FSP. Considering the bright luminescence of these nanocrystals, the development of luminescent materials in defined single colors would be extremely useful for the application in the display industry. Moreover, after studying the correct combination of dopants, the preparation of white emitting phosphors would be of interest for the production of LEDs.

7.3 Core-shell systems

The studies on core-shell systems should be further developed. Firstly, it is necessary a systematic study to investigate the relation between the thickness of the silica shell and the synthesis parameters (e.g. enthalpy of combustion, concentration of the precursor solution).

Magnetic/luminescent multifunctional systems should be investigated, considering the promising preliminary studies with $\text{Fe}_2\text{O}_3:\text{Gd}_2\text{O}_3:\text{Er}^{3+}, \text{Yb}^{3+}$, non reported in this work. Optical spectroscopy characterization (photoluminescence, decay times) and XRD analysis should be followed by magnetic characterization, via magnetoresistance.

However, in order to be considered as alternative method to other more conventional wet procedures, it is necessary to develop a FSP synthesis for the preparation of quasi-single particle core-shell systems in one step. This objective necessarily requires the revision of the FSP burner design: two burners should be employed for the simultaneous preparation of the core and shell via FSP.

8. *Bibliography*

- 1 <http://www.cedmagic.com/history/rca-first-postwar-630ts.html>, 10 March 2012.
- 2 T. Livius, *Ab Urbe Condita*
- 3 M. Taddia, *Chim. Ind. (Milan, Italy)* **85** (7), 37-38 (2003).
- 4 Becquerel, *Ann Chim. Phys.* (55), 3 (1859).
- 5 <http://www.ubergizmo.com/2009/06/super-small-vga-resolution-display/>, 10 March 2012.
- 6 T. Phillips, *Knockoff: The Deadly Trade in Counterfeit Goods*. (Kogan Page, London, 2005).
- 7 http://www.frenchfriends.info/gallery/money/euro_dots_2.jpg.html, 10 March 2012.
- 8 P. Pitts, 2005.
- 9 <http://cdn.ecologiae.com/wp-content/uploads/2009/05/pannelli-solari.jpg>, 10 March 2012.
- 10 T. Trupke, A. Shalav, B. S. Richards, P. Würfel, and M. A. Green, *Solar Energy Materials and Solar Cells* **90** (18-19), 3327-3338 (2006).
- 11 N. M. Brooks, *Foundations of Chemistry* **4**, 127 (2002).
- 12 Laing, *Foundations of Chemistry* **7**, 203 (2005).
- 13 I. McGill, *Rare Earth Elements*. (Wiley-VCH Verlag GmbH & Co. KGaA, 2000).
- 14 J. B. Hedrick, *Journal of Alloys and Compounds* **225** (1-2), 609-618 (1995).
- 15 K. Hans Wedepohl, *Geochimica et Cosmochimica Acta* **59** (7), 1217-1232 (1995).
- 16 J. A. Marinsky, L. E. Glendenin, and C. D. Coryell, *Journal of the American Chemical Society* **69** (11), 2781-2785 (1947).
- 17 N. G. Connelly, *Nomenclature of Organic Chemistry IUPAC Recommendations*. (Royal Society of Chemistry, 2005).
- 18 S. D. Barrett and S. S. Dhesi, *The structure of rare-earth metal surfaces*. (Imperial College Press, 2001).
- 19 S. Cotton, *Lanthanide and actinide chemistry*. (Wiley, 2006).
- 20 S. Hübner, *Optical Spectra of Transparent Rare Earth Compounds*. (Academic Press, New York, NY, 1978).
- 21 J. García Solé, L. E. Bausá, and D. Jaque, *An Introduction to the Optical Spectroscopy of Inorganic Solids*. (Wiley).
- 22 D. Dosev, I. M. Kennedy, M. Godlewski, I. Gryczynski, K. Tomsia, and E. M. Goldys, *Appl. Phys. Lett.* **88** (1), 011906/1-011906/3 (2006).
- 23 G. H. Dieke, H. M. Crosswhite, and H. Crosswhite, *Spectra and energy levels of rare earth ions in crystals*. (Interscience Publishers, New York, 1968).
- 24 F. Vetrone, *Luminescence spectroscopy of erbium⁽³⁺⁾ doped inorganic nanocrystals: An investigation into their upconversion properties* (2005) Concordia University, Montreal..
- 25 B. Henderson and G. F. Imbusch, *Optical spectroscopy of inorganic solids*. (Oxford University Press, 2006).
- 26 K. A. Gschneidner, J. C. G. Bünzli, and V. K. Pecharsky, *Handbook on the Physics and Chemistry of Rare Earths: Optical Spectroscopy*. (Elsevier, 2007).
- 27 F. Vetrone, J.-C. Boyer, J. A. Capobianco, A. Speghini, and M. Bettinelli, *Chem. Mater.* **15** (14), 2737-2743 (2003).
- 28 J. A. Capobianco, F. Vetrone, J. C. Boyer, A. Speghini, and M. Bettinelli, *J. Phys. Chem. B* **106** (6), 1181-1187 (2002).
- 29 J. Wang and P. A. Tanner, *Journal of the American Chemical Society* **132** (3), 947-949 (2009).
- 30 I. Etchart, M. Berard, M. Laroche, A. Huignard, I. Hernandez, W. P. Gillin, R. J. Curry, and A. K. Cheetham, *Chemical Communications* **47** (22), 6263-6265.

-
- 31 E. F. Schubert, *Light-emitting diodes*. (Cambridge University Press, 2006).
- 32 H. Guo, N. Dong, M. Yin, W. Zhang, L. Lou, and S. Xia, *J. Phys. Chem. B* **108** (50), 19205-19209 (2004).
- 33 F. Vetrone, J. C. Boyer, J. A. Capobianco, A. Speghini, and M. Bettinelli, *J. Phys. Chem. B* **107** (5), 1107-1112 (2003).
- 34 F. Vetrone, J.-C. Boyer, J. A. Capobianco, A. Speghini, and M. Bettinelli, *J. Appl. Phys.* **96** (1), 661-667 (2004).
- 35 S. Georgescu, V. Lupei, A. Petraru, C. Hapenciuc, C. Florea, C. Naud, and C. Porte, *J. Lumin.* **93** (4), 281-292 (2001).
- 36 A. Patra, C. S. Friend, R. Kapoor, and P. N. Prasad, *J. Phys. Chem. B* **106** (8), 1909-1912 (2002).
- 37 A. Patra, C. S. Friend, R. Kapoor, and P. N. Prasad, *Chem. Mater.* **15** (9), 3650-3655 (2003).
- 38 R. Scheps, *Opt. Mater.* **7** (3), 75-88 (1997).
- 39 H. Scheife, G. Huber, E. Heumann, S. Bär, and E. Osiac, *Optical Materials* **26** (4), 365-374 (2004).
- 40 S. A. Pollack, *The Journal of Chemical Physics* **40** (10), 2751-2767 (1964).
- 41 J. S. Bae, J. H. Jeong, and S. S. Yi, *Applied Physics Letters* **48** (1), 109-114 (2004).
- 42 S. Chen, X. Chen, M. Ding, and X. Niu, *Mat. Lett.* **35** (2), 178-181 (2007).
- 43 L. G. Jacobsohn, B. L. Bennett, S. C. Sitarz, O. Ugurlu, A. L. L. Sharma, D. W. Cooke, and R. E. Muenchhausen, *Materials Research Society Symposium Proceedings* **1056E** (Nanophase and Nanocomposite Materials V), 1056-HH08-06 (2008).
- 44 J.-C. Boyer, J. Gagnon, L. A. Cuccia, and J. A. Capobianco, *Chemistry of Materials* **19** (14), 3358-3360 (2007).
- 45 S. Heer, K. Kömpe, H. U. Güdel, and M. Haase, *Advanced Materials* **16** (23-24), 2102-2105 (2004).
- 46 R. Naccache, F. Vetrone, V. Mahalingam, L. A. Cuccia, and J. A. Capobianco, *Chemistry of Materials* **21** (4), 717-723 (2009).
- 47 Y. Sun, H. Liu, X. Wang, X. Kong, and H. Zhang, *Chemistry of Materials* **18** (11), 2726-2732 (2006).
- 48 R. Strobel, H. J. Metz, and S. E. Pratsinis, *Chem. Mater.* **20** (20), 6346-6351 (2008).
- 49 A. Vecht, C. Gibbons, D. Davies, X. Jing, P. Marsh, T. Ireland, J. Silver, A. Newport, and D. Barber, *J. Vac. Sci. Technol.* **17** (2), 750-757 (1999).
- 50 K. A. Franz, W. G. Kehr, A. Siggel, J. Wiczorek, and W. Adam, "Luminescent Materials", in *Ullmann's Encyclopedia of Industrial Chemistry* (Wiley-VCH Verlag GmbH & Co. KGaA, 2000).
- 51 H. S. Nalwa and L. S. Rohwer, *Handbook of Luminescence, Display Materials, and Devices*. (American Scientific Publishers, 2003).
- 52 S. S. Pitale, V. Kumar, I. M. Nagpure, O. M. Ntwaeaborwa, E. Coetsee, and H. C. Swart, *Journal of Applied Physics* **109** (1), 013105.
- 53 W. B. Im, Y.-I. Kim, and D. Y. Jeon, *Chemistry of Materials* **18** (5), 1190-1195 (2006).
- 54 Y. C. Kang, I. W. Lenggoro, S. B. Park, and K. Okuyama, *Mater. Res. Bull.* **35** (5), 789-798 (2000).
- 55 L. Xu, Y. Yu, X. Li, G. Somesfalean, Y. Zhang, H. Gao, and Z. Zhang, *Opt. Mater.* **30** (8), 1284-1288 (2008).
- 56 A. Camenzind, R. Strobel, and S. E. Pratsinis, *Chemical Physics Letters* **415** (4-6), 193-197 (2005).
-

- 57 M. D. Marcantonatos, *Journal of the Chemical Society, Faraday Transactions 2: Molecular and Chemical Physics* **82** (3), 381-393 (1986).
- 58 L. A. Riseberg and H. W. Moos, *Physical Review* **174** (2), 429 (1968).
- 59 W. O. Gordon, J. A. Carter, and B. M. Tissue, *J. Lumin.* **108** (1-4), 339-342 (2004).
- 60 B. M. Tissue, *Chem. Mater.* **10** (10), 2837-2845 (1998).
- 61 E. F. Gudgin Dickson, A. Pollak, and E. P. Diamandis, *Journal of Photochemistry and Photobiology B: Biology* **27** (1), 3-19 (1995).
- 62 D. Dosev, B. Guo, and I. M. Kennedy, *J. Aerosol Sci.* **37** (3), 402-412 (2006).
- 63 F. Wang and X. Liu, *Chem. Soc. Rev.* **38** (4), 976-989 (2009).
- 64 S. Heer, O. Lehmann, M. Haase, and H.-U. Güdel, *Angewandte Chemie International Edition* **42** (27), 3179-3182 (2003).
- 65 D. S. Zhao, Seokjun; Zhang, Haibo; Bae, Byeong-soo; Qin, Weiping, *Journal of Nanoscience and Nanotechnology* **10**, 2036-2039 (2010).
- 66 H. Wu, H. Xu, Q. Su, T. Chen, and M. Wu, *Journal of Materials Chemistry* **13** (5), 1223-1228 (2003).
- 67 J. A. Capobianco, F. Vetrone, T. D'Alesio, G. Tessari, A. Speghini, and M. Bettinelli, *Phys. Chem. Chem. Phys.* **2** (14), 3203-3207 (2000).
- 68 K. C. Patil, S. T. Aruna, and T. Mimani, *Curr. Opin. Solid State Mater. Sci.* **6** (6), 507-512 (2003).
- 69 B. Guo, A. Harvey, S. H. Risbud, and I. M. Kennedy, *Philos. Mag. Lett.* **86** (7), 457-467 (2006).
- 70 S. Shigeyuki and R. Roy, *Bull. Mater. Sci.* **23** (6), 453-460 (2000).
- 71 L. Mädler, H. K. Kammler, R. Mueller, and S. E. Pratsinis, *J. Aerosol Sci.* **33** (2), 369-389 (2002).
- 72 S. S. Balabanov, E. M. Gavrishchuk, A. M. Kut'in, and D. A. Permin, *Inorganic Materials* **47** (5), 484-488 (2011).
- 73 H. K. Kammler, L. Madler, and S. E. Pratsinis, *Chem. Eng. Technol.* **24** (6), 583-596 (2001).
- 74 G. L. Chiarello, I. Rossetti, P. Lopinto, G. Migliavacca, and L. Forni, *Catal. Today* **117** (4), 549-553 (2006).
- 75 G. L. Chiarello, I. Rossetti, L. Forni, P. Lopinto, and G. Migliavacca, *Appl. Catal. B-Environ.* **72** (3-4), 218-226 (2007).
- 76 H. K. Kammler, G. Beaucage, R. Mueller, and S. E. Pratsinis, *Chem. Ing. Tech.* **75** (8), 1138-1139 (2003).
- 77 P. N. Kapoor, A. K. Bhagi, R. S. Mulukutla, and K. J. Klabunde, *Mixed Metal Oxide Nanoparticles*. (Marcel Dekker, Inc, New York, 2004).
- 78 O. I. Arabi-Katbi, S. E. Pratsinis, P. W. Morrison, and C. M. Megaridis, *Combustion and Flame* **124** (4), 560-572 (2001).
- 79 A. Camenzind, R. Strobel, F. Krumeich, and S. E. Pratsinis, *Adv. Powder Technol.* **18** (1), 5-22 (2007).
- 80 Y. Shimomura and N. Kijima, *Electrochem. Solid-State Lett.* **7** (2), H1-H4 (2003).
- 81 S. Gao, H. Lu, Y. Nie, H. Chen, D. Xu, Q. Dai, J. Zhang, C. Gao, S. Kan, D. Li, and G. Zou, *Mat. Lett.* **61** (18), 4003-4005 (2007).
- 82 R. M. Laine, J. Marchal, H. Sun, and X. Q. Pan, *Adv. Mater. (Weinheim, Ger.)* **17** (7), 830-833 (2005).
- 83 J. Marchal, T. John, R. Baranwal, T. Hinklin, and R. M. Laine, *Chem. Mater.* **16** (5), 822-831 (2004).
- 84 Y. C. Kang, J. R. Sohn, H. S. Yoon, K. Y. Jung, and H. D. Park, *J. Electrochem. Soc.* **150** (2), H38-H42 (2003).

-
- 85 I. W. Lenggoro, B. Xia, H. Mizushima, K. Okuyama, and N. Kijima, *Mater. Lett.* **50** (2-3), 92-96 (2001).
- 86 F. Vetrone, J.-C. Boyer, J. A. Capobianco, A. Speghini, and M. Bettinelli, *J. Phys. Chem. B* **107** (39), 10747-10752 (2003).
- 87 N. Yamada, S. Shionoya, and T. Kushida, *J. Phys. Soc. Jap.* **32** (6), 1577-86 (1972).
- 88 J. S. Bae, J. H. Jeong, K. S. Shim, B. K. Moon, S.-s. Yi, J. H. Kim, Y. S. Kim, and J. S. Lee, *Applied Surface Science* **252** (13), 4564-4568 (2006).
- 89 J. S. Bae, K. S. Shim, B. K. Moon, S. B. Kim, J. H. Jeong, S. S. Yi, and J. H. Kim, *Journal of the Korean Physical Society* **46** (5), 1193-1197 (2005).
- 90 G. Y. Chen, H. C. Liu, H. J. Liang, G. Somesfalean, and Z. G. Zhang, *Solid State Commun.* **148** (3-4), 96-100 (2008).
- 91 J. H. Jeong, K. S. Shim, H. K. Yang, J. S. Bae, B. K. Moon, S. S. Yi, J. H. Kim, and Y. S. Kim, *J. Lumin.* **122-123**, 87-90 (2007).
- 92 J. Nayak, S. Kimura, and S. Nozaki, *J. Lumin.* **129** (1), 12-16 (2008).
- 93 J.-C. Park, H.-K. Moon, D.-K. Kim, S.-H. Byeon, B.-C. Kim, and K.-S. Suh, *Appl. Phys. Lett.* **77** (14), 2162-2164 (2000).
- 94 C.-S. Su and S.-M. Yeh, *Radiat. Prot. Dosim.* **65** (1-4, Solid State Dosimetry, Pt. 1), 89-92 (1996).
- 95 X. Yu, H.-g. Xu, J. Yin, and W.-f. Zhang, *Faguang Xuebao* **28** (5), 754-759 (2007).
- 96 S. H. Shin, J. H. Kang, D. Y. Jeon, and D. S. Zang, *Journal of Luminescence* **114** (3-4), 275-280 (2005).
- 97 J. S. Bae, J. P. Kim, J. H. Yoon, S. Park, M. S. Won, K. S. Shim, J. H. Jeong, and C. H. Kim, *Journal of the Korean Physical Society* **49** (4), 1615-1619 (2006).
- 98 E. J. Cussen, *Chem. Commun. (Cambridge, U. K.)* (4), 412-413 (2006).
- 99 M. P. O'Callaghan and E. J. Cussen, *Chem. Commun. (Cambridge, U. K.)* (20), 2048-2050 (2007).
- 100 H. Okamoto, K. Ino, H. Matsui, and G.-y. Adachi, *Hyogo-kenritsu Kogyo Gijutsu Senta Kenkyu Hokokusho* **7**, 1-7 (1997).
- 101 Z. Yang and Z. Jiang, *Chin. Sci. Bull.* **49** (24), 2572-2574 (2004).
- 102 Y. D. Park, J. S. Bae, J. K. Jang, Y. H. Kim, K. S. Shim, J. H. Jeong, and S. S. Yi, *Sae Mulli* **45** (6), 370-375 (2002).
- 103 N. S. Singh, R. S. Ningthoujam, L. R. Devi, N. Yaiphaba, V. Sudarsan, S. D. Singh, R. K. Vatsa, and R. Tewari, *J. Appl. Phys.* **104** (10), 104307/1-104307/9 (2008).
- 104 Y. Bai, K. Yang, Y. Wang, X. Zhang, and Y. Song, *Optics Communications* **281** (10), 2930-2932 (2008).
- 105 Q. Lu, F. Guo, L. Sun, A. Li, and L. Zhao, *J. Appl. Phys.* **103** (12), 123533/1-123533/10 (2008).
- 106 B. Guo, H. Yim, A. Khasanov, and J. Stevens, *Aerosol Science and Technology* **44** (4), 281-291 (2010).
- 107 H. Schulz, W. J. Stark, M. Maciejewski, S. E. Pratsinis, and A. Baiker, *Journal of Materials Chemistry* **13** (12), 2979-2984 (2003).
- 108 W. S. a. A. Fink, *J. Colloid. and Inter. Sci.* **26**, 62 (1968).
- 109 R. Strobel and S. E. Pratsinis, *J. Mater. Chem.* **17** (45), 4743-4756 (2007).
- 110 M. Arruebo, Fernández-Pacheco, M. R. Ibarra, and J. Santamara, *Nanotoday* **2** (3), 22-32 (2007).
- 111 D. Dosev, M. Nichkova, R. K. Dumas, S. J. Gee, B. D. Hammock, K. Liu, and I. M. Kennedy, *Nanotechnology* **18** (5), 055102/1-055102/6 (2007).
-

-
- 112 G. L. Chiarello, I. Rossetti, L. Forni, P. Lopinto, and G. Migliavacca, *Appl. Catal.*, B **72** (3-4), 227-232 (2007).
- 113 R. Jossen, S. E. Pratsinis, W. J. Stark, and L. Maedler, *J. Am. Ceram. Soc.* **88** (6), 1388-1393 (2005).
- 114 R. Jossen, W. J. Stark, L. Maedler, and S. E. Pratsinis, *Chem. Ing. Tech.* **75** (8), 1129-1130 (2003).
- 115 F. Vetrone, J.-C. Boyer, and J. A. Capobianco, *Encycl. Nanosci. Nanotechnol.* **10**, 725-765 (2004).
- 116 G. Chen, H. Liu, and Z. Zhang, Application: CN Patent No. 2007-10144773 101177611 (20071207. 2008).
- 117 B. D. Bartolo, *Optical Interactions in Solids*, Boston College, USA (2010).
- 118 W. T. Carnall, "Energy level structure and transition probabilities of the trivalent lanthanides in LaF_3 ", (Argonne National Laboratory, 1977).
- 119 J. G. Knudsen and D. L. V. Katz, *Fluid dynamics and heat transfer*. (McGraw-Hill, 1958).
- 120 W. J. Beek, K. M. K. Mutzall, and J. W. Heuven, *Transport phenomena*. (Wiley, 1999).
- 121 T. Ye, Z. Guiwen, Z. Weiping, and X. Shangda, *Mater. Res. Bull.* **32** (5), 501-506 (1997).
- 122 S. Polizzi, G. Fagherazzi, M. Battagliarin, M. Bettinelli, and A. Speghini, *J. Mater. Res* **16** (1), 146-154 (2001).
- 123 L. Madler, H. K. Kammler, R. Mueller, and S. E. Pratsinis, *J. Aerosol Sci.* **33** (2), 369-389 (2001).
- 124 L. E. Shea, J. McKittrick, O. A. Lopez, and E. Sluzky, *Journal of the American Ceramic Society* **79** (12), 3257-3265 (1996).
- 125 X. Qin, Y. Ju, S. Bernhard, and N. Yao, *J. Mater. Res.* **20** (11), 2960-2968 (2005).
- 126 G. L. Chiarello, I. Rossetti, and L. Forni, *J. Catal.* **236** (2), 251-261 (2005).
- 127 G. Y. Chen, H. C. Liu, G. Somesfalean, Y. Q. Sheng, H. J. Liang, Z. G. Zhang, Q. Sun, and F. P. Wang, *Appl. Phys. Lett.* **92** (11), 113114/1-113114/3 (2008).
- 128 Y. C. Kang, H. S. Roh, S. B. Park, and H. D. Park, *J. Mater. Sci. Lett.* **21** (13), 1027-1029 (2002).
- 129 H. S. Roh, Y. C. Kang, and S. B. Park, *Hwahak Konghak* **38** (2), 255-258 (2000).
- 130 S. S. Yi, J. S. Bae, B. K. Moon, J. H. Jeong, and J. H. Kim, *Appl. Phys. Lett.* **86** (7), 071921/1-071921/3 (2005).
- 131 J. A. Capobianco, P. Kabro, F. S. Ermeneux, R. Moncorgé, M. Bettinelli, and E. Cavalli, *Chemical Physics* **214** (2-3), 329-340 (1997).
- 132 S. E. Pratsinis, *Multi-Phase Flow Transp. Phenom., Int. Symp.* , 59-63 (2001).
-